

**Heat Assisted Magnetic Recording Head-Disk Interface: Numerical Simulation
of Air Bearing and Lubricant Mechanics**

by

Joanna Bechtel Dahl

A dissertation submitted in partial satisfaction of the
requirements for the degree of
Doctor of Philosophy

in

Engineering - Mechanical Engineering

in the

Graduate Division

of the

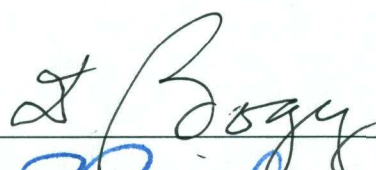
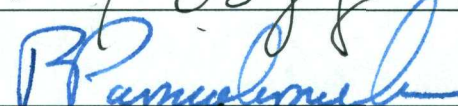

University of California, Berkeley

Committee in charge:

Professor David B. Bogy, Chair
Professor Panayiotis Papadopoulos
Professor Per-Olof Persson

Fall 2013

The dissertation of Joanna Bechtel Dahl, titled Heat Assisted Magnetic Recording Head-Disk Interface: Numerical Simulation of Air Bearing and Lubricant Mechanics, is approved:

Chair		Date	<u>9/16/2013</u>
		Date	<u>9/16/2013</u>
		Date	<u>9/19/2013</u>

University of California, Berkeley

**Heat Assisted Magnetic Recording Head-Disk Interface: Numerical Simulation
of Air Bearing and Lubricant Mechanics**

Copyright 2013
by
Joanna Bechtel Dahl

Abstract

Heat Assisted Magnetic Recording Head-Disk Interface: Numerical Simulation of Air Bearing and Lubricant Mechanics

by

Joanna Bechtel Dahl

Doctor of Philosophy in Engineering - Mechanical Engineering

University of California, Berkeley

Professor David B. Bogy, Chair

The hard drive industry widely views heat assisted magnetic recording (HAMR) as the technology to achieve 4 Tb/in² and greater storage densities and recapture the aggressive storage density growth rates of years past so that hard disk drives are able to meet the world's exploding data storage demand. While traditional magnetic media is thermally unstable at room temperature for the small bit sizes needed for high density recording, the high coercivity HAMR magnetic media can safely store digital data at very small bit sizes of (25 nm)². In order to write data, a near-field optical system confines electromagnetic energy below the diffraction limit to locally heat the HAMR recording bit to 400-500°C within a few nanoseconds. This adds new thermal complications to the already difficult mechanical and tribological design challenges for the head-disk interface (HDI) region. The reliability of hard drive read-write performance depends on the ability of the recording head slider, which contains the read and write elements, to stably fly in close proximity (< 5 nm) to the spinning recording disk. HAMR technology introduces heat-dissipating components and rapid thermal fluctuations to the HDI system not seen in traditional hard drives. Numerical simulations provide insightful information into the performance of HDI components that are difficult or impossible to attain experimentally.

This dissertation focuses on numerically simulating the mechanics of two components of the HDI under HAMR conditions: (1) the air bearing—pressurized airflow dragged in between the rapidly spinning disk and the slider—that supports the flying slider to maintain a < 5 nm minimum spacing above the disk and (2) the 1–2-nm-thick polymer lubricant that coats the disk to protect it against intermittent contact with the slider. Both are modeled using lubrication theory that is modified for gas rarefaction or thin-film polymer effects in order to provide useful system-level predictions.

In this work, the fully generalized molecular gas lubrication equation that allows for non-isothermal conditions is the basis for a simulation tool used to numerically study the effects of heat dissipation by inefficient near-field optics system components on the air bearing performance. The iterative HAMR static solver solves the coupled problem of air bearing

pressure generation and slider thermal deformation, linked by the heat transfer coefficient and pressure profile at the slider's air bearing surface (ABS). Static simulations are conducted for a simple HAMR slider in which the heat dissipating components are a thermal flying height control (TFC) heater, the near-field transducer (NFT), and laser diode. The NFT induces an additional 1–2 nm of localized protrusion compared to traditional TFC sliders, and it has the highest temperature of 175–300°C for the conditions tested. The waveguide dissipates heat away from the NFT and lowers the ABS maximum temperature, leading to a smoother NFT protrusion. Thermal creep, a rarefied gas flow driven by temperature gradients on the boundary, causes additional flying height drop of 0.05–0.15 nm for sliders with minimum flying heights below 2 nm. The efficiency of the read/write transducer and NFT are extremely sensitive to flying height, so even these differences of 0.1 nm will be significant in 4 Tb/in² HAMR systems in which the minimum flying height will only be 1 nm.

The lubricant covering the disk in a HAMR drive must be able to withstand the writing process. As a first step in modeling a robust lubricant, a simulation tool is developed that incorporates previously proposed film thickness variations of viscosity and an additional component of disjoining pressure due to functional end-groups. Here the simulation tool is applied to a conventional perfluoropolyether lubricant, Zdol 2000, for which there exists experimental data. Simulations at small length and time scales that are unobservable with current experimental capabilities are performed. For films thicker than 1 nm, the inclusion of polar disjoining pressure suppresses the lubricant thickness change due to evaporation and thermocapillary shear stress compared with cases without this component. Thin-film viscosity is an important property to consider for thinner lubricants. The smaller spot lubricant profiles have side ridges due to thermocapillary shear stress while the larger spot profiles show no side ridges, only a trough due to evaporation. The lubricant depletion zone width and depth increase with increasing thermal spot maximum temperature.

The lubricant must also sufficiently recover the lubricant depletion and accumulation zones so as to allow for stable flying heights and reliable read/write performance. Simulation results indicate that lubricant deformation caused by small thermal spots of 20-nm full-width half maximum (FWHM) recover on the order of 100–1000 times faster than larger 1- μ m FWHM spots. However, the lubricant is unable to recover from sufficiently high writing temperatures. An optimal thickness at which HAMR writing deformation recovers fastest is apparent for sub-100-nm FWHM thermal spots. Simulations show that simple scaling of experimental observations using optical laser spots of diameters close to 1 μ m to predict lubricant phenomena induced by thermal spots close to 20-nm FWHM may not be valid. Researchers should be aware of the possibility of different lubricant behavior at small scales when designing and developing the HAMR head-disk interface.

To my parents, Professor Stephen Bechtel and Barbara Bechtel, for their love, support and encouragement through the years.

Contents

Contents	ii
List of Figures	iv
List of Tables	ix
Acknowledgements	x
List of Symbols and Abbreviations	xi
1 Introduction	1
1.1 Hard Drive Industry Trends	1
1.2 Hard Disk Drive Technology and the Head-Disk Interface	2
1.3 Heat Assisted Magnetic Recording	4
1.4 Objective and Organization of this Dissertation	6
2 Lubrication Theory	8
2.1 Continuity for a General Fluid	8
2.2 Continuum Lubrication Equation for the Lubricant	12
2.3 Slip Correction from Kinetic Theory for the Air Bearing	15
3 Air Bearing Model and Numerical Solver	20
3.1 CMLAir-HAMR Air Bearing Solver	20
3.2 Iterative Static Solver	24
4 Static Slider Air Bearing Behavior in HAMR under Thermal Flying Height Control and Laser System Induced Protrusion	26
4.1 Introduction	26
4.2 Simplified HAMR Slider	28
4.3 HAMR Slider Component Effects on Flying Height	32
4.4 Effects of New Additions to the Air Bearing Simulation	41
4.5 Discussion	47
4.6 Conclusion	49

5	Lubricant Model and Its Numerical Solution	50
5.1	Lubricant Property Models	50
5.2	Non-dimensional Governing Equations for HAMR Writing and Recovery Conditions	56
5.3	Numerical Simulation Tool	59
6	Simulation of Lubricant Deformation During HAMR Writing	61
6.1	Introduction	61
6.2	Simulations Under HAMR Write Conditions	63
6.3	Discussion	78
6.4	Conclusion	83
7	Simulation of Lubricant Recovery After HAMR Writing	84
7.1	Introduction	84
7.2	Simulations of Recovery After HAMR Writing	85
7.3	Discussion	94
7.4	Conclusion	96
8	Conclusion and Future Work	97
8.1	Conclusion	97
8.2	Future Work	99
	Bibliography	101

List of Figures

1.1	Modern hard disk drive with cover plate removed. This particular drive contains four disk platters and eight suspension-slider assemblies, one for each side of every disk.	3
1.2	Head-disk interface region	4
2.1	HAMR lubricant system schematic: The thin lubricant film of unknown thickness $h(x, y, t)$ is subject to a scanning laser spot of speed u_D . Lubricant flow is driven by the resulting external shear stresses $\tau_{x,ext}$ and $\tau_{y,ext}$ and pressure gradient ∇p_{ext} . Some lubricant is removed from the film via evaporation (\dot{m}).	9
2.2	HAMR air bearing system schematic: The self-acting air bearing is pressurized to an unknown pressure $p(x, y, t)$ that balances the suspension load, resulting in an unknown slider flying height $h(x, y, t)$. The rotating disk results in relative planar velocities u_D and v_D from the reference frame of the slider. The pitch angle α and roll angle β are much less than 1 radian, typically tens of microradians.	10
3.1	Working principle of a hard disk drive air bearing. Air bearing simulation programs such as CMLAir-HAMR predict the pressure profile under the slider and the resulting flying attitude that balances a given suspension load.	21
3.2	Flowchart of the CMLAir-HAMR Iterative Static Solver. The purple box shows the flow of the ANSYS coupled field analysis.	25
4.1	The simplified HAMR slider finite element model used in all simulations. The trailing edge (TE) body contains the embedded waveguide and near field transducer (NFT). The bottom of the NFT is on the air bearing surface (ABS). The heater is embedded into the TE body $7 \mu\text{m}$ from the ABS. The laser diode is attached to the back of the slider, opposite the ABS.	29
4.2	ABS rail design used in CMLAir-HAMR and location of centerline plots. The colors reflect different etch depths. The base etch depth (deepest recess) of the ABS design is $1.651 \mu\text{m}$. The center of the trailing edge is shown in detail. The trailing edge region contains the read and write transducers and the NFT. The yellow dashed line indicates the location of centerline profiles shown in upcoming sections.	30

4.3	The power budget assumed for this study. Power absorbed by a component is assumed to be dissipated as heat.	31
4.4	Slider Component Study: Minimum flying height for different slider types. If present, the NFT heat generation rate is 1 mW, and the laser diode dissipates 50 mW. WG indicates the presence of the waveguide.	33
4.5	Slider Component Study: Centerline profiles of ABS temperature and thermal protrusion near the trailing edge, quantities determined in the ANSYS finite element solver. If present, the NFT heat generation rate is 1 mW, and the laser diode dissipates 50 mW.	34
4.6	Slider Component Study: Centerline profiles for air bearing pressure and flying height near the trailing edge, quantities determined by the air bearing solver CMLAir-HAMR. If present, the NFT heat generation rate is 1 mW, and the laser diode dissipates 50 mW.	36
4.7	Slider Component Study: ABS heat transfer coefficient H_{film} centerline profile near the trailing edge. H_{film} is calculated from the air bearing and pressure profiles (Figure 4.10) and used as the heat transfer boundary condition at the ABS in the finite element solver. If present, the NFT heat generation rate is 1 mW, and the laser diode dissipates 50 mW.	37
4.8	NFT Heat Dissipation Study: Minimum flying height for cases of 1-mW and 2-mW heat dissipation rate in the NFT.	38
4.9	NFT Heat Dissipation Study: Centerline profiles of ABS temperature and thermal protrusion near the trailing edge, quantities determined in the ANSYS finite element solver. Solid lines correspond to the 1-mW NFT heat dissipation rate and the dashed lines correspond to 2-mW NFT heat dissipation rate.	39
4.10	NFT Heat Dissipation Study: Centerline profiles for air bearing pressure and flying height near the trailing edge, quantities determined by the air bearing solver CMLAir-HAMR. Solid lines correspond to the 1-mW NFT heat dissipation rate and the dashed lines correspond to 2-mW NFT heat dissipation rate.	40
4.11	NFT Heat Dissipation Study: ABS heat transfer coefficient H_{film} centerline profile near the trailing edge. H_{film} is calculated from the air bearing and pressure profiles (Figure 4.10) and used as the heat transfer boundary condition at the ABS in the finite element solver. Solid lines correspond to the 1-mW NFT heat dissipation rate and the dashed lines correspond to 2-mW NFT heat dissipation rate.	41
4.12	Governing Equation Study: Difference in minimum flying height for various heater power levels: general MGL case (CMLAir-HAMR) minus isothermal MGL case (CMLAir).	42
4.13	Thermal Creep Study: Minimum flying height difference case including thermal creep minus the case without thermal creep	43

4.14	Thermal Creep Study: Flying height profiles near the NFT for cases including thermal creep and excluding thermal creep in CMLAir-HAMR. Noticeable differences in flying height are apparent for cases for which the minimum flying height is 2 nm or less.	43
4.15	Thermal Creep Study: Mass flow rate vectors (kg/s) with ABS temperature profile contour lines and the location of the NFT marked. The NFT power dissipation is 1 mW, and the heater power is 24 mW. The length of the vectors indicate the magnitude of the mass flow rate vector.	45
4.16	Flying height along the centerline near the trailing edge for cases using heat transfer model 1 (unmodified mean free path λ [53]) or heat transfer model 2 (modified mean free path λ_m [55]) and cases including and not including the temperature dependence on air mean free path.	46
5.1	Disjoining pressure is the resultant force of intermolecular interactions in the solid-liquid-vapor system within a range of influence r on the interfacial surface element dA	52
5.2	Disjoining pressure model reproduced from [79] with permission from Elsevier. This model is derived from experimental free energy measurements (sessile drop method) of unannealed PFPE Zdol 2000 on magnetic disks with a 1.3-nm amorphous hydrogenated carbon overcoat.	53
5.3	Viscosity model for Zdol from [84] based on Eyring's rate theory [83]. The arrow points in direction of increasing temperature.	54
5.4	Schematics of the lubricant system under HAMR writing and recovery conditions.	57
6.1	Thermocapillary shear stress, with assistance from thermoviscosity, is a main contributor to lubricant flow under HAMR writing conditions. Evaporation is set to zero in these simulations. If the temperature dependence of viscosity is included (denoted (T) in the legend), a significant amount of lubricant is drawn from the thermal spot center to side ridges in the cooler, higher viscosity regions. The thickness dependence of viscosity (denoted (h) in the legend) mitigates the amount of lubricant pulled away from the thermal spot center for thinner lubricant systems.	64
6.2	Disjoining pressure study: Cross-track profiles at the center of the depletion trough for lubricant systems of different thicknesses. Thin lubricant systems show little deformation for cases that including disjoining pressure. For thicker films, the inclusion of polar disjoining pressure suppresses lubricant deformation compared with cases without this component. $t_f = 2$ ns, $u_D = 5$ m/s, $T_{max} = 350^\circ\text{C}$, FWHM = 20 nm.	66
6.3	Disjoining pressure study: Amount of mass evaporated after 2 ns of illumination by the laser with a scanning speed 5 m/s. The variation in disjoining pressure with lubricant thickness determines the evaporation rate.	67

6.4	Disjoining pressure study: Instantaneous evaporative mass flux at 2 ns for the cases considering total disjoining pressure $\Pi = \Pi^d + \Pi^p$. Thinner lubricants have orders of magnitude lower evaporation rates compared with thicker lubricants.	68
6.5	Disjoining pressure study: Instantaneous lubricant viscosity at 2 ns for the cases considering total disjoining pressure $\Pi = \Pi^d + \Pi^p$. Thinner lubricants have orders of magnitude higher viscosity compared with thicker lubricants.	69
6.6	Disjoining pressure study: Final Laplace pressure for the cases considering total disjoining pressure $\Pi = \Pi^d + \Pi^p$. Laplace pressure and hence interface curvature become more severe as the lubricant thickens.	69
6.7	Disjoining pressure study with no evaporation: Cross-track profiles at the center of the depletion trough for lubricant systems of different thicknesses with evaporation suppressed. Total disjoining pressure suppresses lubricant flow away from the thermal spot center for thicker lubricants but has little effect for thin lubricant system. $t_f = 2$ ns, $u_D = 5$ m/s, $T_{max} = 350^\circ\text{C}$, FWHM = 20 nm.	71
6.8	Thin-film viscosity study: Cross-track profiles of viscosity at the center of the depletion trough for lubricant systems of different thicknesses. Thin-film viscosity is important to consider for thinner lubricants, but it has a smaller effect on lubricant flow for thicker lubricants. $t_f = 2$ ns, $u_D = 5$ m/s, $T_{max} = 350^\circ\text{C}$, FWHM = 20 nm.	74
6.9	Thin-film viscosity study: Viscosity at final lubricant profiles with and without thickness dependence of viscosity. For thick films, neglecting thickness dependence results in similar viscosity values. For thin films, neglecting the thickness dependence of viscosity predicts a value several orders of magnitude lower than the thin-film viscosity model. $t_f = 2$ ns, $u_D = 5$ m/s, $T_{max} = 350^\circ\text{C}$, FWHM = 20 nm.	75
6.10	Thermal spot size study: Cross-track profiles at the center of the depletion trough for lubricant systems of different thicknesses and thermal spot sizes. The cross-track coordinate is normalized by the thermal spot FWHM. The small spot profiles have side ridges due to thermocapillary shear stress while the largest spot profiles show no side ridges, only a trough due to evaporation. $t_f = 2$ ns, $u_D = 5$ m/s, $T_{max} = 350^\circ\text{C}$	76
6.11	Maximum temperature study: Comparison of lubricant cross-track profiles for different thermal spot maximum temperatures. The lubricant depletion zone width and depth increase with increasing thermal spot maximum temperature. FWHM = 20 nm, $h_0 = 1.2$ nm, $u_D = 5$ m/s.	78
6.12	Maximum temperature study: Comparison of total mass evaporated in 2 ns of thermal spot illumination time for different thermal spot maximum temperatures. The mass of one molecule of Zdol 2000 (M_w/N_A) is indicated by the horizontal dashed line. If thermal decomposition is ignored, significant mass loss due to evaporation does not occur below $\sim 300^\circ\text{C}$. FWHM = 20 nm, $h_0 = 1.2$ nm, $u_D = 5$ m/s, $t_f = 2$ ns.	79

7.1	Cross-track profiles after specified amounts of recovery time for different initial thicknesses ($h_0 = 0.7, 1.2,$ and 1.4 nm) and thermal spot sizes used during HAMR writing (illumination time 2 ns, scanning speed 5 m/s, $T_{max} = 350^\circ\text{C}$). The cross-track coordinate is normalized by the thermal spot FWHM for direct comparison.	87
7.2	Trough recovery rate for various initial lubricant thicknesses and thermal spot sizes. A star indicates the time at which the lubricant recovers to within 0.01 nm of the original thickness. The algorithm tolerance is 10^{-9} . Laplace pressure, which has a minor effect on the lubricant profile, is ignored for 20-nm and 100-nm FWHM to expedite the computation time.	88
7.3	Cross-track lubricant profiles for 20-nm FWHM and 1.2-nm initial thickness with and without Laplace pressure.	90
7.4	Lubricant trough recovery rates for $1\text{-}\mu\text{m}$ FWHM and 1.4-nm initial thickness with and without Laplace pressure.	90
7.5	Normalized volume to recover following HAMR writing and recovery time to within 0.01 nm of the initial thickness for different thicknesses and thermal spot sizes. The volume to recover is from a cross-sectional slice $3\cdot\text{FWHM}$ in width.	92
7.6	Cross-track lubricant profiles for different maximum temperature achieved during writing with a 20-nm FWHM. Initial (0 s of recovery, immediately after writing) and recovery after $1\ \mu\text{s}$ are shown for each T_{max} case. All effects, including Laplace pressure, are considered. $h_0 = 1.2$ nm, 20-nm FWHM case.	93

List of Tables

4.1	Simplified HAMR slider component material properties. The properties are k thermal conductivity, α_T thermal expansion coefficient, E Young's modulus, ν Poisson's ratio, and ρ electrical resistivity.	31
6.1	Comparison of characteristic forces driving lubricant flow for different lubricant thicknesses. $\Delta T = 325^\circ\text{C}$, thermal spot size FWHM 20 nm. Thermocapillary shear stress is the dominant flow force for thin lubricant thicknesses and the major flow force in thicker lubricant systems.	72
6.2	Normalized total evaporated mass \bar{m}_{evap} (kg/m^2) for four thermal spot sizes. The amount of normalized evaporated mass is comparable between the all thermal spot sizes.	77
7.1	Recovery time to within 0.01 nm of initial thickness for various thermal spot sizes (FWHM) and initial thicknesses. Laplace pressure is omitted for the 20-nm and 100-nm FWHM cases to speed up computation time.	86
7.2	Recovery time to within 0.01 nm of initial thickness for various thermal spot maximum temperatures achieved during HAMR writing. Laplace pressure is neglected to speed up the computation time.	93

Acknowledgments

First and foremost, I would like to thank my adviser, Prof. David Bogy, for guiding and supporting me through my doctoral work and believing in me even when I didn't believe in myself. I am grateful to him for providing valuable technical and professional advice while giving me the freedom to explore my own research interests. I am really fortunate to have him both as an advisor and a mentor.

I also would like to thank Profs. Panayiotis Papadopoulos and Per-Olof Persson for their feedback on this dissertation, discussions here and there that got me out of a research rut, and for serving on my qualifying exam committee. My education at UC Berkeley was also enhanced by taking one or more of their classes, some of the best courses I took as a graduate student.

“If I have seen farther, it is by standing on the shoulders of giants,” wrote Isaac Newton in a letter to his rival Robert Hooke in 1676. In my case, I stood on the shoulders of current and former graduate student researchers in Prof. Bogy's Computer Mechanics Laboratory. The work of labmates Liping Li, Shaomin Xiong, Yung-Kan Chen, Alejandro Rodriguez, Jinglin Zheng, Sripathi Canchi, Rahul Rai, Sean Mosley, Nan Liu, Liang Pan, Soroush Sarabi, Ning Li, Jia Zhao, and Yuliang Liu have all informed the work presented in this dissertation in some fashion. I want to give special thanks to Dolf Mardan for assisting me and the rest of the lab with the computer resources required for our work. Thanks also to Dr. Bair Budaev for discussing with me his ideas on near-field heat transfer phenomena and, along with Prof. Bogy, inspiring me to be a thorough, rigorous scientist whose work is based on fundamental principles.

In the summer of 2010, I was fortunate to work as a summer intern at Seagate's facility in Minneapolis thanks to the efforts of Cynthia Hipwell. Thank you to James Kiely and Bob Crone for being my primary mentors. I also appreciate the kindness shown to me by everyone in the air bearing group that included Eric Montei, Manuel Anaya-Dufresne, Zoron Jandric, and Anil Reddy.

Finally, my accomplishments have been possible because of the love, support, and encouragement from my wonderful family. Words cannot express how grateful I am for the loving home and firm foundation provided to me by my parents and sister. Thanks also to all the extended Bechtel and Smith family members involved in teaching, higher education, and science for their encouragement and inspiration by example. Last but not least, my husband Rob has been most supportive and caring, especially in the final year of my (research/dissertation-bingeing) doctoral studies.

The research presented in this dissertation was supported by the Computer Mechanics Laboratory, the Information Storage Industry Consortium's Extremely High Density Recording Program, and the International Disk Drive Equipment and Materials Association's Advanced Storage Technology Consortium.

List of Symbols and Abbreviations

List of Symbols

D	inverse Knudsen number, $\sqrt{\pi}/(2 \cdot \text{Kn})$
h	flying height or spacing, air bearing or lubricant film thickness [m]
h_m	characteristic spacing at the trailing edge center of the slider [m]
H	nondimensional flying height or air bearing thickness, h/h_m
Kn	Knudsen number, λ/h
L	slider length or thermal spot FWHM [m]
\dot{m}	evaporative mass flux, [kg/(m ² ·s)]
M_w	molecular weight [kg/mol]
N	number density [molecules/m ³]
p	local pressure [Pa]
p_0	ambient pressure [Pa], 1 atm = 101325 Pa
P	nondimensional local air bearing pressure, p/p_0
Q_P, Q_T	non-dimensionalized flow rate coefficient
Q_{con}	flow rate coefficient for Poiseuille flow in the continuum limit, $D/6$
$\overline{Q}_P, \overline{Q}_T$	relative non-dimensionalized flow rate coefficient, Q/Q_{con}
R	universal gas constant, 3.14462 J/(mol·K)
T	temperature, [K or °C]
T_0	characteristic temperature, [K or °C], 25°C
\overline{T}	non-dimensional air bearing local temperature, T/T_0
u_D	thermal spot scanning speed during HAMR writing [m/s]
U, V	air bearing disk boundary speeds in x, y directions [m/s]
u, v, w	x, y, z components of velocity
x, y, z	Cartesian coordinates with x being the slider length direction or down-track direction, y the slider width or cross-track direction, and z the film thickness direction
X, Y, Z	nondimensional coordinates, $x/L, y/L, z/h_m$
α	surface accommodation coefficient or evaporation coefficient
λ	mean free path [m]

λ_m	modified mean free path that accounts for close proximity of bounding surfaces [m]
Λ_x, Λ_y	bearing number, $U \frac{6\mu L}{p_a h_m^2}$, $V \frac{6\mu L}{p_a h_m^2}$
μ	air bearing viscosity [Pa·s]
$\bar{\mu}$	non-dimensional air bearing viscosity, μ/μ_0
η	lubricant viscosity [Pa·s]
ρ	density [kg/m ³]

Subscripts

0	ambient conditions
d	disk
P	Poiseuille flow
s	slider
T	thermal creep flow
w	air bearing boundary wall (slider or disk)

Superscripts

d	dispersive
p	polar

List of Abbreviations

ABS	air bearing surface
CML	Computer Mechanics Laboratory
FWHM	full-width at half-maximum
HAMR	heat assisted magnetic recording
HDD	hard disk drive
HDI	head-disk interface
MGL	molecular gas lubrication
PFPE	perfluoropolyether
TFC	thermal flying height control
NFT	near-field transducer

Chapter 1

Introduction

The digital and computer technology advances in the last several decades have been made possible in part by the ability to store and access digital data. Much of the world's digital information has been and still is stored on hard disk drives (HDDs). While hard drives may appear to the consumer to be giving way to solid state drives (SSDs) in many popular mobile devices, the convenience of accessing your data "anytime, anywhere" on multiple devices is possible because of the storage of multiple copies of your digital data on servers, refrigerator-sized arrays of hard disk drives connected on a network, maintained by a cloud service provider. Digital technology has also been leveraged in practically every sector of modern society; all these activities require storage and access of digital data, tasks often provided by hard disk drives. As the worldwide demand for data storage continues to explode at a 40% annual rate, HDDs remain an important infrastructure player in the world's technological development.

This introductory chapter provides an overview of hard drive industry trends that are pushing for higher storage capacities in products. Next the basics of hard disk drive technology and the topic of interest for this dissertation, the head-disk interface, are described. Heat assisted magnetic recording is introduced, a technology widely seen by the industry as necessary to achieve higher storage densities. Finally the motivation, objectives, and organization of this dissertation are given.

1.1 Hard Drive Industry Trends

In 1956 IBM introduced the first hard disk drive, the IBM RAMAC, which IBM leased to businesses at a cost of \$3,200 per month in 1957 dollars, equivalent to about \$26,600 today [1]; the IBM RAMAC had a storage capacity of 5 MB and weighed over one ton. Seagate currently makes a hybrid solid state-hard disk drive for laptops that has a storage capacity of 1 TB, weighs 0.254 pounds, and costs only \$130 [2]. The dramatic increase in areal storage density (often reported with units bits/in²) and decrease in cost per bit is due to many technological advances in the past five decades. Over 200 companies have participated

in the improvement of hard drive assembly since 1956, but by 2013 the industry has whittled down to three companies through mergers, acquisitions and failures—Seagate Technologies, Western Digital, and Toshiba [3], evidence that HDD technology issues are difficult and now more than ever require a large amount of investment to develop and produce the next generation of HDDs.

Certainly SDDs are superseding HDDs in familiar mobile devices, but the hard drive industry still provides cheap, reliable mass storage capabilities that are not going to be met by SDDs in the near future. The world's total SSD capacity is not enough to replace all the data currently stored on HDDs [4]. Nor can the SDD industry be expected to grow fast enough to meet digital storage demand, forecasted to grow by a factor of 300 from 2005 to 2020, that is from 130 exabytes (130 billion GBs) to 40,000 exabytes (40 trillion GBs) [5]. The world has large data storage demands to be met, and only HDDs have the manufacturing capacity to meet a majority of the demand. In addition, hard drive companies have recognized solid state and magnetic hard drives are synergistic technologies that can be combined to take advantage of each technology's strengths: in January 2013, Seagate entered into a strategic agreement with a flash-based storage-class memory company to jointly address the growing enterprise flash storage market [6], and in June 2013 HGST, a Western Digital Company, acquired an enterprise solid-state drive company [7].

A major emphasis in the HDD industry has always been to increase areal density, but in recent years the compound annual growth rate of storage density has slowed from 60–100% in the years 1990–2002 to less than 25% in the years since 2010 as the limits of current technology have been reached [8]. Meanwhile, demand for storage is growing roughly 40% every year [4], and it is forecasted to grow over 50% per year through 2020 [5]. To fill the gap between demand and supply by simply producing more HDDs—to be assembled into more servers that would be housed in more data centers—would require an enormous amount of capital investment by HDD companies, their suppliers, and their customers. Hard drive companies view introducing new technologies that recapture aggressive storage density growth rates as the most economical way to meet the world's data storage demand. Certainly the explosion of data storage demand is an opportunity for the hard drive industry, a big business with revenues expected to be over \$50 billion in 2013 [8], to grow and sell more products.

1.2 Hard Disk Drive Technology and the Head-Disk Interface

A hard disk drive is composed of the disk on which the data is stored along with the components that allow for the reading and writing of data (Figure 1.1). Binary digital information is stored on thin film ferromagnetic material on a disk as bits, uniformly magnetized regions composed of tens of grains with "up" or "down" magnetic orientation. The magnetic recording layer (30 nm thick) is deposited onto a substrate. This relatively soft layer is protected

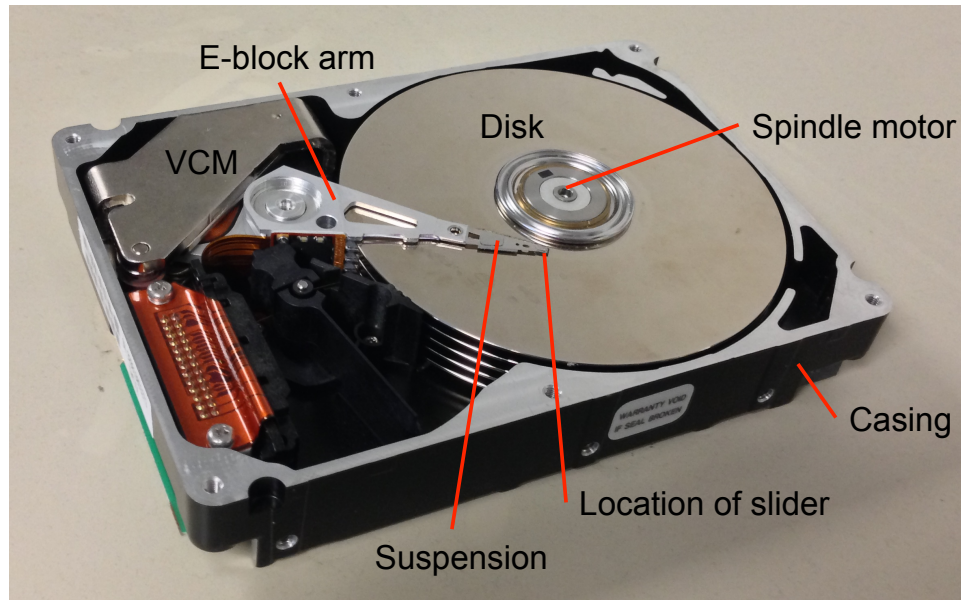


Figure 1.1: Modern hard disk drive with cover plate removed. This particular drive contains four disk platters and eight suspension-slider assemblies, one for each side of every disk.

from impact, corrosion, and wear by a hard diamond-like carbon overcoat (2–3 nm thick) and a thin polymer lubricant layer (1–2 nm thick). A spindle motor rotates the circular disks, and the magnetic information is written to or read from concentric tracks. As the disk spins at 5,400–10,000 RPM, magnetic field transitions are converted into electric current (read operation) or vice versa (write operation) by read and write transducers embedded in a small body called a slider or recording head. The read and write transducers are protected from contact and corrosion by a carbon overcoat (2–3 nm thick). The slider is attached to the end of a suspension arm that is in turn attached to an E-block arm. The E-block arm is actuated by a voice coil motor (VCM) to position the slider over the desired recording track. The relative velocity between the disk and slider, on the order of 10 m/s, forms a self-acting pressurized gas bearing called the air bearing that balances the applied suspension load and moments that act to push the slider toward the disk. In equilibrium, the slider is "flying" above the disk with physical clearance (also called flying height) of 5 nm or less in modern HDDs.

The surface of the slider facing the disk, called the air bearing surface (ABS), is etched with a special design that controls the air flow under the slider and determines the slider's flying attitude. A recent technology called thermal flying height control (TFC) improves the flying reliability at low physical clearances by only bringing the trailing edge portion of the slider containing the read and write transducers close to the disk [9]. Power is supplied to a resistive heater embedded in the slider, and the thermal expansion bulge containing the read/write transducer brings these elements to the required physical proximity to the disk.

The mechanical stability of the head-disk interface (HDI), the region between the slider and the disk, is important for the performance and reliability of HDDs. Components of the HDD that influence the HDI include the air bearing, slider, suspension, the multi-layered recording disk, and the lubricant (Figure 1.2). The Wallace Spacing Loss equation states that the intensity of the read-back signal when performing the read operation decreases exponentially with increasing distance between the magnetic media and the read/write transducers [10]. Therefore as the size of the bits are decreased to increase storage density, the physical spacing between the disk and slider must be as small as possible in order to realize a good signal to noise ratio. The reliability of HDD read-write performance depends on the ability of the slider to stably fly in close proximity to the disk with no more than 10% variation in the slider’s flying attitude—its flying height and pitch and roll angles—across all tracks. This is the mechanical and tribological challenge for HDI design.

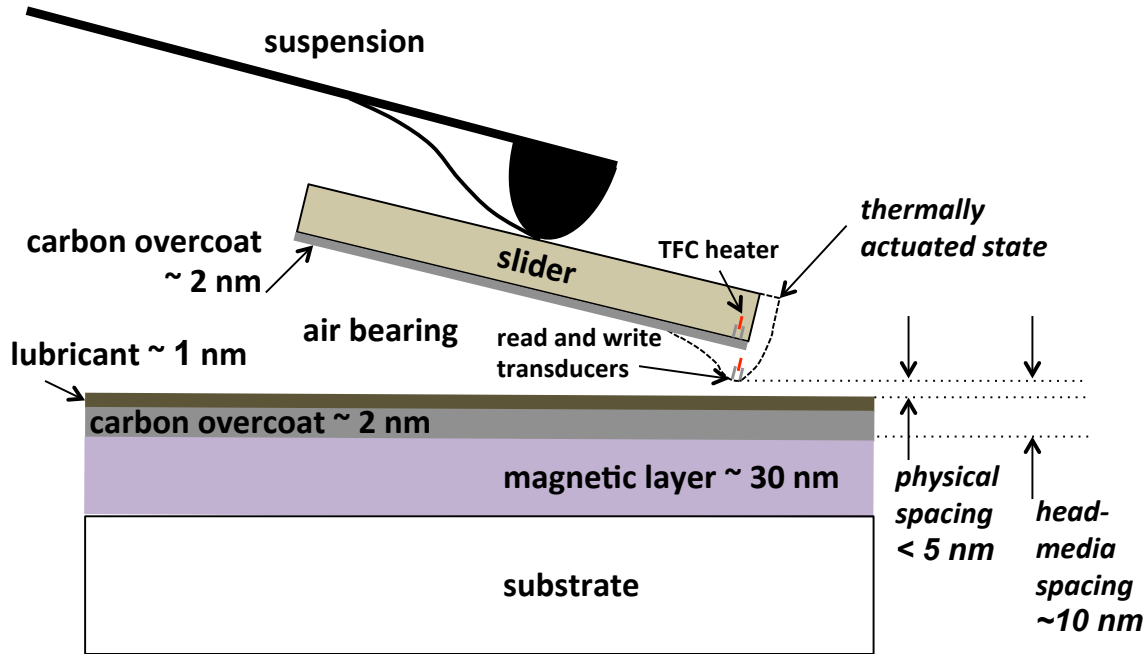


Figure 1.2: Head-disk interface region

1.3 Heat Assisted Magnetic Recording

Current HDD products are approaching 1 TB/in² storage density. Higher storage densities will soon no longer be possible because the superparamagnetic limit will be reached for current product magnetic media: if the size of the magnetic bits are further decreased, the bits will be thermally unstable [11]. At room temperature, the random thermal fluctuations of media molecules have the strength to overcome the energy barrier between "up" and

”down” magnetic orientations, thereby demagnetizing the bit grains and corrupting the stored magnetic data. The industry agrees that a new technology is needed to increase the storage density of HDDs above 1 TB/in² and recapture aggressive storage density annual growth rates of years past to meet the digital data storage demand. Over the past few years, the HDD industry has reached a consensus that Heat Assisted Magnetic Recording (HAMR) will be the first high density recording technology brought to market. Other technologies are also being investigated but not as aggressively as HAMR as of 2013: bit patterned media and microwave assisted recording.

The principle of HAMR is to use a new magnetic media that will be thermally stable at room temperature for the bit sizes needed to exceed 1 TB/in². This new media, likely FePt, has a higher coercivity than traditional HDD media so that the magnetically encoded data is frozen at room temperature. At room temperature, a very high magnetic field would need to be applied in order to write data on the high coercivity media, far beyond capabilities of current write transducers embedded in the slider. In HAMR, this problem is solved by locally heating the bit, thereby reducing the media’s coercivity and allowing manipulation of the grain’s magnetic orientation at a lower magnetic field strength than the write transducer is capable of producing. After writing is completed, the means of heating is turned off and the media cools back to ambient temperature where the magnetic orientation of the magnetic grains is stable and the data is safe from corruption.

One set of challenges to overcome before bringing HAMR products to market arises from the thermal issues introduced by the heating of the media during the writing process. On the disk, small thermal spot sizes that rapidly heat up and cool are needed to achieve 4–5 TB/in², the industry’s storage density goal for the next couple of years. Industry consensus indicates that a thermal spot with a full width at half maximum (FWHM) of 25 nm will be required [12]. The heating and cooling times are expected to be on the order of nanoseconds. The leading HAMR media candidate FePt has a Curie temperature (temperature at which the material’s coercivity is zero) of 700 K = 427°C, and it is expected that the maximum temperature on the disk during HAMR writing will need to be around 500°C to successfully orient the entire bit domain. This means that the thermal gradient on the disk will be on the order of 10¹⁰ °C /m. With these high temperature gradients and rapid heating and cooling rates, thermal fatigue becomes an issue. Because the carbon overcoat and lubricant for current HDDs are destroyed in the high temperatures realized in the HAMR HDI, the industry is investigating new revolutionary materials and processing methods for these protective layers.

Another major hurdle for HAMR is finding a method to concentrate energy so that a small thermal spot on the media only 25 nm FWHM can be achieved. This is well below the diffraction limit of visible and infrared laser beams focused by far-field optics in air. BluRay players are examples of high density optical data storage, and their focused spot size is close to 230 nm. To overcome the diffraction limit, near-field optics uses waveguides to transmit and confine electromagnetic waves from an optical laser diode to an antenna or aperture that can then transmit sufficient energy to the magnetic media. The antenna or aperture, called a near-field transducer (NFT), must be no more than a couple of nanometers from the

disk surface in order to achieve reasonable transmission efficiencies. An optimized near-field optical delivery system will likely be integrated into the slider body and only transmit $< 5\%$ of the electrical power supplied to the laser diode to the recording bit on the disk [13, 14]. The inefficiencies of the laser delivery system are likely dissipated as heat elsewhere in the system, most notably in the laser diode, NFT, and write pole [15, 16]. Throughout this text, the near-field optical delivery system will loosely be called the laser deliver system. More explanation of the laser delivery system will be given in Section 4.2 when we describe a simple HAMR slider of our own design.

In addition to developing the HAMR technology, the head-media spacing must also be reduced from 10 nm in current HDD products to ~ 4.5 nm for 4 TB/in² magnetic recording. In other words, between the bottom of the read/write transducer and the top of the magnetic media, the sum of the slider carbon overcoat, physical clearance, lubricant, and disk carbon overcoat thickness can only total 4.5 nm. The HDI researchers in the industry believe new revolutionary technologies in materials, processes, and clearance control schemes will be needed to realize the estimated 0.9 nm head overcoat, 1 nm flying height, 0.8 nm lubricant, and 1.5 nm disk overcoat requirements [12]. Not only will the capabilities of HDI technology be stretched to reduce head-media spacing to 4.5 nm, but new challenges and requirements to HDI stability will be introduced by HAMR never seen before in traditional drives.

1.4 Objective and Organization of this Dissertation

Analysis and modeling of HDI components in traditional (non-HAMR) hard drives usually assumes isothermal conditions for the air bearing and lubricant. The isothermal assumption is reasonable for traditional HDDs in which the slider's ABS is less than 100°C under thermal flying height control and the disk is not subjected to a heat source. However, in HAMR drives the disk will be rapidly heated several hundred degrees above ambient and experience a very high temperature gradient due to the focused energy on the recording bit; the slider's temperature will increase due to dissipated heat from the laser delivery system. Therefore, an assumption of isothermal conditions for the air bearing and lubricant is likely not valid for HAMR systems. Accurate HDI component models are essential as the targeted clearance between the head and slider is only 1 nm and the targeted lubricant thickness is 0.8 nm—even 0.1 nm difference in predicted flying height or lubricant thickness is a significant 10% or 12.5% of the component's thickness budget.

This work improves models for two HDI components, the air bearing and lubricant, by introducing the ability to model the non-isothermal conditions seen in HAMR HDD operation. This is accomplished by adding new thermal drivers of air flow (thermal creep) and lubricant flow (thermocapillary shear stress) and implementing material property models that include variation with local temperature (viscosity and mean free path for air; viscosity, surface tension, and vapor pressure for the lubricant) .

The objective of this dissertation is to advance the understanding of the head-disk interface behavior under HAMR conditions by

- developing models of two components of the HDI, the air bearing and the lubricant, for HAMR conditions,
- performing numerical simulations to predict air bearing and lubricant behavior under HAMR usage conditions that are difficult to observe experimentally, and
- identifying slider or lubricant design issues that may mitigate thermal effects on the air bearing and lubricant.

Lubrication theory is used to model both the air bearing and the lubricant, with modifications to account for rarefaction (air bearing) or thin film confinement effects (lubricant). These variations on the lubrication equation are the basis for the numerical simulations developed in this dissertation. Chapter 2 presents a derivation of the governing partial differential equation and then describes how the equation is modified to suit the air bearing and lubricant systems. Chapter 3 introduces the model and numerical solver for the air bearing and highlights new features added to account for thermal effects introduced by HAMR. Chapter 4 presents static simulation results of our simplified HAMR slider, and it shows the effects of laser delivery system components and new air bearing solver features on the slider's flying performance. The lubricant model and numerical solver is discussed in Chapter 5. Chapter 6 presents simulations of lubricant deformation during HAMR writing, and Chapter 7 presents simulations of lubricant recovery following HAMR writing. Finally, a concluding summary and suggestions for future work are provided in Chapter 8.

Chapter 2

Lubrication Theory

The minimum physical spacing between the disk and slider is less than 5 nm and the initially uniform lubricant thickness is close to 1 nm, which provide characteristic lengths that are much smaller than the lateral dimensions of the slider (usually 700-850 μm) and the disk radius (typically 10-30 mm). When modeling these components of the head-disk interface, one can take advantage of the characteristic length disparity between coordinate directions to simplify the analysis. For both the air bearing and the lubricant coating on the disk, the governing equations are specialized forms of the well-known Reynolds lubrication equation [17]. The lubricant is considered to be an incompressible Newtonian fluid, and its governing evolution equation is derived via the traditional lubrication approximation procedure first described by Reynolds. The air bearing is modeled as a dilute ideal gas, and sophisticated slip correction coefficients are derived from the linearized Boltzmann equation with the Bhatnagar-Gross-Krook (BGK) collision integral approximation [18]. This chapter presents an overview and justification of the models used for the lubricant and air bearings, and it highlights the assumptions used and the limitations of the lubrication and kinetic theories.

2.1 Continuity for a General Fluid

The classical Reynolds equation governs the pressure generation in a lubricating fluid film. By combining the statements of conservation of mass and conservation of momentum, the evolution of a lubrication system can be described by one equation if the system is isothermal. For non-isothermal systems in which the fluid temperature is unknown, the energy equation must also be solved simultaneously. However, in this work we simplify our analysis by assuming we know the temperature profile of the fluid so as to bypass solving the energy equation. The electro-thermo-mechanical problem of transferring energy from the laser delivery system embedded in the slider to the recording bit on the disk surface is quite complicated and not well understood. Therefore, because the energy transfer is difficult and not a focus of this work, we will assume an idealized temperature distribution for the lubricant and use a simple averaged temperature estimate for the air bearing.

The lubrication equation derivation starts from the continuity equation. We consider a general fluid here and specialize the results for the assumed incompressible lubricant and compressible air bearing in the upcoming sections. For a continuum fluid, the local form of mass conservation is

$$\frac{\partial \rho}{\partial t} + \frac{\partial(\rho u)}{\partial x} + \frac{\partial(\rho v)}{\partial y} + \frac{\partial(\rho w)}{\partial z} = 0, \quad (2.1)$$

where ρ is the fluid density, h is the fluid film thickness, and u, v and w are the fluid velocity components in the x, y and z directions. By integrating the continuity equation in the z direction from $z = 0$ (disk surface) to $z = h$ (lubricant-air interface or slider ABS), we simplify the analysis from determining the details of the velocity profiles in the z direction to just determining average flow rates. Next we introduce the lubricant and air bearing systems before proceeding with the lubrication equation derivation.

We model the lubricant as a viscous liquid bounded below by a horizontal solid substrate (the magnetic recording disk) and above by an interface between the liquid film and a passive gas (the air bearing) (Figure 2.1). The coordinate system is fixed to the disk, and the scanning thermal spot moves with speed u_D in the down-track (x) direction. Because the lubricant simulations are confined to one track, which is less than 100 nm wide, we ignore the effect of slider skew angle. The velocity boundary conditions for the lubricant originate from a no-slip assumption at the disk surface and interface kinematics and stress balance at the lubricant-air interface. The no-slip boundary condition is reasonable because the lubricant type studied in this work has hydroxyl end-groups that hydrogen bond to active sites on the disk surface [19]. PFPE lubricants exhibit viscoelastic behavior [20], but here we assume a purely viscous model for simplicity, so the shear stresses in the lubricant are proportional to the velocity gradients: $\tau_{x,ext} = \tau_x = \mu \frac{\partial u}{\partial z}$ and $\tau_{y,ext} = \tau_y = \mu \frac{\partial v}{\partial z}$. The lubricant pressure balances the applied pressure: $p = p_{ext}$. The external shear stresses $\tau_{x,ext}, \tau_{y,ext}$ and pressure p_{ext} acting on the lubricant will be discussed in Section 5.1. The lubricant boundary

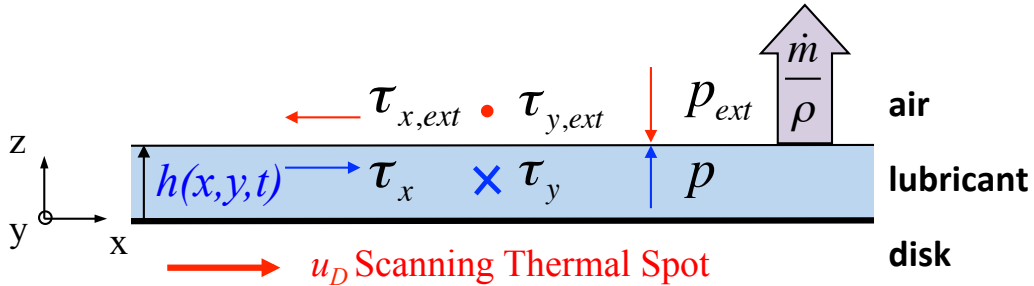


Figure 2.1: HAMR lubricant system schematic: The thin lubricant film of unknown thickness $h(x, y, t)$ is subject to a scanning laser spot of speed u_D . Lubricant flow is driven by the resulting external shear stresses $\tau_{x,ext}$ and $\tau_{y,ext}$ and pressure gradient ∇p_{ext} . Some lubricant is removed from the film via evaporation (\dot{m}).

conditions are as follows:

$$\text{at } z = 0 : u = u_D, \quad v = 0, \quad w = 0 \quad \text{no slip} \quad (2.2a)$$

$$\text{at } z = h(x, y, t) : \mu \frac{\partial u}{\partial z} = \tau_x, \quad \mu \frac{\partial v}{\partial z} = \tau_y, \quad \text{stress balance} \quad (2.2b)$$

$$w = \frac{dh}{dt} = \frac{\partial h}{\partial t} + u|_{z=h} \frac{\partial h}{\partial x} + v|_{z=h} \frac{\partial h}{\partial y} \quad \text{kinematic condition} \quad (2.2c)$$

The air bearing is modeled as a (compressible) ideal gas (Figure 2.2). Generally the slider has a non-zero skew angle with respect to the down-track direction, so for a coordinate system fixed in the reference frame of the slider, there are x and y components of the fluid velocity. Rarefaction effects (deviation from no-slip boundary condition) will be incorporated into expressions for mass flow rate. For the air bearing system, the velocity boundary conditions originate from a no-slip assumption and the kinematic condition for slider flying height. The air bearing velocity boundary conditions are:

$$\text{at } z = 0 : u = u_D, \quad v = v_D, \quad w = 0 \quad \text{no slip} \quad (2.3a)$$

$$\text{at } z = h(x, y, t) : u = v = 0, \quad w = \frac{dh}{dt} = \frac{\partial h}{\partial t} \quad \text{no slip and kinematic condition} \quad (2.3b)$$

Because the air bearing is compressible, pressure $p(x, y, t)$ is also an unknown in addition to the flying height $h(x, y, t)$. The pressure boundary condition is ambient pressure at the edges of the slider body domain.

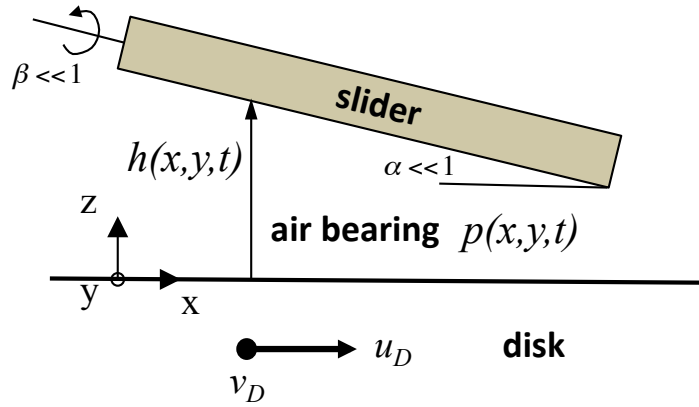


Figure 2.2: HAMR air bearing system schematic: The self-acting air bearing is pressurized to an unknown pressure $p(x, y, t)$ that balances the suspension load, resulting in an unknown slider flying height $h(x, y, t)$. The rotating disk results in relative planar velocities u_D and v_D from the reference frame of the slider. The pitch angle α and roll angle β are much less than 1 radian, typically tens of microradians.

The most general boundary conditions between the lubricant system (Equation 2.2) and air bearing system (Equation 2.3) will be used in this section for the derivation and are as follows:

$$\text{at } z = 0 : u = u_D, \quad v = v_D, \quad w = 0 \quad (2.4a)$$

$$\begin{aligned} \text{at } z = h(x, y, t) : u &= u|_{z=h}, \quad v = v|_{z=h}, \\ w &= \frac{dh}{dt} = \frac{\partial h}{\partial t} + u|_{z=h} \frac{\partial h}{\partial x} + v|_{z=h} \frac{\partial h}{\partial y} \end{aligned} \quad (2.4b)$$

Integrating the continuity equation across the film thickness, we obtain the apparent result:

$$\int_0^h \frac{\partial \rho}{\partial t} dz + \int_0^h \frac{\partial(\rho u)}{\partial x} dz + \int_0^h \frac{\partial(\rho v)}{\partial y} dz + [\rho w]_0^h = 0 \quad (2.5)$$

Upon implementing Leibnitz's rule of integration, generally written as

$$\frac{\partial}{\partial \theta} \left[\int_{a(\theta)}^{b(\theta)} f(\theta, z) dz \right] = \int_a^b \frac{\partial f}{\partial \theta} dz + f(b, z) \frac{\partial b}{\partial \theta} - f(a, z) \frac{\partial a}{\partial \theta} \quad (2.6)$$

where the function f is u or v , θ is x or y , $b = h(x, y, t)$ and $a = 0$, the integrated continuity Equation 2.5 transforms into a powerful and tractable equation for analysis.

Under the lubrication approximation and for negligible body forces, the pressure does not vary in the film thickness direction. For the ideal gas air bearing with $\rho \propto p$, this implies that ρ is also independent of z . For the incompressible lubricant, this simplification is irrelevant because density is a constant. Applying the general boundary conditions (Equation 2.4) and Leibnitz's rule (Equation 2.6), each term in Equation 2.5 can be further evaluated.

$$\int_0^h \frac{\partial \rho}{\partial t} dz = \frac{\partial \rho}{\partial t} [z]_0^h = h \frac{\partial \rho}{\partial t} \quad (2.7a)$$

$$[\rho w]_0^h = \rho \frac{\partial h}{\partial t} + \rho u|_{z=h} \frac{\partial h}{\partial x} + \rho v|_{z=h} \frac{\partial h}{\partial y} \quad (2.7b)$$

$$\int_0^h \frac{\partial(\rho u)}{\partial x} dz = \frac{\partial}{\partial x} \left[\int_0^h \rho u dz \right] - \rho u|_{z=h} \frac{\partial h}{\partial x} + \rho u_D \frac{\partial \theta}{\partial x} \quad (2.7c)$$

$$\int_0^h \frac{\partial(\rho v)}{\partial y} dz = \frac{\partial}{\partial y} \left[\int_0^h \rho v dz \right] - \rho v|_{z=h} \frac{\partial h}{\partial y} + \rho v_D \frac{\partial \theta}{\partial y} \quad (2.7d)$$

The final integrated conservation equation is

$$\frac{\partial(\rho h)}{\partial t} + \frac{\partial}{\partial x} \left[\int_0^h (\rho u) dz \right] + \frac{\partial}{\partial y} \left[\int_0^h (\rho v) dz \right] = 0 \quad (2.8)$$

This mass conservation equation across the film thickness can be re-written in terms of mass flow rate per unit length, q :

$$\frac{\partial(\rho h)}{\partial t} + \frac{\partial q_x}{\partial x} + \frac{\partial q_y}{\partial y} = 0 \quad (2.9)$$

The mass flow rates q_x and q_y are the mass fluxes in the planar x and y directions integrated across the film.

$$\begin{aligned} q_x &= \int_0^h (\rho u) dz \\ q_y &= \int_0^h (\rho v) dz \end{aligned} \quad (2.10)$$

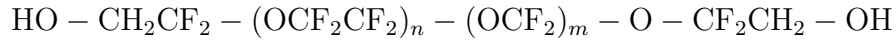
Once an expression for the mass flow rate is known, it can be inserted into Equation 2.9. The result is a single partial differential equation for the evolution of the thin film for which the detailed velocity component profiles are not needed, only the mass flow rates. For the lubricant, the mass flow rates are determined from the Navier-Stokes momentum conservation equations subject to the lubrication approximation. For the air bearing, expressions from gas dynamics based on kinetic theory and subjected to the lubrication approximation are used for q_x and q_y .

2.2 Continuum Lubrication Equation for the Lubricant

Applicability of Continuum Theory for HDD Lubricants (Perfluoropolyethers)

Perfluoropolyethers (PFPEs) are common lubricants used in the magnetic recording industry due to their favorable properties that enable them to reduce wear and friction at conventional hard drive operating temperatures throughout the drive's lifetime: chemical stability, low volatility, thermal stability, and low viscosity. Lubricant properties can be further improved and customized by adding functional end-groups, such as the hydroxyl end-groups on difunctional Zdol and tetrafunctional Ztetraol molecules that interact with the amorphous carbon overcoat through hydrogen bonding [19]. The addition of mid-chain functional groups has resulted in improved minimum clearance and evaporation properties [21]. Because of Zdol's long history in the hard drive industry and widespread use in products in the 1990s, there is much published experimental data and theoretical analysis on which to base Zdol property models in our simulation tool. So while Zdol is not in common use today or a candidate for HAMR systems, we will analyze the flow and evaporation of this conventional lubricant as a first step in predicting HAMR lubricant behavior. Specifically, we will simulate Zdol 2000; the name indicates the molecular weight of this molecule is 2000 Da = 2 kg/mol. The

backbone radius is about 0.6 nm and the chain length, if stretched out, is around 10 nm. Thus a Zdol 2000 coating on the disk surface is in some ways like a thin layer of spaghetti noodles covering a dinner plate; the polymer molecules are much longer than the polymer film thickness. The chemical structure of the Zdol molecule is



where the ratio m/n is typically between 2/3 and 1. This polymer chain is composed of a perfluorinated ether backbone terminated by hydroxyl groups. The HAMR writing system will create an adverse thermal environment for PFPE lubricants as the magnetic media is heated above its Curie temperature to 500°C with large temperature gradients due to the estimated small spot size of only 25-nm full width at half maximum (FWHM) to achieve 5 Tb/in² [12]. Thermal decomposition of bulk Fomblin Zdol occurs at temperatures above 350°C [22, 23] and evaporation of functionalized PFPEs will be significant at HAMR system temperatures [24, 25], so a new HAMR lubricant needs to be designed to achieve HDI reliability.

We are obviously pushing the limits of continuum theory by using lubrication theory to describe the lubricant. Zdol 2000 has a radius of gyration (average radius of the polymer chain over all chain conformations in a sample and over time) of 1.12 nm in Freon [20], meaning a 1-nm thick PFPE film is one or two monolayers and the discrete nature of individual molecules may be important in describing its flow. However, it has been found that continuum theory can be an adequate approach for predicting PFPE lubricant flow on a hard drive disk. Mate et al. [26] showed that the non-functional PFPE lubricant Z (CF₃ end-groups) behaved as a Newtonian fluid in air shearing experiments with a viscosity near the bulk value for thickness as small as 0.8 nm, which is thinner than its 2.7-nm diameter of gyration. In a follow-up publication, Scarpulla et al. [27] found that functional Zdol movement under air shearing is generally well described by a continuum flow process with effective viscosities for the restricted and mobile layers, even when the film thickness is less than the polymer's diameter of gyration. More recently, Marchon and Saito [28] presented fluid dynamics simulation results of non-functional Z under HAMR laser illumination conditions that agreed well with much more computationally expensive molecular dynamics simulations. Thus we will use the lubrication theory approach as a starting point for studying lubricant flow and evaporation under HAMR writing conditions. However, we must keep in mind several limitations of lubrication theory for modeling this Zdol system. No information about the microstructure and particular polymer conformation is provided by continuum theory. Factors that may be important in monolayer functional lubricants may not be illuminated by the continuum behavior studies mentioned above. Our simulations are only as good as the constitutive law (stress-strain relationship) used, the parameters for which are inferred from experiments.

Classical Reynolds Lubrication Equation for Viscous, Incompressible Fluid

The fundamental assumption of lubrication theory is that the characteristic dimension in the thickness direction h_0 is much smaller than the characteristic dimension in the length and width directions, L : $h_0 \ll L$. For the upcoming studies of lubricant deformation under HAMR writing conditions, h_0 is the initially uniform film thickness and L is the prescribed thermal spot FWHM. Additionally we assume the polymer lubricant is incompressible, which implies its density is constant, and that body forces are negligible. To determine which of the remaining terms in the momentum conservation equation are dominant, we normalize all quantities by appropriate scaling factors and impose the limit $h_0/L \rightarrow 0$ [29–31]. After this procedure, the momentum equations simplify to

$$\frac{\partial p}{\partial x} = \frac{\partial}{\partial z} \left(\mu \frac{\partial u}{\partial z} \right) \quad (2.11a)$$

$$\frac{\partial p}{\partial y} = \frac{\partial}{\partial z} \left(\mu \frac{\partial v}{\partial z} \right) \quad (2.11b)$$

$$\frac{\partial p}{\partial z} = 0 \quad (2.11c)$$

Equations 2.11a-2.11b are accurate to order h_0^2/L^2 ; Equation 2.11c is accurate to order h_0/L [29]. Viscosity varies in the x - y plane according to the local temperature and local film thickness, but μ is assumed to be independent of z for our sub-2-nm films. Integrating Equations 2.11a and 2.11b subject to the boundary conditions in Equation 2.2, we obtain the velocity profiles:

$$u = \frac{1}{\mu} \frac{\partial p}{\partial x} \left(\frac{1}{2} z^2 - hz \right) + \frac{\tau_x}{\mu} z + u_D \quad (2.12a)$$

$$v = \frac{1}{\mu} \frac{\partial p}{\partial y} \left(\frac{1}{2} z^2 - hz \right) + \frac{\tau_y}{\mu} z \quad (2.12b)$$

Inserting these profiles into the integrated mass conservation statement (Equation 2.8) and adding a source term because we consider evaporation, we arrive at the governing evolution equation for the lubricant film as

$$\frac{\partial h}{\partial t} + u_D \frac{\partial h}{\partial x} + \frac{\partial}{\partial x} \left[\frac{h^2}{2\mu} \tau_x - \frac{h^3}{3\mu} \frac{\partial p}{\partial x} \right] + \frac{\partial}{\partial y} \left[\frac{h^2}{2\mu} \tau_y - \frac{h^3}{3\mu} \frac{\partial p}{\partial y} \right] + \frac{\dot{m}}{\rho} = 0 \quad (2.13)$$

In this problem, the lubricant film thickness $h(x, y, t)$ is unknown. The lubricant shear stresses $\tau_x(x, y, t)$, $\tau_y(x, y, t)$ and pressure $p(x, y, t)$ are determined from a stress balance at the lubricant-air interface.

The lubrication assumption $h_0/L \ll 1$ has several implications, some of which have already been discussed. The assumptions for the HAMR lubricant studies are highlighted below:

- The lubricant-air interface is nearly parallel to the flat disk below (small slope): $\frac{\partial h}{\partial x}, \frac{\partial h}{\partial y} \ll 1$
- The fluid flow is approximately parallel to the bounding surface: $u, v \gg w$
- The pressure gradients along the film (x and y directions) balance the viscous shear forces. We assume that body forces are negligible. Inertia forces are shown to be negligible in the limit $h/L \rightarrow 0$.
- The fluid pressure variation in the film thickness direction is negligible.
- Fluid properties are constant through the thickness direction and can only vary in the planar directions.
- The derivatives of u and v with respect to z are much larger than all other velocity gradients: $\frac{\partial u}{\partial z} \gg \frac{\partial u}{\partial x}, \frac{\partial u}{\partial y}$ and $\frac{\partial v}{\partial z} \gg \frac{\partial v}{\partial x}, \frac{\partial v}{\partial y}$
- As phrased by Dowson [29], in a general lubrication system, the radius of curvature of solid surfaces bounding the lubricant film is large compared to the thickness of the film. In our HDD lubricant system, we assume the lubricant covers a flat magnetic recording disk, so this assumption of lubrication approximation is automatically satisfied. However, current production disks have a root-mean-square roughness around 0.34 nm according to AFM measurements [32, 33], so disk roughness may be important to include in future simulations of 1–2-nm-thick lubricants.

2.3 Slip Correction from Kinetic Theory for the Air Bearing

The HDD industry relies on fast air bearing simulation tools that are reasonably accurate to design ABS surfaces for desired flying performance, diagnose failure issues, and other tasks that save time and money in the development and production of hard disk drives. Direct simulation methods such as molecular dynamics simulations or direct simulation Monte Carlo methods are so detailed as to be computationally intensive even for simple, flat slider geometries. To achieve slider-level air bearing simulation with sufficient accuracy, a lubrication equation with rarefaction corrections that can be solved efficiently with established numerical methods for nonlinear partial differential equations is desired.

Gas Flow Regimes

The magnitude of the Knudsen number, the ratio of the mean free path of a gas and a characteristic length dimension $\text{Kn} \equiv \lambda/h$, indicates whether a statistical mechanics (kinetic theory) or continuum mechanics formulation of the governing balance equations should be used for analysis of a gas system. When the mean free path is comparable to a physical

length scale over which large variations in macroscopic quantities can take place, the continuum hypothesis is not a valid assumption. The discrete nature of the gas molecules becomes important as collisions are less frequent, leading to the break down of the constitutive equation; a statistical mechanics formulation should be used. A dilute gas for which the length of the mean free path is not negligible is called a rarefied gas.

It is generally agreed that continuum theory is sufficiently accurate for dense gases in the range $\text{Kn} \leq 0.01$, and kinetic theory applies for very dilute (rarefied) gases in free molecular flow with infrequent collisions in the range $\text{Kn} \geq 10$ [34]. Empirical information suggests that first-order velocity slip and temperature jump boundary conditions can extend the applicability of continuum fluid dynamics equations in the slip regime $0.01 < \text{Kn} < 0.1$, and higher order slip corrections may be adequate in the transition regime $0.1 < \text{Kn} < 10$ [35]. The limits of the slip and transition regimes may depend on the problem geometry. For the problem of the HDD air bearing, a first-order slip model [36] and second order slip model [37] have been found to be accurate up to a certain point. A more sophisticated slip correction derived from the linearized Boltzmann equation [18, 38] called the molecular gas lubrication (MGL) equation or the generalized Reynolds equation is used in this dissertation. It is the most commonly used air bearing model in the HDD industry, and it is considered to be sufficiently accurate for ABS design.

Fukui and Kaneko's MGL equation [18] is useful for air bearing simulations because it is valid for an arbitrary Knudsen number regime. At standard temperature and pressure, the mean free path of air molecules is $\lambda = 65$ nm. Under the flying slider, the physical spacing between the slider and disk varies with ABS etch depth and pitch angle from several microns to less than 5 nm. The slider studied in this report has a maximum spacing under regions with the maximum base etch depth of $1.651 \mu\text{m}$ ($\text{Kn} \approx 0.04$, slip regime) and the minimum flying height less than 2 nm ($\text{Kn} \approx 30$, free molecular flow); hence the air bearing experiences several gas flow regimes.

Molecular Gas Lubrication Equation for HDD Air Bearing

The Boltzmann equation governs fluidic and thermal gas transport for a gas such as an HDD air bearing over the entire Knudsen number regime and for non-equilibrium conditions [39]. The behavior of the velocity distribution function of gas molecules is governed by this integro-differential equation: the velocity distribution function varies along a molecular path due to intermolecular collisions. Macroscopic quantities such as density, flow velocity, temperature, and stress are defined as moments of the velocity distribution function. Rarefied gases are composed of three fundamental flows: pressure-gradient-driven Poiseuille flow, shear-driven Couette flow due to relative motion between the bounding surfaces, and boundary-temperature-gradient-driven thermal creep (transpiration) flow that only arises in rarefied gas flows. See Sone's molecular gas dynamics book [40] for a through explanation of the Boltzmann equation and these fundamental flows.

There have been various derivations of non-dimensional expressions for these elemental flow rates that used a simplified linearized Boltzmann equation that employs the BGK model

for the collision integral and idealistic gas-solid interactions at the boundaries [41, 42]. These flow rate expressions are valid for flows with small pressure and temperature gradients and apply over the entire rarefaction range—continuum to free molecular flow. The flow rates depend on the local Knudsen number and the surface properties of both bounding surfaces, represented by the phenomenological surface accommodation coefficient α . For symmetric boundaries that have the same surface properties and therefore the same accommodation coefficients, the shear-driven Couette flow rate Q_C is always unity. In this dissertation, the slider and disk surfaces are assumed to be symmetric with a perfectly diffuse surface, so Q_C is always equal one and Couette flow is independent of rarefaction effects.

The technique of integrating a mass conservation equation across a film thickness is not limited to a Newtonian fluid; it can be used for a rarefied gas as well. Fukui and Kaneko [18] assumed the lubrication approximation and diffuse reflection at the boundaries to analytically decompose the linearized BGK-Boltzmann equation into expressions for the fundamental flows, the flow rates for which have been reported by others [41, 42]. By inserting the expressions for the rarefied gas mass flow rates into Equation 2.9, they obtained what has been called the generalized Reynolds equation or molecular gas lubrication equation because it applies of the entire Knudsen number regime. The non-dimensional MGL equation is

$$\begin{aligned} \sigma \frac{\partial}{\partial \tau} \left(\frac{PH}{\bar{T}} \right) + \frac{\partial}{\partial X} \left[\frac{1}{\bar{T}} \left(\Lambda_{x,0} PH - \frac{PH^3}{\bar{\mu}} \bar{Q}_P \frac{\partial P}{\partial X} + \frac{P^2 H^3}{\bar{\mu} \bar{T}} \bar{Q}_T \frac{\partial \bar{T}_w}{\partial X} \right) \right] \\ + \frac{\partial}{\partial Y} \left[\frac{1}{\bar{T}} \left(\Lambda_{y,0} PH - \frac{PH^3}{\bar{\mu}} \bar{Q}_P \frac{\partial P}{\partial Y} + \frac{P^2 H^3}{\bar{\mu} \bar{T}} \bar{Q}_T \frac{\partial \bar{T}_w}{\partial Y} \right) \right] = 0 \end{aligned} \quad (2.14)$$

where the non-dimensional squeeze number and bearing numbers in the x and y directions are defined as

$$\sigma = \frac{12\mu_0\omega_0 L^2}{p_0 h_m^2} \quad (2.15a)$$

$$\Lambda_{x,0} = \frac{6LU\mu_0}{p_0 h_m^2} \quad (2.15b)$$

$$\Lambda_{y,0} = \frac{6LV\mu_0}{p_0 h_m^2} \quad (2.15c)$$

The non-dimensional quantities are $X = x/L$, $Y = y/L$, $Z = z/h_m$, $H = h/h_m$, $P = p/p_0$, $\bar{\mu} = \mu/\mu_0$, $\bar{T} = T/T_0$, and $\tau = \omega_0 t$. The subscript ‘0’ denotes ambient conditions. Here \bar{T} is temperature and τ is time. L is the characteristic lubrication region length, the slider length in the case of an air bearing simulation. h_m is a reference clearance at the slider’s trailing edge center (TEC). U and V are the planar direction disk speeds from the perspective of the slider as determined from the skew angle. $\Lambda_{x,0}$, $\Lambda_{y,0}$ are system parameters, constant for a particular head-disk system with a constant rotational speed because they depend on ambient properties. $\frac{\partial \bar{T}_w}{\partial X}$, $\frac{\partial \bar{T}_w}{\partial Y}$ are the boundary wall temperature gradients. ω_0 is a characteristic angular frequency equivalent to the disk rotational speed. \bar{Q}_P , and \bar{Q}_T

are the relative non-dimensional flow rates for Poiseuille, and thermal creep flow determined from kinetic theory [41, 42].

The term containing \overline{Q}_T in Equation 2.14 is due to a rarefied gas phenomenon called thermal creep or thermal transpiration. A tangential temperature gradient along a channel wall can drive flow in a rarefied gas from *cold to hot* regions if the thickness of a channel is comparable in magnitude to the mean free path. The interaction of the gas molecules with the solid boundary walls is significant. The qualitative difference in the velocity distribution functions of the molecules impinging the boundary from the 'hot' and 'cold' sides plays an essential role in a difference in momentum transfer that induces thermal creep flow [40].

To make their generalized lubrication equation directly comparable to the classical Reynolds equation (Equation 2.13), Fukui and Kaneko normalized the non-dimensional Poiseuille and thermal creep flow rates by the Poiseuille flow rate in continuum lubrication flow, $Q_{con} = D/6 = \sqrt{\pi}/(12Kn)$, thereby defining relative flow rates: $\overline{Q}_P \equiv Q_P/Q_{con}$, $\overline{Q}_T \equiv Q_T/Q_{con}$. So in the continuum limit, their equation reduces to the classical Reynolds equation in non-dimensional form because $Kn \rightarrow 0 \Rightarrow \overline{Q}_P \rightarrow 0$, $\overline{Q}_T \rightarrow 0$.

Equation 2.14 is the same equation as Fukui and Kaneko's molecular gas lubrication equation for large temperature differences [38] except for the bearing number. They defined the bearing number in terms of local viscosity, e.g. $\Lambda_x = \frac{6LU\mu}{p_0h_m^2}$. Since we consider here local air bearing heating due to heat dissipated by the laser delivery system embedded in the slider body, we allow for the viscosity changes with temperature and hence location on the slider. Therefore we choose here to define the bearing number in terms of constant characteristic quantities. The change in viscosity is incorporated with the Poiseuille and thermal creep flow terms.

The MGL equation has been shown to agree well with direct simulation Monte Carlo (DSMC) methods for simple flat slider geometry, i.e. for a slider with no etched ABS design. Alexander et al. [43] showed that the close agreement between DSMC and MGL numerical solutions for a 5- μm long, infinitely wide flat slider with minimum flying heights of 15 nm and 50 nm. Huang et al. [44] reported the MGL and DSMC air bearing force and pressure profile agreed within a maximum relative difference of $< 4\%$ for a for 4- μm long, 3.3- μm wide slider with a minimum flying height varying from 2–25 nm. As the bearing number increases, such as with a faster disk speed or lower flying height, the Couette flow term that is independent of the Knudsen number becomes dominant; in other words, the influence of rarefaction effects could be small when the Couette flow dominates [18, 44]. So at the small spacings simulated here, around 0.9–2-nm physical spacing between the slider and disk, the high bearing number is expected to dominate. The error incurred by using the Fukui and Kaneko's sophisticated slip correction of the Reynolds lubrication equation is not expected to be significant.

Before concluding this chapter, the assumptions used to derive the MGL equation are emphasized below.

- The lubrication approximation is used: the gas film thickness is much smaller than the slider's length and width, and the flow velocity in the thickness direction is negligibly small. Under this thin-film assumption, the total flow of the rarefied gas can be

decomposed into fundamental flows of Poiseuille (pressure gradient driven), Couette (relative motion between the bounding surfaces), and thermal creep (due to tangential temperature gradients in bounding surfaces).

- The rarefied gas is assumed to deviate only slightly from static, isotropic equilibrium so that the Boltzmann equation can be linearized. That is, macroscopic velocities, pressure gradients, and tangential temperature differences in the lubrication film are small. The gas flow velocities are small compared with the molecular thermal velocities, i.e. the flow Mach number is small.
- The linearized Boltzmann equation is not a rigorous mathematical linear approximation of the true solution; terms higher than second order have been merely neglected. There is no mathematical derivation to assure the linearized Boltzmann equation solution approaches the full Boltzmann equation solution as the small parameter approaches zero [40].

Chapter 3

Air Bearing Model and Numerical Solver

3.1 CMLAir-HAMR Air Bearing Solver

CMLAir is an air bearing simulation tool developed in the Computer Mechanics Laboratory at the University of California, Berkeley to solve the isothermal molecular gas lubrication (MGL) equation [45, 46]. Hard drive companies use CMLAir or a similar MGL numerical solver to design slider air bearing surfaces. CMLAir-HAMR is a modification of CMLAir for non-isothermal conditions expected for HAMR sliders. CMLAir predicts the slider's flying attitude (flying height, pitch and roll angles) according to the air bearing force that balances a given suspension load as depicted in Figure 3.1. The equation is discretized using a control volume formulation [47], setting up a system of linear equations that is solved using a quasi-Newton iteration method [48]. A V-cycle multi-grid method and alternating direction implicit line-sweep method speed up convergence, and the mass flux averaging technique allows for arbitrary ABS rail designs with multiple recesses. Thermal flying height control (TFC) protrusion can be incorporated into the simulation by specifying the height to be added to the air bearing surface (ABS) over a certain area. There are static and dynamic versions of CMLAir and CMLAir-HAMR.

There are three major changes made to CMLAir to create CMLAir-HAMR:

1. Non-isothermal governing equation: The original CMLAir solves the MGL equation that is simplified for isothermal conditions:

$$\sigma \frac{\partial(PH)}{\partial\tau} + \frac{\partial}{\partial X} \left(\Lambda_x PH - PH^3 \bar{Q}_P \frac{\partial P}{\partial X} \right) + \frac{\partial}{\partial Y} \left(\Lambda_y PH - PH^3 \bar{Q}_P \frac{\partial P}{\partial Y} \right) = 0 \quad (3.1)$$

For CMLAir-HAMR, the control volume discretization is modified to add terms that

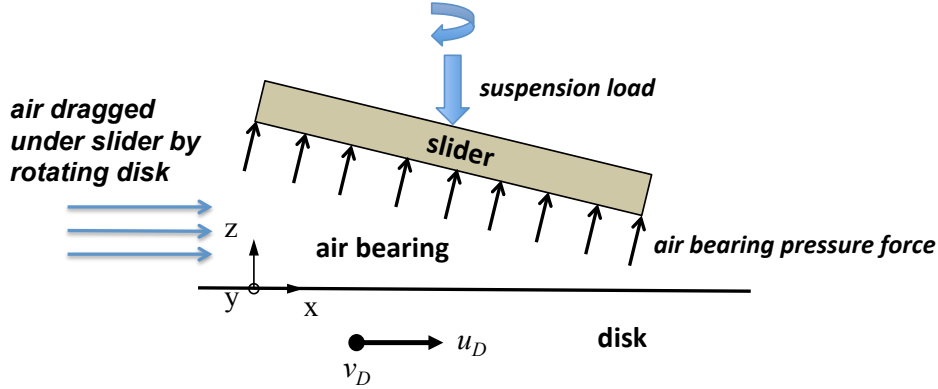


Figure 3.1: Working principle of a hard disk drive air bearing. Air bearing simulation programs such as CMLAir-HAMR predict the pressure profile under the slider and the resulting flying attitude that balances a given suspension load.

represent the general non-isothermal MGL equation, repeated from Section 2.3:

$$\begin{aligned} \sigma \frac{\partial}{\partial \tau} \left(\frac{PH}{\bar{T}} \right) + \frac{\partial}{\partial X} \left[\frac{1}{\bar{T}} \left(\Lambda_{x,0} PH - \frac{PH^3}{\bar{\mu}} \bar{Q}_P \frac{\partial P}{\partial X} + \frac{P^2 H^3}{\bar{\mu} \bar{T}} \bar{Q}_T \frac{\partial \bar{T}_w}{\partial X} \right) \right] \\ + \frac{\partial}{\partial Y} \left[\frac{1}{\bar{T}} \left(\Lambda_{y,0} PH - \frac{PH^3}{\bar{\mu}} \bar{Q}_P \frac{\partial P}{\partial Y} + \frac{P^2 H^3}{\bar{\mu} \bar{T}} \bar{Q}_T \frac{\partial \bar{T}_w}{\partial Y} \right) \right] = 0 \quad (3.2) \end{aligned}$$

2. ABS temperature input file: When numerically solving the Equation 3.2, we assume the slider and disk temperature distributions are known and are inputs to the simulation. These bounding surface temperatures are used to estimate the air bearing temperature. The temperature of the air at a particular point (x, y) under the slider is estimated to be the average of the disk and slider temperature at that point, a reasonable first approximation:

$$\bar{T}(x, y) = \frac{1}{2} \left(\frac{T_s(x, y) + T_d(x, y)}{T_0} \right) \quad (3.3)$$

In order to determine the air temperature variation across the film or a better estimate for $\bar{T}(x, y)$, one would use kinetic theory [49]. Because the thermal spot on the disk is much smaller than the slider, the disk is assumed to be at ambient temperature for air bearing simulations. The non-dimensionalized temperature gradient is the average of the non-dimensionalized slider and disk temperature gradients at that point as suggested by Fukui and Kaneko [18]. The user specifies an ABS temperature input file similar to the thermal protrusion input file.

3. \bar{Q}_T database and new flow rate coefficient evaluation method: The flow rate coefficients determined from kinetic theory, \bar{Q}_P and \bar{Q}_T , depend on the local pressure P , spacing or flying height H , and temperature \bar{T} through the Knudsen number (more

explanation below). The local flow rate coefficients are quickly obtained at each location on the slider by interpolating in a database created at the beginning of the simulation. To implement the non-isothermal MGL equation for CMLAir-HAMR, we added a \bar{Q}_T database. A improved technique to evaluate the flow rate coefficients that uses a Chebyshev polynomial expansion to evaluate the the Abramowitz function is implemented that is accurate for both \bar{Q}_P and \bar{Q}_T [50].

Air Bearing Model

In order to solve the governing equation of the air bearing, we need to know the local air viscosity and mean free path. Both depend on local pressure and temperature according to the hard sphere model. In the derivation of their generalized molecular gas lubrication equation, Fukui and Kaneko [18] modeled the air molecules as hard spheres that obey the ideal gas law, a common model used in kinetic theory. For hard spheres with velocity distributed according to the Maxwellian distribution, the distance between collisions (mean free path λ) is inversely related to the distance squared between the molecules d and the number density of molecules N [51]. Number density can be expressed in terms of the density and mass of the individual molecules: $\rho = Nm_i$ where N is the number of molecules per unit volume, m_i is the mass of an individual molecule and density ρ has units of mass per unit volume.

$$\lambda = \frac{1}{\sqrt{2}\pi d^2 N} = \frac{m_i}{\sqrt{2}\pi d^2 \rho} \quad (3.4)$$

By considering the air to be an ideal gas, we can relate the density to the local gas temperature T and pressure p by the ideal gas law (equation of state) of the form:

$$p = \rho \frac{R}{M_w} T \quad (3.5)$$

where p is the gas pressure, $R = 8.314462$ J/mol/K is the universal gas constant, M_w is the molecular weight or molar mass (moles per unit mass), and T is the gas temperature. Substituting Equation 3.5 into Equation 3.4, we obtain

$$\lambda = \frac{m_i R T}{\sqrt{2}\pi d^2 M_w p} \quad (3.6)$$

Therefore, in the air bearing of a hard disk drive, the mean free path of the air molecules is assumed to be proportional to the local temperature and inversely proportional to the local pressure. It follows that for a given gas (constant m_i , d , and M_w), the ratio of local mean free path λ to its ambient value λ_0 can be expressed in terms of the ratios of local temperature and pressure, T and p , to ambient temperature and pressure, T_0 and p_0 :

$$\frac{\lambda}{\lambda_0} = \frac{T}{T_0} \frac{p_0}{p} \quad (3.7)$$

In the original isothermal CMLAir, only the local pressure effect on mean free path is considered: $\lambda = \lambda_0(p_0/p)$. Recalling that $\text{Kn} \equiv \lambda/h$, we can relate the ratio of the local Knudsen number to the reference Knudsen number to the ratios of the local and reference pressure, temperature, and air bearing thickness:

$$\frac{\text{Kn}}{\text{Kn}_0} = \frac{T}{T_0} \frac{p_0}{p} \frac{h_0}{h} \quad (3.8)$$

The non-dimensional mass flow rates \bar{Q}_P and \bar{Q}_T are functions of the Knudsen number and the surface accommodation coefficient α for the slider and disk. For simplicity, both bounding surfaces are assumed perfectly diffuse ($\alpha = 1$). Therefore only the dependence of the flow rates on the Knudsen number needs to be considered. The local mass flow rates are evaluated at the local Knudsen number:

$$\bar{Q}_P(\text{Kn}) = \bar{Q}_P \left(\text{Kn}_0 \frac{\bar{T}}{PH} \right), \quad \bar{Q}_T(\text{Kn}) = \bar{Q}_T \left(\text{Kn}_0 \frac{\bar{T}}{PH} \right) \quad (3.9)$$

where \bar{T} , P , and H are the non-dimensional temperature, pressure, and air bearing thickness.

The air viscosity, a function of temperature, is calculated from the estimated air bearing temperature using Sutherland's Formula for the viscosity of a gas. Sutherland proposed a model that considered gas molecules to be hard spheres and added a weak attractive force between the molecules that decays rapidly with distance; his hypothesis is adequate over a wide range of temperatures for many gases, including air [51, 52].

$$\bar{\mu} = \frac{\mu}{\mu_0} = \left(\frac{T}{T_0} \right)^{3/2} \left(\frac{T_0 + C}{T + C} \right) \quad (3.10)$$

where μ_0 is a known viscosity at a known absolute temperature and Sutherland's constant C is fit to the data. For air, the reference viscosity at the reference temperature $T_0 = 273.15$ K is $\mu_0 = 1.71\text{e-}5$ kg/m/s and the empirically fitted constant is $C = 110.4$ K [52].

We will consider conductive heat transfer from the air bearing surface. Zhang and Bogy [53] developed an expression for the conductive heat flux at the ABS, $q_{cond}|_{\text{ABS}}$ (units W/m²), by solving the energy equation and applying temperature jump boundary conditions (first order slip theory). Viscous dissipation can also contribute to the heat flux at the ABS, but the conduction contribution to the heat flux is larger by 1–2 orders of magnitude for TFC sliders, for which the ABS temperature increases only tens of degrees Celsius above ambient temperature [54]. We disregard the viscous dissipation for now, but it may be worth investigating the magnitude of viscous dissipation for HAMR sliders because the near-field transducer at the ABS may experience hundreds of degrees temperature increase during writing. Chen et al. [55] later improved this model to account for the close proximity of two bounding surfaces on the mean free path as well as expressions for viscous dissipation. For all simulations in this work, we consider only the heat transfer due to conduction at the ABS using the following expression [53]:

$$q_{cond}|_{\text{ABS}} = -k_{air} \frac{T_s - T_d}{h + 2 \frac{2 - \sigma_T}{\sigma_T} \frac{2\gamma}{\gamma + 1} \frac{\lambda}{Pr}} = H_{film}(T_s - T_d) \quad (3.11)$$

where k_{air} is the air's thermal conductivity, T_s and T_d are the local temperatures of the slider and disk that bound the air bearing, σ_T is the bounding surface thermal accommodation coefficient, γ is the ratio of specific heats of air, Pr is the Prandtl number, λ is the air's mean free path, and h is the local spacing between the slider and disk, i.e. the flying height. For all simulations in this work, we will use $k_{air} = 0.0262$ W/(m·K), $Pr = 0.7145$, $\gamma = 1.4015$, and we assume perfectly diffuse surface collisions ($\sigma_T = 1$). Unless otherwise noted, we use the modified mean free path expression from [55] that accounts for the close proximity of the bounding surfaces. The mean free path is the average distance traveled by freely moving gas molecules between collisions at equilibrium; however in the head-disk interface, the motion of air molecules is constrained by the presence of the closely spaced slider and disk.

3.2 Iterative Static Solver

The flying attitude and thermal deformation solutions of a TFC slider or HAMR slider must be solved by an iterative approach. The air bearing and slider thermal deformation solutions are related to each other through boundary conditions at the ABS (heat transfer coefficient and pressure, temperature and protrusion). CMLAir-HAMR predicts the pressure profile and flying attitude of a slider for a given suspension load, slider thermal protrusion profile, and the ABS temperature profile, a new feature for CMLAir-HAMR. The thermal protrusion due to specified heat generating components can be determined from a finite element solver such as ANSYS where the heat transfer boundary conditions and the pressure force at the air bearing surface depend on the slider's flying attitude and pressure profile.

An iterative solver between commercial finite element software ANSYS and the static version of CMLAir-HAMR are developed, based on the CML TFC code [56]. Macro files written in the ANSYS Parametric Design Language pass boundary conditions between ANSYS and CMLAir-HAMR. Figure 3.2 shows the flowchart of the Iterative Static Solver procedure. First CMLAir-HAMR is solved to obtain an initial pressure profile and spacing profile (flying height) under the slider. The heat transfer coefficient at the ABS surface H_{film} is calculated according to Equation 3.11. The heat transfer coefficient and pressure profile are boundary condition inputs to the coupled field analysis performed in ANSYS. The user specifies the TFC heater power and the amount of heat dissipated in the laser delivery system components. The updated ABS protrusion and temperature profiles are inputs into the next CMLAir-HAMR simulation, and updated pressure and spacing profiles are obtained. The iterations between ANSYS and CMLAir-HAMR continue until the flying height obtained from two consecutive iterations is within a specified tolerance (0.05 nm).

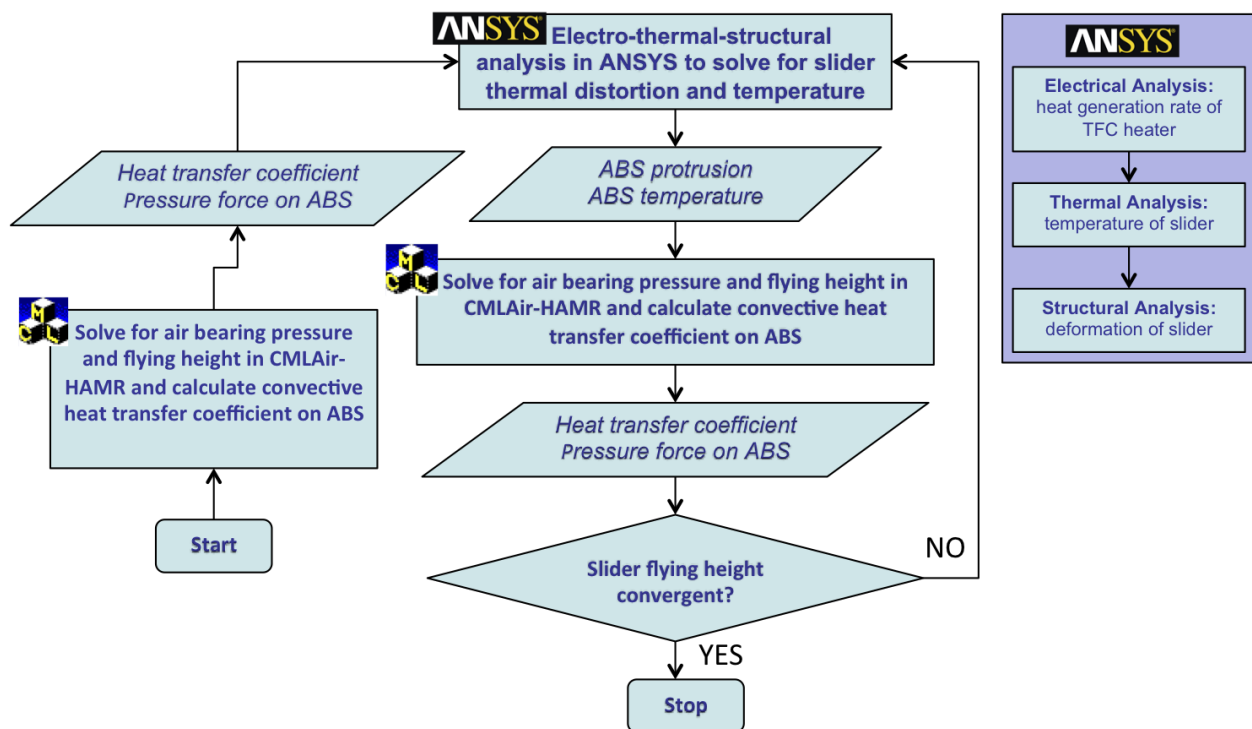


Figure 3.2: Flowchart of the CMLAir-HAMR Iterative Static Solver. The purple box shows the flow of the ANSYS coupled field analysis.

Chapter 4

Static Slider Air Bearing Behavior in HAMR under Thermal Flying Height Control and Laser System Induced Protrusion

4.1 Introduction

In this chapter we use the general non-isothermal equation in the air bearing solver to evaluate how the laser delivery system can impact the slider's flying attitude and read/write performance. A detailed HAMR slider model is not available (for proprietary reasons—if a HDD company has a reliable HAMR slider design, they would not tell their competitors and it would be in product development!). First we describe a simplified HAMR slider model of our own design. We use the iterative static solver to evaluate the effect of various factors on the predicted slider flying height: the components of the integrated laser delivery system and the new features added to create CMLAir-HAMR (thermal creep, lateral air temperature variation).

Seagate and HGST (now a division of Western Digital) presented experimental and simulation results of a HAMR slider with an integrated laser delivery system but with several design details omitted for competitive reasons. Challener et al. [13] reported that the HAMR heads with an integrated laser delivery system lasted only tens of track recordings and the exact failure mechanism was unknown. They mentioned that modeling indicated the NFT temperature increased by several hundred degrees to a value below the melting point of gold, so no information or conjecture about the cause of failure was provided. Stipe et al. [14] presented intriguing magnetic writing demonstrations that couple HAMR technology with another high density recording technology, bit patterned media. In both publications, finite element simulations were used to solve Maxwell's equations to determine the electromagnetic field intensity distribution in the waveguide, near-field transducer (NFT), and the media to

predict the laser delivery system's efficiency. Neither paper discusses in detail the thermal effects of the laser delivery system or the impact of the high temperatures and temperature gradients on the air bearing and the slider's flying ability.

Even though no production HAMR slider exists for research purposes, a few experimental and simulation studies have been published that investigate thermal issues for sliders under HAMR conditions. Xu et al. [57] measured the effect of a pulsed laser on the slider's flying dynamics; the slider's vibration amplitude was about 0.2 nm for their 130–170 kHz pulsed laser which their continuum-based finite element analysis showed was mostly due to the disk surface thermal expansion. For these studies, the laser was optically focused through the glass substrate onto the back of the magnetic layer with a maximum media temperature estimated to be 100°C, so the laser delivery system was not integrated into the slider and no NFT was present to confine the laser energy below the diffraction limit. The write pole and the NFT should be in close proximity so the thermal and magnetic fields are aligned for HAMR writing. Seigler et al. [15] presented an analysis of the system using Maxwell's equations that demonstrated that integrating the magnetic and optical field delivery components will be difficult—the magnetic material needed for the write pole will interfere with the electromagnetic field in the nearby waveguide, absorbing some of electromagnetic energy that will increase the write pole's temperature and add to the slider's thermal deformation. Zheng et al. [58] used an iterative static solver to predict the flying attitude of a sophisticated slider with dual thermal flying height control (TFC) heaters, read and writer elements, and two laser delivery system components, the waveguide and NFT. The only heat dissipating components were the two heaters and the waveguide. The dual heater design could compensate for waveguide-induced thermal protrusion if the power dissipated in the waveguide was less than the heater powers.

A series of papers from the Data Storage Institute in Singapore investigated the impact of an integrated laser delivery system on the slider's thermal deformation. Xu et al. [16] present a thermal analysis of the most detailed integrated HAMR slider model to date that includes a laser diode, waveguide, coupling prism, and NFT as well as the suspension to which the slider is attached. However, in their model there is no TFC heater. The change in the NFT temperature in this work was only 1°C when the minimum flying height decreased from 10 nm to 4 nm. In another study, Xu et al. [59] simulated a NFT efficiency of 2–3% and found that the NFT absorbed 10–25% of the incident energy from the waveguide. The presence of the write pole was also studied where the write pole was assumed to absorb 10–30% of the energy in the waveguide: the NFT temperature increased over 200 °C when the distance between the write pole and NFT reduced from 50 nm to 10 nm. In [60], the dynamic thermal response of HAMR head components to a pulsed laser was investigated numerically. They found that the NFT protrusion does not follow the rapid temperature change of the pulsed laser. The NFT protrusion response time was 2–3 ms while the temperature response time is only 2 μ s. The rest of the slider body demonstrated temperature response times of about 1 s.

All the previous studies mentioned above have focused on the details of heat transfer within the slider body and laser delivery system but not on the thermal effects on the

air bearing. If the air bearing was included, either the same air bearing solver designed for traditional non-HAMR sliders was used or a flying attitude and pressure profile were assumed. In this chapter we focus on the air bearing model in addition to the effect of various HAMR slider components. This work is meant to be a qualitative study of HAMR air bearing performance. A more accurate analysis would require a more accurate HAMR slider design, which may only be available after a HAMR product is on the market.

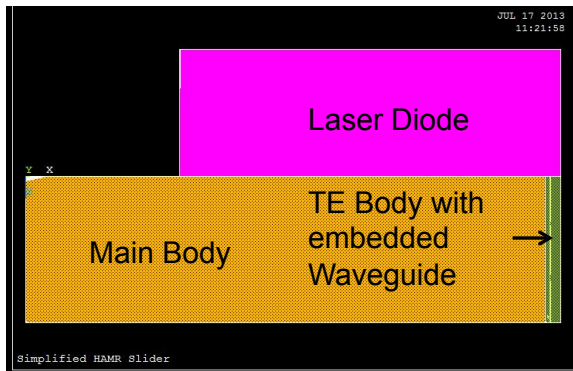
4.2 Simplified HAMR Slider

The HAMR laser delivery system is made up of several components in series that confine the energy of a 700–850-nm laser beam (electromagnetic waves) down an intensity profile spot on the magnetic media less than 100-nm FWHM to generate the thermal spot required for HAMR writing. The source of the electromagnetic wave is a laser diode separate from the slider or possibly mounted on to the back side of the slider, i.e. the side opposite the ABS. The laser beam is focused using traditional optical means onto the end of a waveguide. The waveguide confines the energy and delivers it to the near-field transducer (NFT). The waveguide is made of a dielectric material assumed to transfer the electromagnetic energy without absorbing any energy. At the surface of the metallic NFT, it is conjectured that the incident optical field excites surface plasmons, which are collective oscillations of electrons. The oscillating charges generate an electric field whose intensity exponentially decays with distance from the interface [61]. These oscillations couple with the electrons in the magnetic media in close proximity and transfer energy. The components likely to dissipate significant amounts of energy are the NFT, the laser diode, and the write pole.

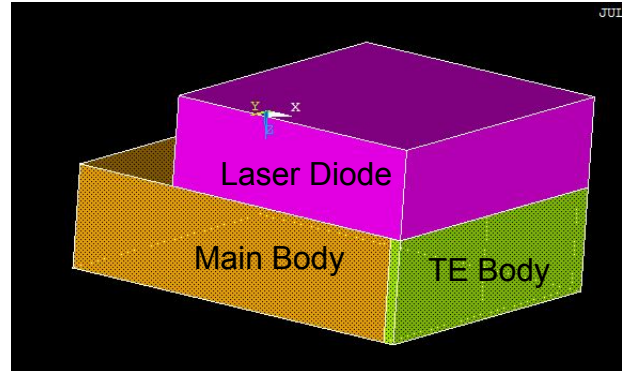
Two integrated HAMR head recording demonstrations have been published. Seagate investigators sketched out the design of a planar solid immersion lens (waveguide) that focuses the electromagnetic energy onto a ‘lollipop’ NFT, and in this paper the authors demonstrated HAMR writing with an areal density of ~ 0.24 Tb/in² [13]. They reported the gratings (waveguide) are 50% efficient, and the electromagnetic simulation results showed coupling efficiency of 8% for the NFT (incident focused optical power to the region on the disk). Authors from HGST proposed an ‘E-antenna’ NFT design, and they demonstrated improved storage capacity up to ~ 1 Tb/in² when the HAMR system was coupled with another developing hard drive technology, bit patterned media [14]. They mentioned that the optical efficiency from the objective lens (the entrance of the waveguide) to the start of the NFT was 40%, and they reported simulation results showing 12.8% of the energy in the NFT was absorbed by the medium. So the entire laser delivery system was only about 1% efficient at transferring the electrical energy supplying the laser diode to the recording bit on the disk. Thus 99% of the energy did not make it to the disk in their system, and a significant portion was likely dissipated as heat in the hard disk drive.

Here we develop a simplified HAMR slider design with important laser delivery system components in addition to a thermally actuating heater to perform early stage HAMR slider flying behavior analysis. We create a simple HAMR slider finite element model (Figure 4.1)

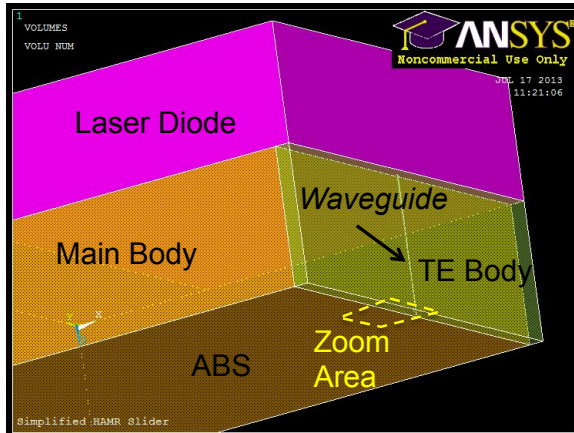
and use an existing ABS rail design from a production TFC slider for the air bearing simulations (Figure 4.2). In order to work with a reasonable number of nodes, we do not include the etched ABS design in the finite element model; the etch depth dimensions (2.5 nm–1.6 μm) are small compared to most of the other mechanical dimensions of the slider. The thermal deformation determined by the finite element solver is merely added to the ABS etched design in the air bearing solver. The finite element model components are simply joined together with no interface thermal resistances. The displacements and temperatures



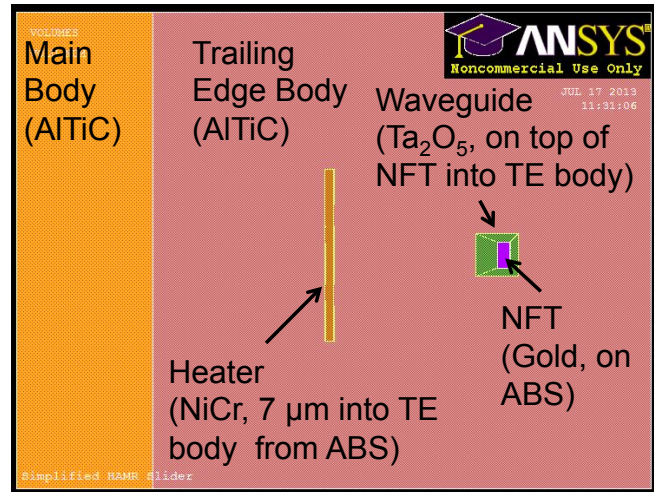
(a) Side view



(b) Oblique view



(c) Oblique view with ABS zoom area labeled



(d) ABS zoom near the trailing edge

Figure 4.1: The simplified HAMR slider finite element model used in all simulations. The trailing edge (TE) body contains the embedded waveguide and near field transducer (NFT). The bottom of the NFT is on the air bearing surface (ABS). The heater is embedded into the TE body 7 μm from the ABS. The laser diode is attached to the back of the slider, opposite the ABS.

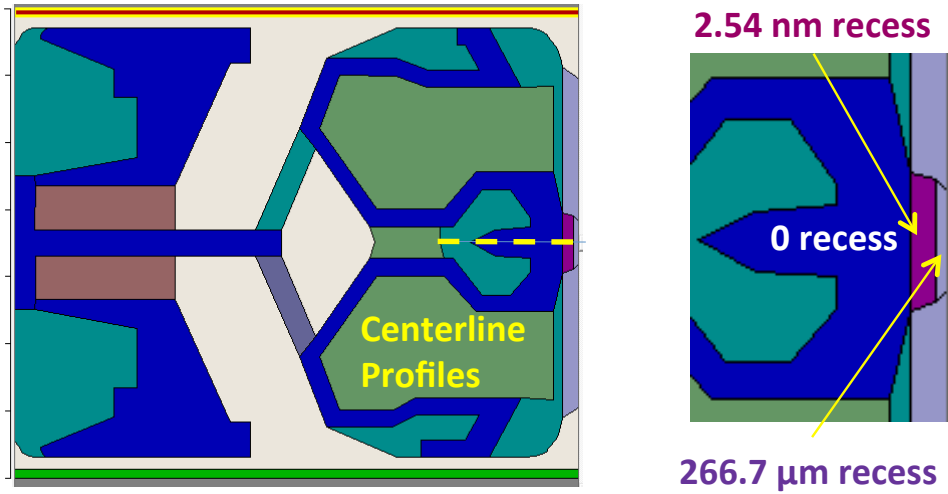


Figure 4.2: ABS rail design used in CMLAir-HAMR and location of centerline plots. The colors reflect different etch depths. The base etch depth (deepest recess) of the ABS design is $1.651 \mu\text{m}$. The center of the trailing edge is shown in detail. The trailing edge region contains the read and write transducers and the NFT. The yellow dashed line indicates the location of centerline profiles shown in upcoming sections.

of shared nodes are assumed to be equal.

We use bulk material properties for all the slider's components even though thin-film effects are likely important, especially around the NFT. The bulk of the slider is made of aluminum-titanium-carbon (AlTiC), a common substrate for air bearing sliders. The trailing edge portion of the slider with the embedded thermal fly height control heater is made of alumina (Al_2O_3) which is often used as an electrical insulator in integrated circuits. Nichrome (NiCr) is a high resistivity, non-magnetic alloy used for the TFC heater resistance wire that performs the electric heating. The NFT is made of gold (Au), a metal that supports surface plasmons. The diode is made of gallium arsenide (GaAs), a common semiconductor material use in near-infrared laser diodes. Tantalum pentoxide (Ta_2O_5) is used for the waveguide material due to its high refractive index contrast and low absorption properties that allow for strong confinement of light with low propagation losses; thin-film thermoelastic properties for Ta_2O_5 are used according to measurement from [62].

Around 0.5 mW of energy is expected to be needed to heat a magnetic bit region of a FePt magnetic disk in HAMR writing [16]. Diodes generally convert about 50% of the input electrical power into electromagnetic wave energy (laser beam), and we assume that the remaining 50% is dissipated as heat in the diode. The overall optical efficiency from the exit of the laser diode to the entrance of the NFT is around 40% due to coupling losses [14]. The NFT is about 5% efficient, and it absorbs about 10–20% of the energy delivered by the waveguide [59]. Figure 4.3 summarizes the light delivery pathway and regions of expected

Table 4.1: Simplified HAMR slider component material properties. The properties are k thermal conductivity, α_T thermal expansion coefficient, E Young’s modulus, ν Poisson’s ratio, and ρ electrical resistivity.

Component	Material	k W/(m·K)	α_T K ⁻¹	E GPa	ν –	ρ Ωm	Dimensions μm
Main Body	AlTiC	24.5	7.7e-6	390	0.24		$818.5 \times 700 \times 230$
TE Body	Al ₂ O ₃	1.3	7.5e-6	200	0.23		$25 \times 700 \times 230$
Heater	NiCr	13.4	14e-6	165	0.3	1.0414e-6	$0.3 \times 4 \times 4$
NFT	Au	318	14.2e-6	79	0.44		$0.3 \times 0.6 \times 0.1$
Waveguide	Ta ₂ O ₅	57.5	4.4e-6	136	0.27		$1 \times 1 \times 229.9$
Laser Diode	GaAs	33	5.7e-6	85.9	0.31		$600 \times 700 \times 150$

heat dissipation. The heat generations in the NFT and the diode are assumed to be uniform. The diode would likely be adhered to the the back of the slider by some means, but we do not include a boundary thermal resistance between the slider and disk or between any other slider components at this time. Analysis with Maxwell’s equations shows that the magnetic write pole absorbs a 10–40% of the energy from the waveguide and dissipates that energy as heat [15]. However, for simplicity we are excluding the read and write elements for this study.

The smallest stable flying height is one parameter determines the areal recording density and the efficiency of the NFT. The studies in this chapter concentrate on the flying height profile near the trailing edge which contains the payload—the read and write transducers and the NFT. The simulated minimum flying heights are explained by inspecting the heat transfer from the ABS, the slider’s thermally induced protrusion and temperature profiles, and the air bearing pressure profile.

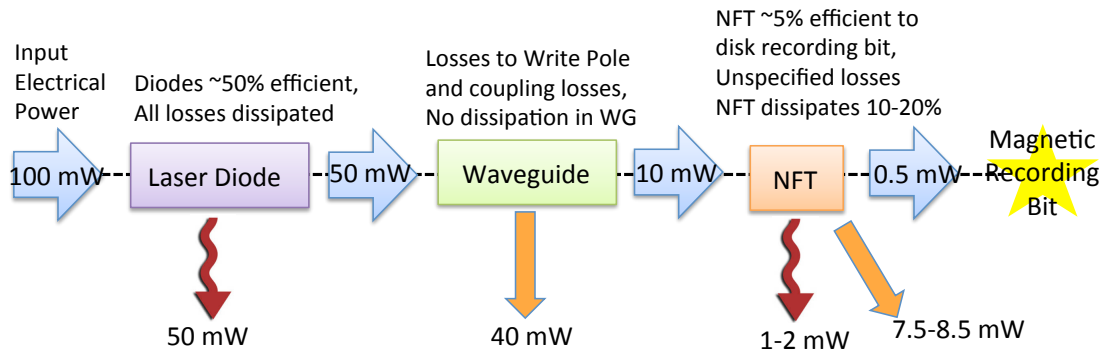


Figure 4.3: The power budget assumed for this study. Power absorbed by a component is assumed to be dissipated as heat.

Boundary Conditions and Simulation Conditions

In the finite element solver presented here, the displacement boundary conditions are applied to the slider to approximate the attachment to the suspension system, thereby transmitting the suspension load. The laser diode is attached to the back of the slider, and on the back of the diode (farthest face from the ABS) the displacement is constrained to be fixed in the vertical z direction. The two corners at the leading edge are fixed. This is the 'back fixed' option in the TFC code released by CML. We are not including the suspension in this model because it adds complexity that we deem unnecessary to perform the thermo-mechanical analysis of the HAMR thermal effects on the air bearing.

Convective boundary conditions are defined on each external face of the slider finite element model. At a rotational speed of 5400 RPM, boundary layer theory predicts the convection coefficient on the non-ABS faces of the slider is on the order of $100 \text{ W}/(\text{m}^2\cdot\text{K})$ [63]. We use a higher convective heat transfer coefficient of $2000 \text{ W}/(\text{m}^2\cdot\text{K})$ on the top of the slider to approximate the heat-carrying capacity of the metal suspension. On the air bearing surface, we use the film coefficient derived from slip theory (Equation 3.11).

Other features of CMLAir are included in the following simulation studies. Intermolecular forces are modeled using the Lennard-Jones potential [64]. At spacings less than 3 nm, the molecules in the disk and slider are close enough to influence each other without contact that may lead to flying instabilities [65]. Intermittent contact is inevitable in a HDD with a disk that will have some amount of roughness. CMLAir treats intermittent contact between the slider and disk in a statistical manner by adding a contact pressure to the force balance [46]. The simulations occur at a disk radial position of 22.215 mm with a skew angle of 0.953 degrees. The disk is spinning at 5400 RPM. The 2.5 g suspension load is applied at the slider's geometric center (no offset). The suspension has a preloaded $0.74\text{-}\mu\text{Nm}$ static pitch torque and $0\text{-}\mu\text{Nm}$ static roll torque.

4.3 HAMR Slider Component Effects on Flying Height

In the process of developing our HAMR slider, we added components one-by-one and tested the impact of the additional components on the predictions of the iterative static solver. The components were added in the following order: TFC heater, NFT, waveguide, and laser diode. Figure 4.4 presents the minimum flying heights at various heater powers for four different sliders with varying amount of laser delivery system components.

The minimum flying height is determined by slider type. The heater-only slider corresponds to a conventional TFC slider currently used in HDD products and has the highest flying height at all heater power levels. The presence of the heat-generating NFT results in lower flying heights. The slider with the lowest flying height is the slider with the heater and NFT. There is not much difference in the minimum flying heights between the final two sliders that only differ by the presence of the laser diode on the backside of the slider.

The minimum flying heights of the three sliders containing a NFT converge around 25 mW when the flying height drops below 2 nm. Next we analyze the centerline profiles of various quantities for a heater power level of 27 mW in order to explain the minimum flying height differences for the slider types shown in Figure 4.4.

The inclusion of HAMR laser delivery system components affects the heat transfer from the slider body, resulting in different ABS temperatures and thermal protrusion profiles that are the reason for the differences in the minimum flying heights predicted by CMLAir-HAMR. The ABS temperatures and protrusion profiles determined by the finite element solver are plotted in Figure 4.5. All slider types have a similar ABS temperature profile away from the NFT region. The TFC slider (heater-only) has a low temperature, around 40°C , in the trailing edge region. The localized sharp temperature spike at the NFT location is due to the insulating feature of the surrounding alumina that keeps much of the dissipated heat at the NFT. For sliders containing a waveguide adjacent to the back of the NFT, the temperature at the NFT is approximately 70°C lower than the slider without the waveguide. This is due to relatively high thermal conductivity of the waveguide; with $k = 57.5 \text{ W}/(\text{m}\cdot\text{K})$, the Ta_2O_5 waveguide conducts heat generated by the NFT away from the ABS more efficiently than the electrically insulating alumina with $k = 1.3 \text{ W}/(\text{m}\cdot\text{K})$). The gold NFT has a thermal expansion coefficient roughly twice that of alumina and three times that of the

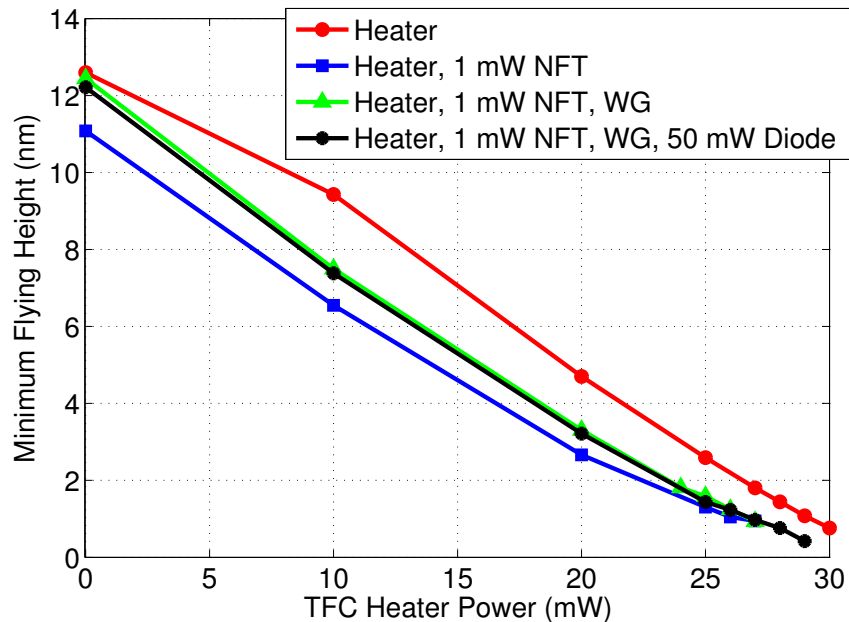
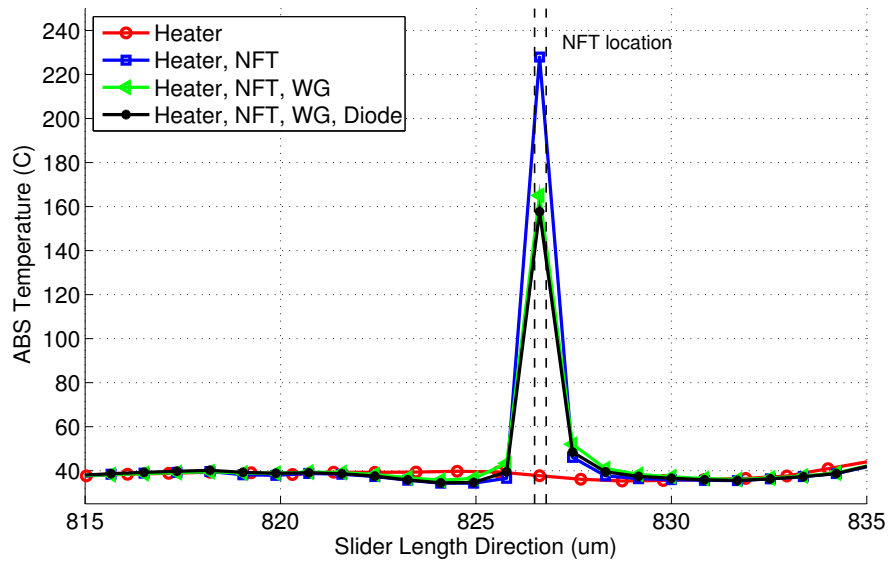
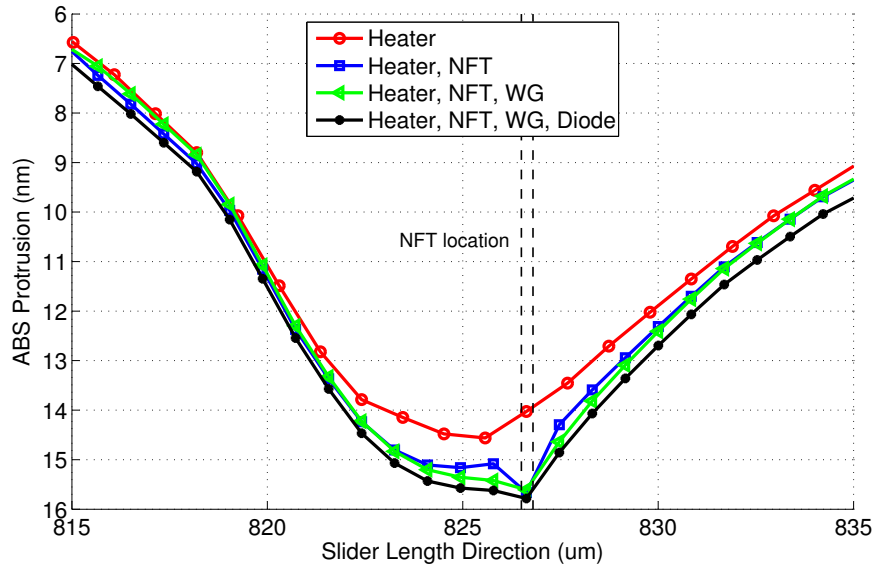


Figure 4.4: Slider Component Study: Minimum flying height for different slider types. If present, the NFT heat generation rate is 1 mW, and the laser diode dissipates 50 mW. WG indicates the presence of the waveguide.



(a) ABS temperature

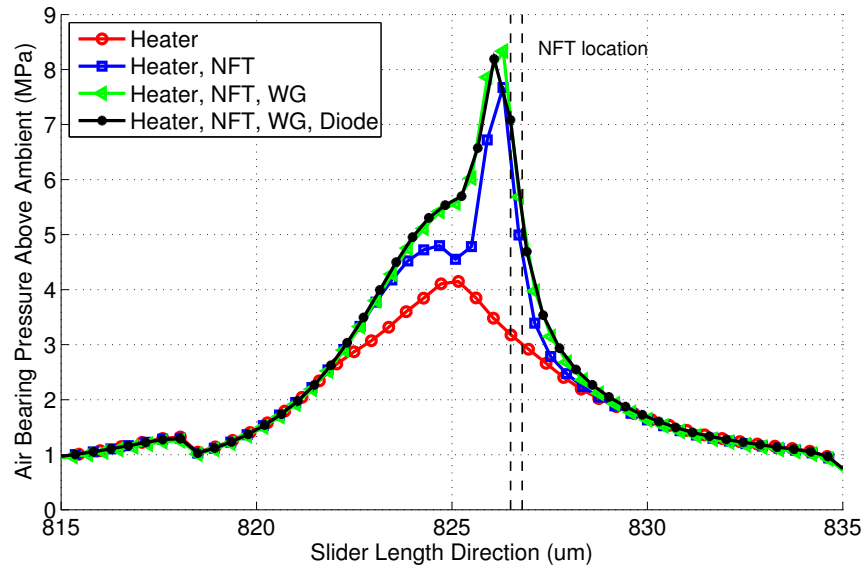


(b) ABS protrusion

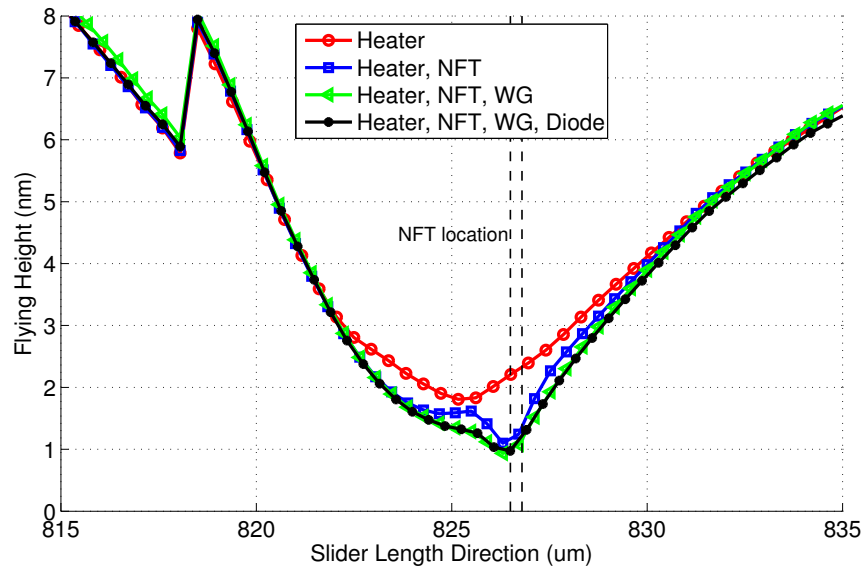
Figure 4.5: Slider Component Study: Centerline profiles of ABS temperature and thermal protrusion near the trailing edge, quantities determined in the ANSYS finite element solver. If present, the NFT heat generation rate is 1 mW, and the laser diode dissipates 50 mW.

waveguide in addition to achieving the highest temperature because it is a heat source. So the NFT protrudes from the surrounding material, creating a relatively sharp protrusion point. The large temperature spike for the heater-NFT-only slider results in the sharpest protrusion profile at the NFT location. The presence of the 50-mW dissipating diode does not significantly affect the temperature profile or protrusion profile. The diode's minor effect is to slightly increase the amount of thermal protrusion compared with the slider containing the NFT and waveguide.

The resulting pressure and flying height profiles are plotted in Figure 4.6 and the heat transfer coefficient at the ABS determined from these air bearing solution profiles is plotted in Figure 4.7. For sliders containing a NFT, the peak pressure location is on the leading edge side of the peak protrusion at the NFT. This is due to the build up of air molecules in front of the relatively sharp NFT protrusion as the spinning disk drags the molecules in Couette flow. For the TFC slider (heater-only), the smooth thermal bulge allows for a gradual pressure increase to a peak pressure that is located at approximately the peak protrusion location. The pressure and flying height profiles of the two most complicated sliders are very close; the presence of the laser diode does not greatly affect the air bearing solution for our simple HAMR slider. The sharp change in flying height at 818 μm is due to the presence of a rail or sharp change in etch depth from 0 nm to 2.54 nm (see Figure 4.2). The heat transfer coefficient profile closely matches the shape of the pressure profile.



(a) Air bearing pressure



(b) Flying height

Figure 4.6: Slider Component Study: Centerline profiles for air bearing pressure and flying height near the trailing edge, quantities determined by the air bearing solver CMLAir-HAMR. If present, the NFT heat generation rate is 1 mW, and the laser diode dissipates 50 mW.

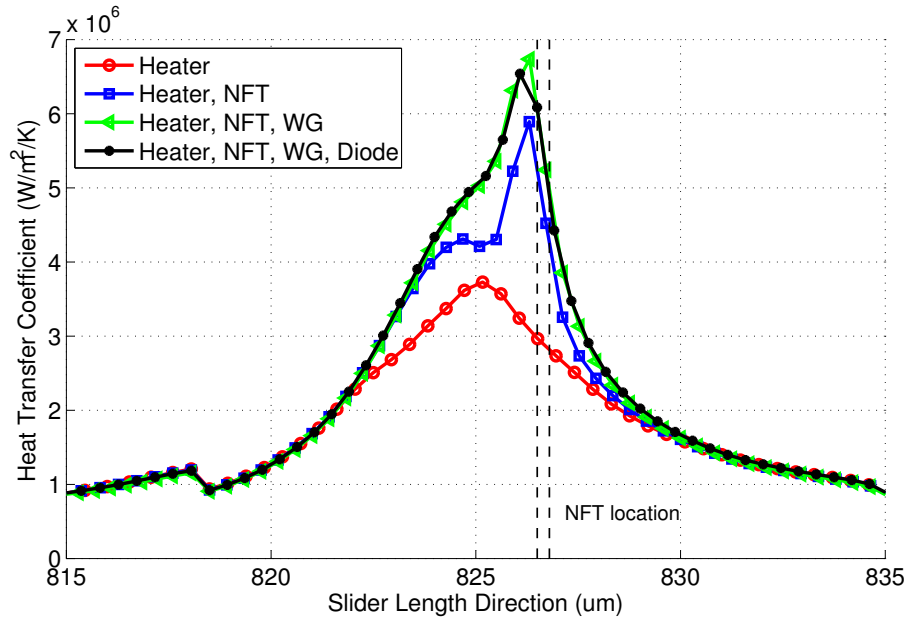


Figure 4.7: Slider Component Study: ABS heat transfer coefficient H_{film} centerline profile near the trailing edge. H_{film} is calculated from the air bearing and pressure profiles (Figure 4.10) and used as the heat transfer boundary condition at the ABS in the finite element solver. If present, the NFT heat generation rate is 1 mW, and the laser diode dissipates 50 mW.

NFT Heat Dissipation Study

Next we investigate how the HDI changes with the rate of NFT heat dissipation. The minimum flying heights for different heater powers are plotted in Figure 4.8. The 2-mW NFT heat dissipation rate results in a minimum flying height roughly 2 nm lower for 0-mW heater power and roughly 1 nm lower at 24-mW heater power with the discrepancy between the two cases gradually decreasing with increasing heater power.

The amount of NFT heat dissipation influences the maximum temperature and amount of thermal protrusion at the ABS as shown in Figure 4.9. The temperature profiles around the NFT are closely clustered according to the NFT heat dissipation rate. The peak ABS temperature roughly doubles as a result of doubling the NFT heat dissipation rate. The higher NFT heat dissipation creates a very sharp protrusion point at the NFT location that is approximately 1.5–2 nm greater at the peak protrusion. The protrusion profiles differ significantly only in a 10–20- μm diameter region centered around the NFT.

The effects of the NFT heat dissipation rate on air bearing pressure and flying height are shown in Figure 4.10. The discrepancy in air bearing peak pressure between the 1-mW and 2-mW NFT heat dissipation rate cases increases with increasing heater power. The difference in minimum flying height at the NFT location closely matches the difference in

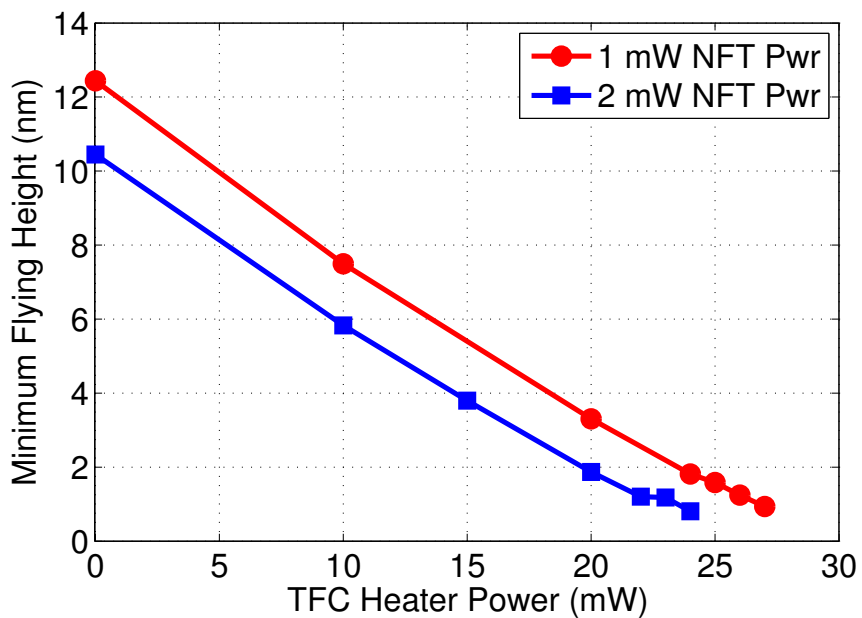
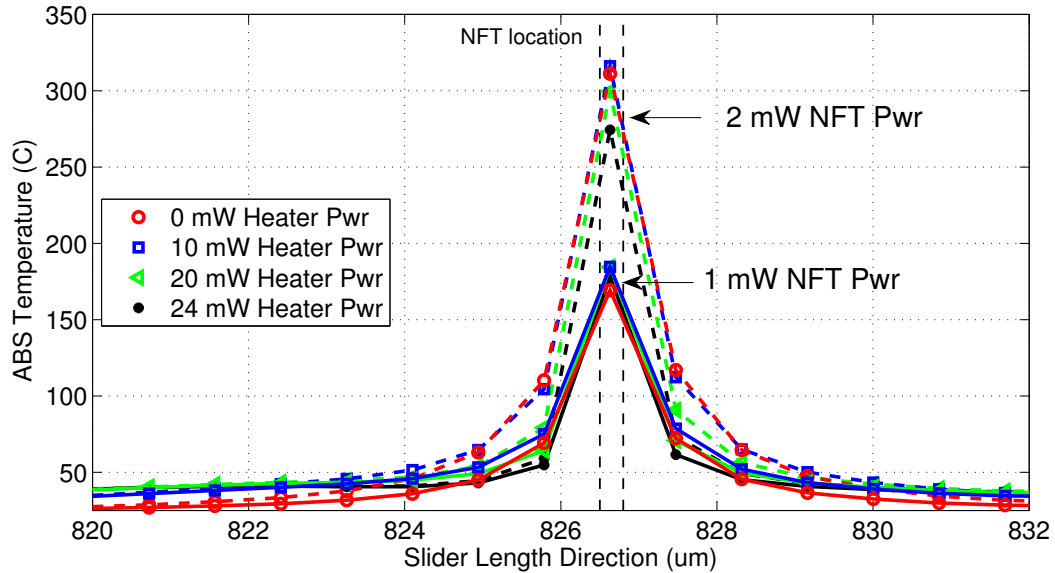
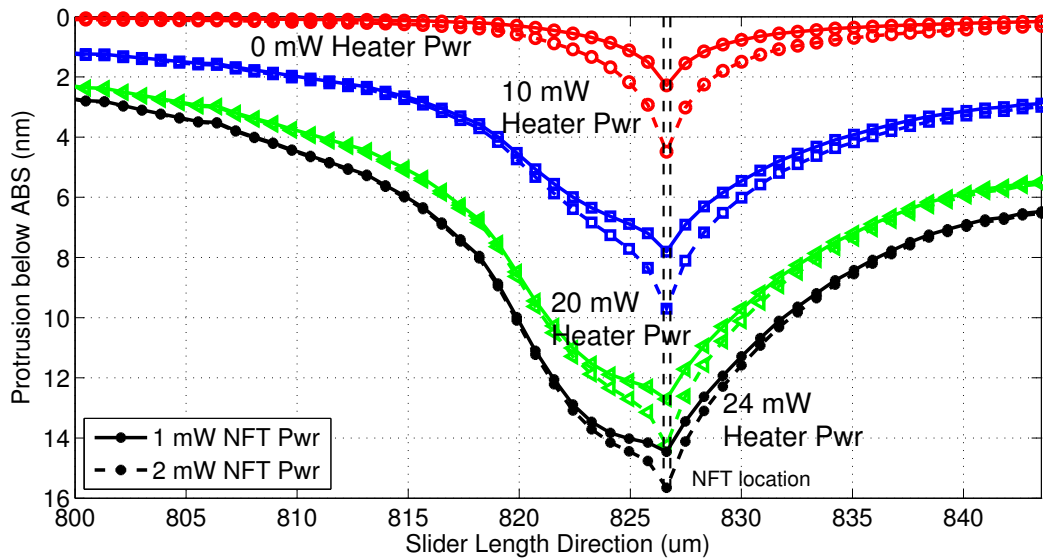


Figure 4.8: NFT Heat Dissipation Study: Minimum flying height for cases of 1-mW and 2-mW heat dissipation rate in the NFT.

peak protrusion. The heat transfer coefficient jumps dramatically around 1-nm flying height, following the jump in the pressure (Figure 4.11).

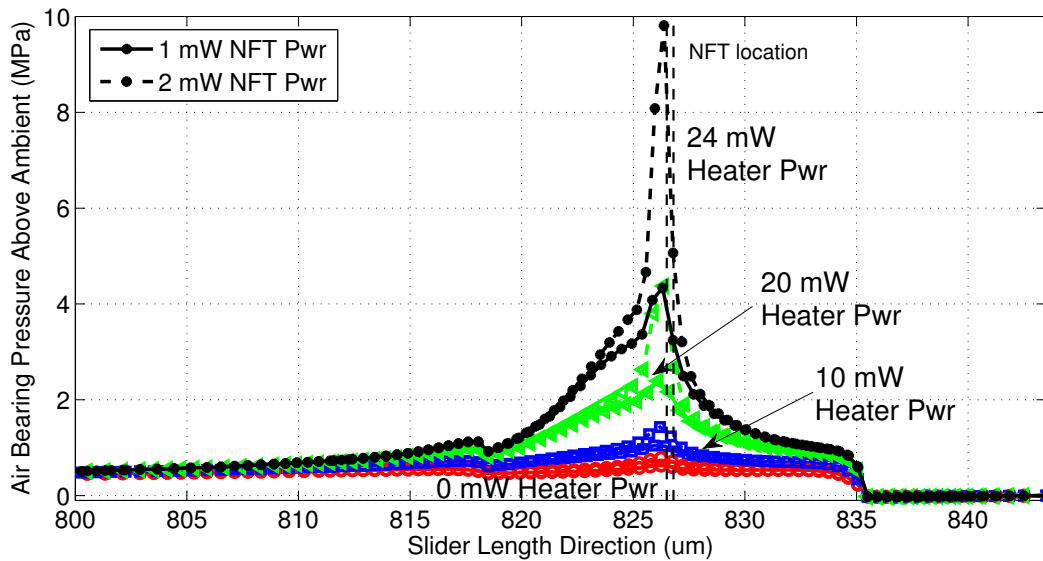


(a) ABS temperature

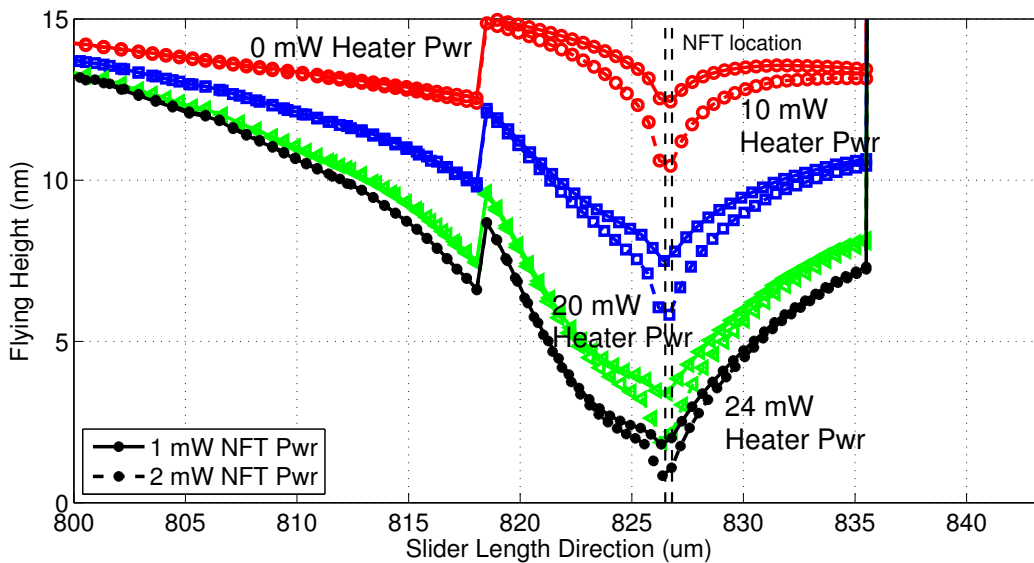


(b) ABS protrusion

Figure 4.9: NFT Heat Dissipation Study: Centerline profiles of ABS temperature and thermal protrusion near the trailing edge, quantities determined in the ANSYS finite element solver. Solid lines correspond to the 1-mW NFT heat dissipation rate and the dashed lines correspond to 2-mW NFT heat dissipation rate.



(a) Air bearing pressure



(b) Flying height

Figure 4.10: NFT Heat Dissipation Study: Centerline profiles for air bearing pressure and flying height near the trailing edge, quantities determined by the air bearing solver CMLAir-HAMR. Solid lines correspond to the 1-mW NFT heat dissipation rate and the dashed lines correspond to 2-mW NFT heat dissipation rate.

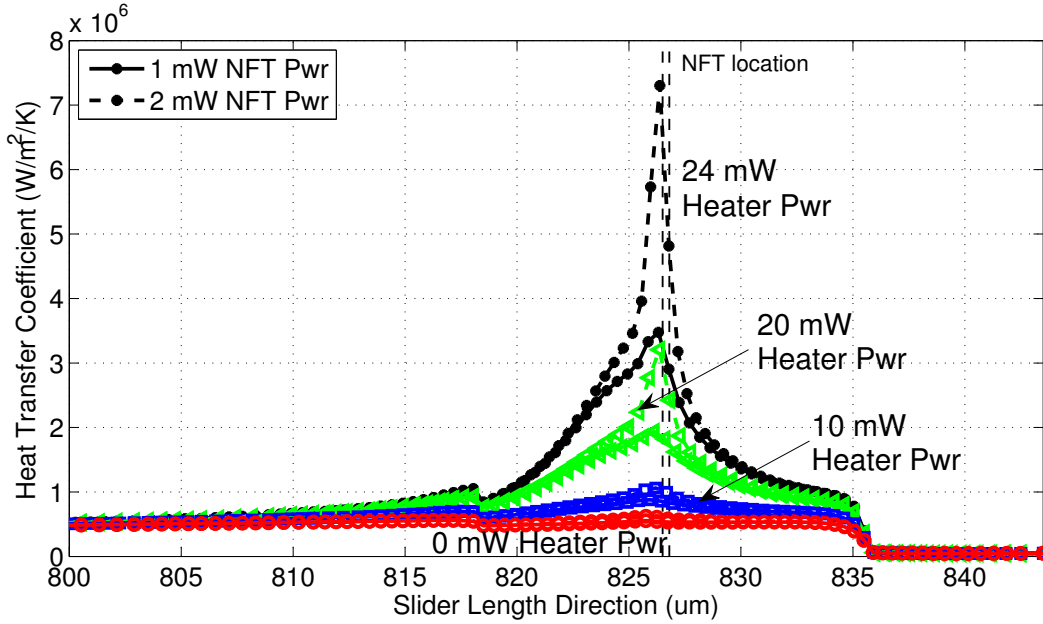


Figure 4.11: NFT Heat Dissipation Study: ABS heat transfer coefficient H_{film} centerline profile near the trailing edge. H_{film} is calculated from the air bearing and pressure profiles (Figure 4.10) and used as the heat transfer boundary condition at the ABS in the finite element solver. Solid lines correspond to the 1-mW NFT heat dissipation rate and the dashed lines correspond to 2-mW NFT heat dissipation rate.

4.4 Effects of New Additions to the Air Bearing Simulation

In this section, the new features added to develop CMLAir-HAMR are turned ‘on’ and ‘off’ to investigate their effects on the predicted minimum flying height of our simple HAMR slider.

Isothermal vs. Generalized Molecular Gas Lubrication Equation

We first investigate the impact of using Fukui and Kaneko’s general molecular gas lubrication (MGL) equation [38] instead of the isothermal MGL equation for our simple HAMR slider containing a heater, waveguide and NFT. The two versions of the iterative static solver are performed for various heater power levels and 1-mW and 2-mW heat generation rates in the NFT. The difference in the minimum flying height between the two solutions (general MGL/CMLAir-HAMR – isothermal MGL/CMLAir) is plotted in Figure 4.12. The difference in predicted minimum flying height is within the tolerance (stopping criterion) of the iterative static solver for heater power levels less than 25 mW which corresponds to a minimum flying

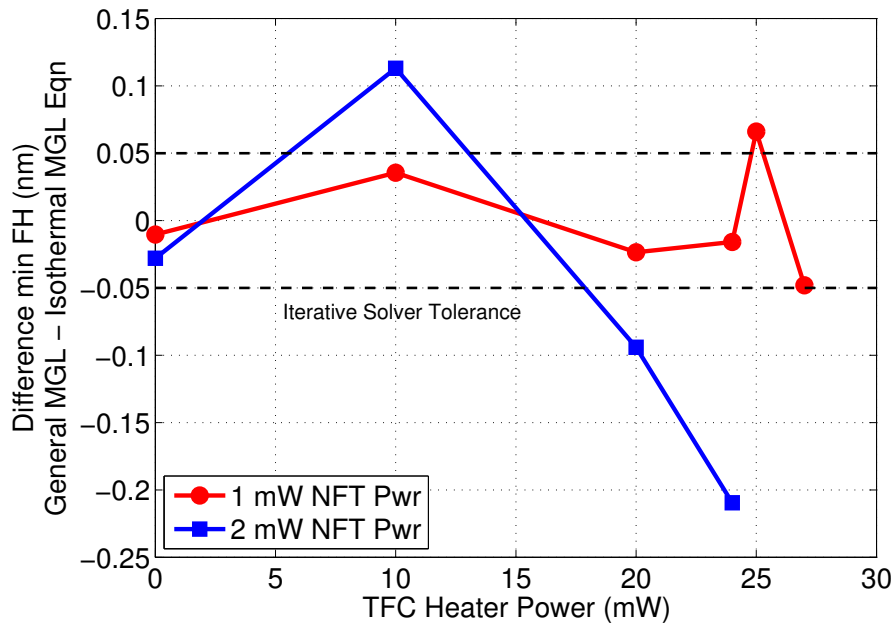


Figure 4.12: Governing Equation Study: Difference in minimum flying height for various heater power levels: general MGL case (CMLAir-HAMR) minus isothermal MGL case (CMLAir).

height greater than 1 nm. At higher heater power levels with lower flying heights, the flying height difference is slightly above but still close to the solver tolerance. The trends are not monotonic; the difference oscillates between positive (CMLAir-HAMR flying higher) and negative (CMLAir flying higher) values.

Thermal Creep Effect

The effect of thermal creep is studied by turning this contribution to the airflow ‘on’ and ‘off’. Two sets of CMLAir-HAMR simulations are conducted at various heater powers and NFT powers of 1 and 2 mW: one case that includes thermal creep and the other case that excludes thermal creep. The difference in the minimum flying height between these two cases is plotted in Figure 4.13. For low heater powers and higher flying heights, the difference in minimum flying height is within the iterative solver tolerance. The discrepancy in flying height increases with increasing heater power, and the case including thermal creep predicts a smaller minimum flying height.

The flying height profiles with and without thermal creep are plotted in Figure 4.14. Noticeable differences in flying height are apparent for cases for which the minimum flying height is 2 nm or less: 1-mW NFT/24-mW Heater, 2-mW NFT/20-mW Heater, and 2-mW NFT/24-mW Heater.

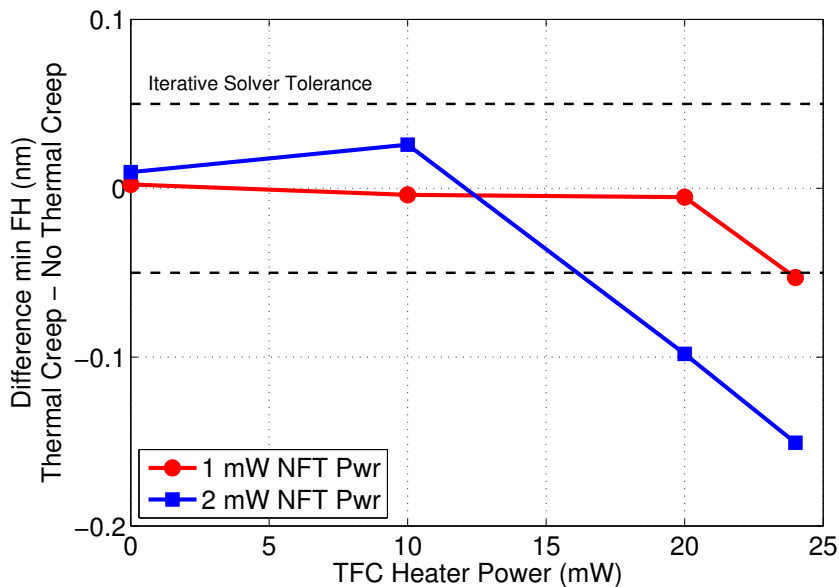


Figure 4.13: Thermal Creep Study: Minimum flying height difference case including thermal creep minus the case without thermal creep

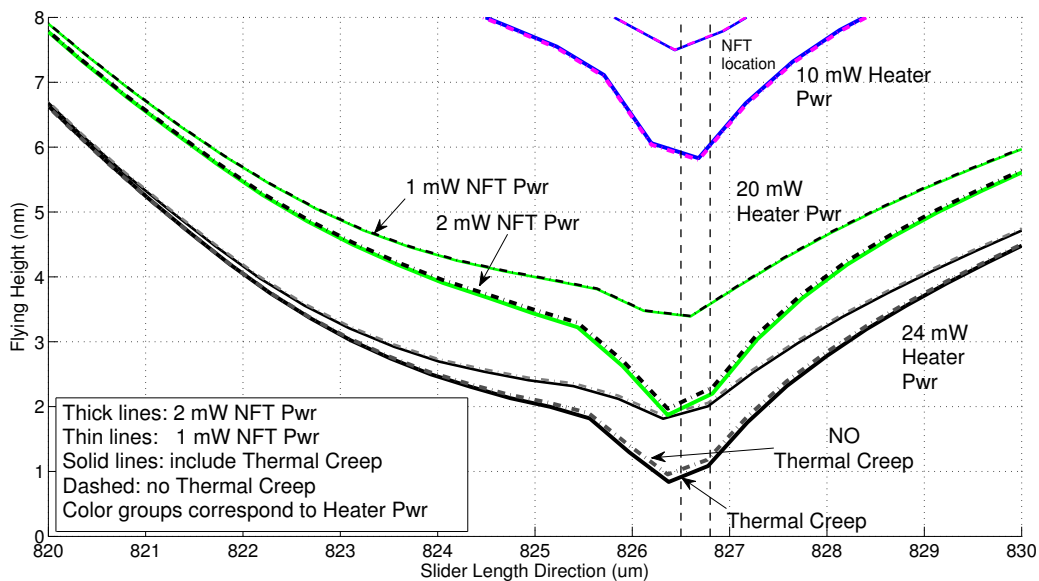
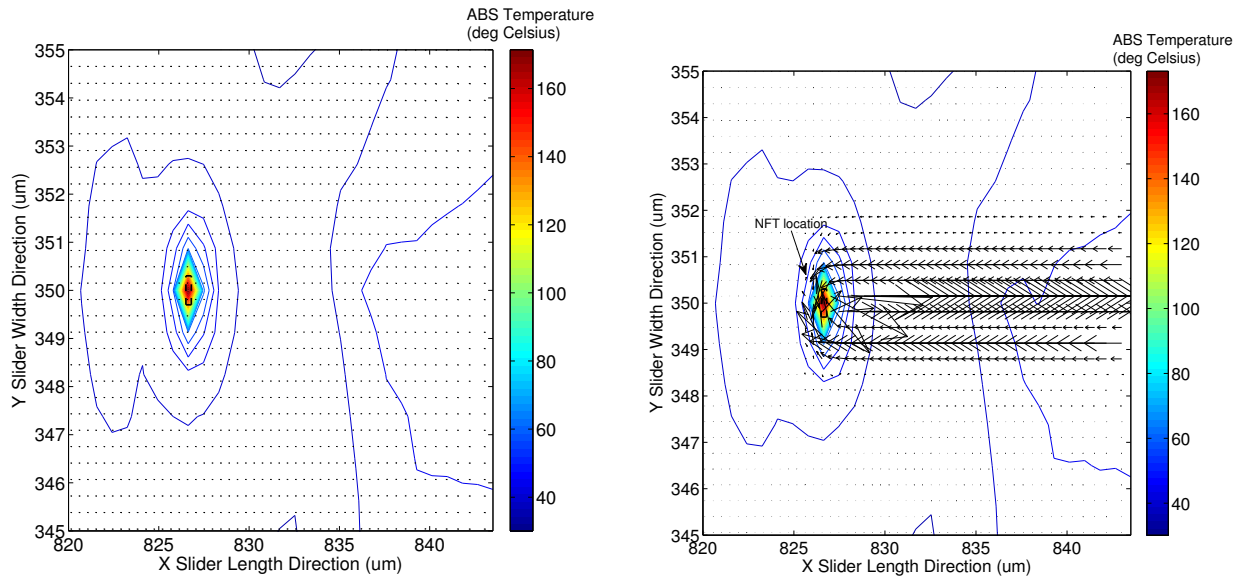


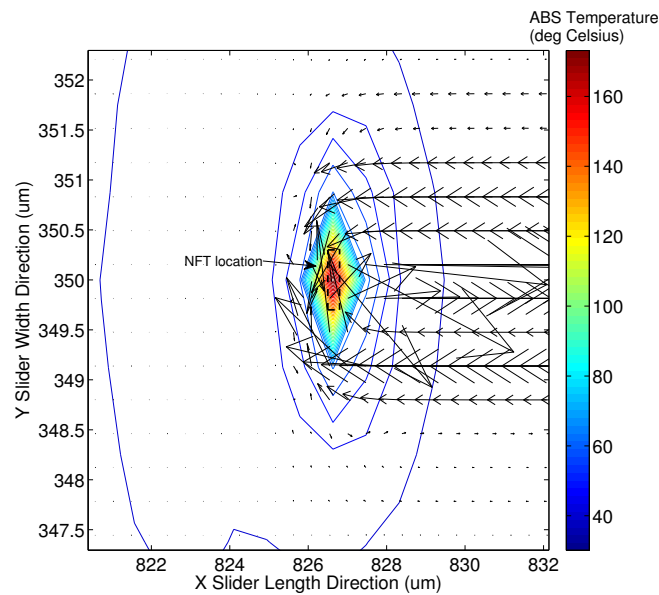
Figure 4.14: Thermal Creep Study: Flying height profiles near the NFT for cases including thermal creep and excluding thermal creep in CMLAir-HAMR. Noticeable differences in flying height are apparent for cases for which the minimum flying height is 2 nm or less.

Thermal creep affects the air flow by driving fluid from cold to hot regions. So under a HAMR slider, thermal creep drives air towards the hot NFT region. Figure 4.15 presents mass flow vector fields that indicate the strength and direction of the air flow. The case including thermal creep shows enhanced air flow in the region of the NFT. Directly over the NFT the flow field is toward the trailing edge. To either side of the NFT, the air flow is in the direction of the leading edge. This leads to reduced heat transfer in the NFT region and a hotter slider, predicted to be about 10°C hotter at the NFT location compared to the case excluding thermal creep. Thus there is more thermal protrusion and therefore lower flying height when thermal creep is included. As indicated in Figure 4.15, the air bearing solver grid is too coarse around the NFT. A multi-scale air bearing simulator would better capture the phenomena around the NFT, and this may be a fruitful topic for further study of the thermal creep effect. Another issue may be that the linearized Boltzmann equation does not apply in a region with such a high temperature gradient.



(a) Thermal creep excluded

(b) Thermal creep included



(c) Thermal creep included, Zoom to NFT location

Figure 4.15: Thermal Creep Study: Mass flow rate vectors (kg/s) with ABS temperature profile contour lines and the location of the NFT marked. The NFT power dissipation is 1 mW, and the heater power is 24 mW. The length of the vectors indicate the magnitude of the mass flow rate vector.

Effects of ABS Heat Transfer Model and Mean Free Path Temperature Dependence

Figure 4.16 shows the effects of the choice of ABS heat transfer model (λ or λ_m) and including the temperature dependence on the mean free path ($\lambda = \lambda_0 \bar{T}/P$ instead of $\lambda = \lambda_0/P$) on the flying height centerline profile near the trailing edge. The maximum temperature at the NFT location is approximately 200°C for these simulations.

The flying height profile is slightly lower for heat transfer model 1 (λ) compared to heat transfer model 2 (λ_m). In the lowest section pictured in Figure 4.16 at approximately 2-nm flying height, the flying height difference is around 0.1–0.15 nm. The physical interpretation used to modify the mean free path is that molecules close enough to the bounding surfaces hit the wall before they collide with other gas molecules; therefore, the average mean free path is shorter in the restricted space between the two bounding surfaces [55]. Recalling the hard sphere gas mean free path definition (Equation 3.4), we see that the mean free path is inversely proportional to the gas molecule number density; a shorter mean free path indicates a higher air molecule density, so there are more air molecules to act as heat carriers between the slider and disk. Thus a shorter air mean free path leads to a larger H_{film} . At the NFT location, the heat transfer coefficient is 0.35 MW/(m²·K) higher or 10% higher

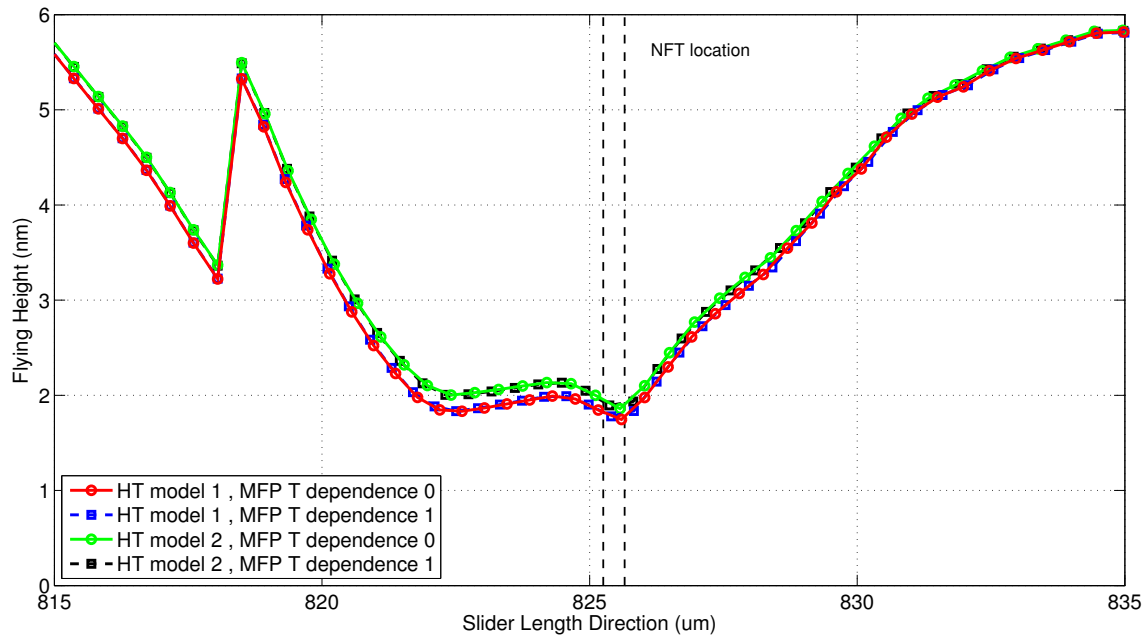


Figure 4.16: Flying height along the centerline near the trailing edge for cases using heat transfer model 1 (unmodified mean free path λ [53]) or heat transfer model 2 (modified mean free path λ_m [55]) and cases including and not including the temperature dependence on air mean free path.

using the heat transfer model 2. This higher rate of cooling at the ABS results in a cooler ABS temperature ($\sim 5^\circ\text{C}$) and less thermal protrusion (~ 0.5 nm), leading to a lower air bearing peak pressure ($\sim 0.2\text{--}0.3$ MPa) and smaller flying heights in the ABS region closest to the disk.

The flying height does not appreciably change when we include the temperature dependence on mean free path. For a given heat transfer model, the flying profile is practically the same with and without the temperature dependence of mean free path. Mean free path determines the heat transfer at the ABS (Equation 3.11) and the local Poiseuille and thermal creep flow rate coefficients (Equation 3.11). H_{film} is slightly lower when the temperature dependence of mean free path is included, but the minor decrease in cooling leads to less than 0.01 nm more thermal protrusion of the ABS. This slight increase in thermal protrusion has no noticeable effect on the air bearing pressure profile or flying height. The non-dimensional flow rate coefficients Q_P and Q_T do not vary significantly over a wide range of Knudsen numbers: Q_P is within the range 2 – 4 for $\text{Kn} = 10^{-3} - 10^7$ and Q_T is within 0 – 1.8 for $\text{Kn} = 10^{-4} - 10^7$ [66]. With the temperature over most of the ABS only tens of degrees Celsius above ambient and only a small region around the NFT that is a couple hundred degrees above ambient, the overall increase in air bearing temperature and therefore mean free path is less than a factor of 5. So the changes to Q_P and Q_T are negligible.

4.5 Discussion

In this chapter, we simulated stable flying conditions down to about 1-nm minimum flying height and showed that interesting phenomena such as thermal creep and high conductive heat fluxes from the ABS occur in the range of 1–2-nm minimum flying height. Here, variations in minimum flying height of even 0.1 nm are significant, accounting for 5–10% of the flying height budget.

Some of our simulation results are comparable to the thermo-mechanical modeling of an integrated HAMR slider performed at the Digital Storage Institute [16]. We use the same heat transfer model from the ABS and similar convective boundary condition to non-ABS slider faces. The DSI slider finite element model is similar to ours except for their addition of two components we excluded (a prism coupling the laser from the diode to the waveguide and a suspension) and a defined boundary thermal resistance between the diode and slider representing a soldering joint. However, in [16] the air bearing problem is not solved; rather just the finite element solver is used with a prescribed pressure profile and flying attitude. In reality, the air bearing pressure increases with decreasing minimum flying height, as shown in the studies of this section (see Figures 4.6a and 4.10a), and that increases the conductive heat transfer from the ABS (see Figures 4.7 and 4.11). In [16], one figure shows only a 0.5°C decrease in NFT temperature (gold, 1-mW heat dissipation rate) for a decrease in minimum flying height from 8 nm to 4 nm (the smallest flying height used). Our simulations predicted similar results for a comparable system: for the 1-mW NFT case, we predict a NFT temperature drop of 0.2°C for a decrease in minimum flying height from 7.5 nm (10-mW

heater power) to 3.3 nm (30-mW heater power). However the constant pressure assumed by Xu et al. [16] is not expected to give accurate NFT temperature results if the flying height is decreased below 4 nm. Xu et al. [16] predict an NFT temperature of 250°C for 1-mW NFT power and 475°C for 2-mW NFT power with a minimum flying height of 2 nm; we predict lower NFT temperatures for similar conditions: 184.5°C NFT temperature for 1-mW NFT power at 3.3-nm minimum flying height and 312.3°C for 2-mW NFT power at 3.8-nm minimum flying height. Our lower predicted temperature is due to our choice of waveguide material; we use a higher thermal conductivity waveguide material that can more easily conduct heat away from the NFT and cool it. They observed 2 nm of protrusion at the NFT location due to its higher temperature and larger coefficient of thermal expansion. We show slightly less NFT protrusion compared to the surrounding material, closer to 0.6 nm under similar simulation conditions, because of our choice of waveguide material that has a similar coefficient of thermal expansion as the NFT and also because of our lower NFT temperature.

In an earlier publication, we used CMLAir-HAMR for different prescribed ABS temperature profiles with the same protrusion profile [67]. For those ABS large thermal spots, thermal creep did not change the static flying attitudes. The full width at half maximum Gaussian temperature profiles were relatively large: 50- μm or 170- μm FWHM and the temperature rise was 100–300°C. For the studies in [67] the minimum flying height ranged from 2.2–3.5 nm, just above the threshold found in this chapter for thermal creep to be slightly important. The difference in minimum flying height between cases including and not including thermal creep in [67] was on the order of 10^{-3} nm because the ABS temperature gradient was relatively large and the minimum flying height was relatively high. In this chapter, a thermal spot at the NFT roughly 3 μm wide resulted in 0.2 nm lower flying height when the minimum flying height was just under 1 nm. We see minimum flying height differences due to thermal creep that are larger than the solver tolerance only when the minimum flying height is less than 2 nm.

Thermal creep could be an important factor to investigate further. The grid used in this investigation is too coarse around the small NFT, so only a few nodes are present in the region to predict the behavior. Due to the discrepancy in length scales, another air bearing problem should be solved in the region near the NFT with the larger air bearing problem used to find the pressure boundary conditions. An iterative loop between the large and small air bearing problems could be nested within the larger iterative static solver to more accurately predict the behavior of the HAMR slider.

The heat transfer coefficient is greatest at the minimum flying height location where the pressure is maximum. For an actual HAMR slider, this location will likely correspond to the NFT. Challener et al. [13] noted that the HAMR sliders did not last more than a few write cycles. Some researchers have proposed that the NFT is being destroyed because the level of laser irradiation experienced by the HAMR slider near-field transducers exceeds the laser-induced damage threshold for thin-film gold [68]. The studies in this chapter predict that the heat transfer coefficient dramatically increases around 1 nm. If a stable 1-nm flying height can be realized, the enhanced cooling of the ABS could be used to control the temperature

rise of the NFT. However, the laser irradiation level needs to be low enough so as to not exceed the damage thresholds.

The ANSYS analysis presented here uses macroscopic field theories in the coupled-field analysis: Maxwell’s equations for the electrical analysis, Fourier’s law for heat condition in the thermal analysis, and linear elasticity for the structural analysis. These theories employ a continuum assumption. For the tiny features of an integrated HAMR slider—the NFT is only 100 nm thick and 300–600 nm in lateral dimensions—continuum theory may not be valid. The HAMR slider heat transfer problem requires a different type of analysis that is not limited by continuum assumptions. The aim of this work is to gain insight into the performance of the air bearing under HAMR conditions. A more accurate finite element heat transfer analysis is left to other researchers. When and if reliable HAMR sliders are built and become available, they would provide a means to experimentally validate any nanoscale thermo-mechanical simulation tools that are developed.

4.6 Conclusion

In this chapter, an iterative static solver based on the general MGL equation is used to determine the equilibrium flying conditions and thermal deformation of a simple HAMR slider design with a complicated ABS rail design. The components that dissipate heat are the TFC heater, NFT, and laser diode. The NFT induces localized protrusion and has the highest temperature. The Ta_2O_5 waveguide dissipates heat away from the NFT and lowers the ABS maximum temperature, leading to a smoother NFT protrusion. The laser diode does not appreciably affect the slider’s air bearing and thermo-mechanical state for this particular slider design. The ABS temperature and thermal protrusion are determined by the power dissipated in the NFT. The thermal deformation of the slider is an important factor that significantly influences the flying height, so an accurate electro-thermo-mechanical model is needed.

Several air bearing model options were tested. For minimum flying heights below 2 nm and confined thermal spots at the NFT, thermal creep adds to the air flow so as to decrease the minimum flying height up to 0.15 nm for the conditions simulated here. The choice of heat transfer model (λ or λ_m) could change the flying height in the trailing edge location by 0.1–0.15 nm for a minimum flying height around 2 nm. The difference in the minimum flying height between the solutions using the general MGL or isothermal MGL are significant only for relatively high temperature, low flying height conditions. Including the temperature dependence on the mean free path did not significantly change the predicted flying attitude.

Chapter 5

Lubricant Model and Its Numerical Solution

5.1 Lubricant Property Models

Intermolecular interactions between various components of the thin-film system dictate the movement of the lubricant that covers the disk: lubricant-lubricant molecule interactions, lubricant-carbon overcoat interactions, and the presence of two interfaces in close proximity (air-lubricant and lubricant-carbon overcoat). In order to model the lubricant from a continuum point of view, we endow the lubricant with various macroscopic properties that capture the long-range effects of the intermolecular interactions on lubricant flow and evaporation. These properties are surface tension, disjoining pressure, viscosity, and vapor pressure. Vapor pressure determines the evaporation rate of the lubricant. Surface tension and disjoining pressure, in effect, apply forces to the lubricant-air interface and determine the lubricant pressure. In addition, we make an assumption about the density of the 1–2-nm lubricant film covering the disk.

Surface Tension

When a molecule is brought to the interface between a liquid and a gas, the molecule experiences intermolecular attractions from one side only. The unbalanced intermolecular forces near an interface means there is a thermodynamic surface energy γ_{LV} per unit area of liquid-vapor interface; in order to bring more molecules to the surface and increase the area of the interface, an additional energy γ_{LV} per unit of added area needs to be applied to the system [69, 70]. For liquids, surface energy can be interpreted as a force per unit length that acts tangent to the interface, and this force is commonly called surface tension: $\gamma = \gamma_{LV}$.

The resultant force of surface tension can be decomposed into two parts: a component tangent to the interface that is due to variations in surface tension (Maragoni stress) and a component acting normal to the interface due to surface curvature (Laplace pressure or capillary pressure) [71]. In this study the variation in surface tension is due to a temperature

gradient, and the resulting Maragoni stress is also called thermocapillary stress. Thus surface tension contributes to the force balance at the lubricant-air interface via its resultant applied pressure and shear stress:

$$\begin{aligned} p_{ext} \mathbf{n} \Big|_{\gamma} &= (-\gamma \nabla \cdot \mathbf{n}) \mathbf{n} = (\gamma \nabla^2 h) \mathbf{n} \\ \boldsymbol{\tau}_{ext} \Big|_{\gamma} &= \nabla \gamma - \mathbf{n} (\nabla \gamma \cdot \mathbf{n}) \end{aligned}$$

where \mathbf{n} is the interface unit normal vector and the gradient is a two-dimensional operator: $\nabla(\cdot) = \frac{\partial}{\partial x}(\cdot) \mathbf{e}_1 + \frac{\partial}{\partial y}(\cdot) \mathbf{e}_2$. For quasi-parallel films ($|\nabla h| \ll 1$), $\mathbf{n} \approx \mathbf{e}_3$, so $\nabla \gamma \cdot \mathbf{n} \approx 0$. Therefore the external forces on the lubricant-air interface due to surface tension are

$$p_{ext} \mathbf{n} \Big|_{\gamma} = (\gamma \nabla^2 h) \mathbf{e}_3 \quad (5.1)$$

$$\boldsymbol{\tau}_{ext} \Big|_{\gamma} = \frac{\partial \gamma}{\partial x} \mathbf{e}_1 + \frac{\partial \gamma}{\partial y} \mathbf{e}_2 \quad (5.2)$$

The surface tension of most liquids decreases with increasing temperature until it reaches a value of zero at the critical temperature. The surface tension of a non-polar PFPE lubricant was measured in the limited temperature range of 10-180°C and found to be linear [72]. We assume that functional PFPE lubricants such as Zdol have a similar slope, and in our model we use the slope $\frac{d\gamma}{dT} = -0.06 \text{ mN}/(\text{m}^\circ\text{C})$. With this assumed dependence on temperature, the external shear stress due to surface tension (thermocapillary shear stress) becomes

$$\boldsymbol{\tau}_{ext} \Big|_{\gamma} = \frac{d\gamma}{dT} \frac{\partial T}{\partial x} \mathbf{e}_1 + \frac{d\gamma}{dT} \frac{\partial T}{\partial y} \mathbf{e}_2 \quad (5.3)$$

where T is the local lubricant temperature. For the simulations in this paper, $T(x, y, t)$ is prescribed so the temperature gradient is a known quantity.

Disjoining Pressure

For sufficiently thin films, the lubricant molecules at the lubricant-air interface experience intermolecular forces from liquid molecules in the film and molecules in the solid substrate. In effect, these intermolecular forces have a finite range r , as schematically illustrated in Figure 5.1. First introduced by Derjaguin, disjoining pressure is defined as the difference between the hydrostatic pressure p in the thin liquid film and the pressure of the bulk phase p_∞ under the same thermodynamic conditions (equal temperature and chemical potential) [73]:

$$\Pi(h) = p - p_\infty$$

This additional or supplementary pressure acting on a interfacial surface element produces an extra force that augments the classical equations of hydrostatics. This new force in thin-film systems is a function of film thickness only, and it is proportional to surface area. It is

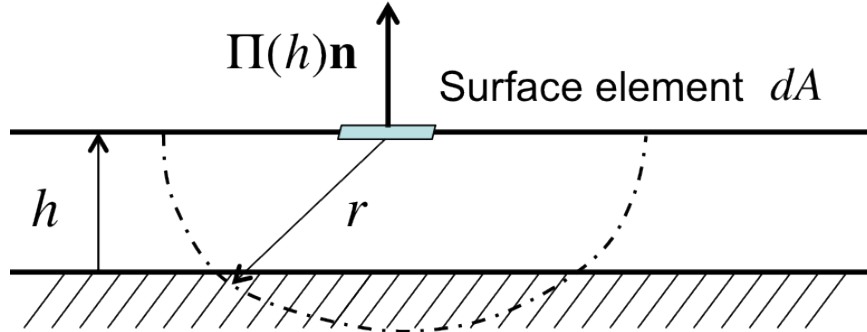


Figure 5.1: Disjoining pressure is the resultant force of intermolecular interactions in the solid-liquid-vapor system within a range of influence r on the interfacial surface element dA .

the resultant force of all intermolecular interactions within the solid-liquid-vapor system on the interfacial surface element dA . Disjoining pressure can be positive (solid substrate repels interface) or negative (solid substrate attracts interface). Thus the contribution of disjoining pressure acting on interfacial elements is

$$p_{ext}\mathbf{n}\Big|_{\Pi} = \Pi(h)\mathbf{e}_3 \quad (5.4)$$

The challenge for accurately predicting lubricant behavior in hard disk drives has been to determine an appropriate model for the disjoining pressure of the particular lubricant-disk system of interest. We consider two contributions to disjoining pressure and use the terminology common in hard drive lubricant literature [74]: (1) the *dispersive component* due to van der Waals forces with $1/h^3$ dependence and (2) the oscillating *polar component* that could be due to structural effects or non van der Waals interactions introduced by the functional end-groups. Previous simulations for lubricants covering the disk under HAMR conditions have only considered the dispersive component [72, 75–77].

The sessile drop method of determining the disjoining pressure of hard drive lubricants from experimental surface energy (contact angle) data has been widely used. However, some researchers have questioned the assumptions made in this method and caution that while such experiments and analysis are useful probes for determining lubricant-substrate dynamics, the values determined for disjoining pressure should not be taken as a true experimental measurement [74, 78]. In the absence of an accurate method for measuring disjoining pressure, we use the mathematical model for PFPE Zdol from Karis and Tyndall [79] derived using contact angle measurements from their earlier publications [80–82]. The authors assumed a $1/h^2$ form of the dispersive component of surface free energy consistent with the $1/h^3$ form for dispersive disjoining pressure and determined the coefficients by a regression fit to dispersive surface energy data: $\gamma^d = c_0 + c_1/h^2$. Using the notation from [79], we call γ the surface energy. The oscillating polar component of surface energy is fit to the polynomial expansion $\gamma^p = \sum_{i=0}^n a_i h^i$. The disjoining pressure is the negative derivative of

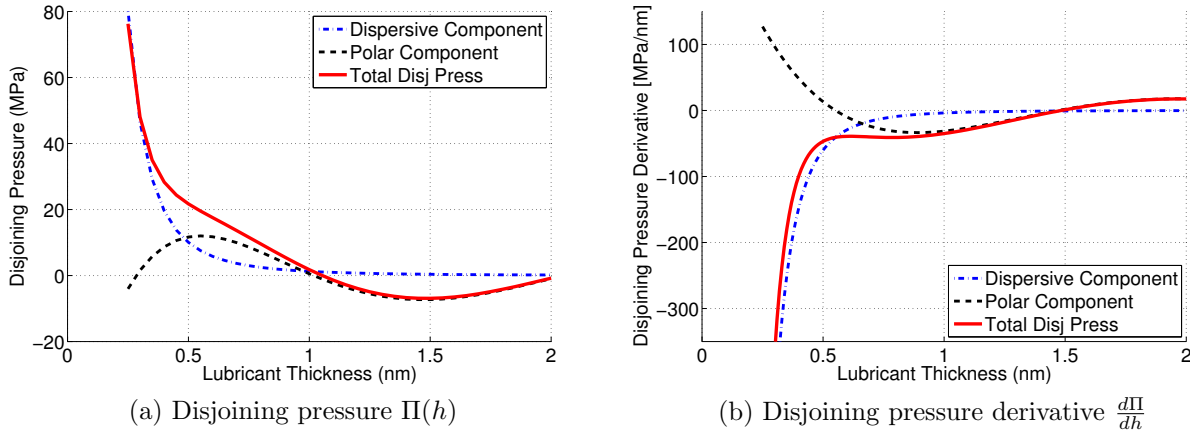


Figure 5.2: Disjoining pressure model reproduced from [79] with permission from Elsevier. This model is derived from experimental free energy measurements (sessile drop method) of unannealed PFPE Zdol 2000 on magnetic disks with a 1.3-nm amorphous hydrogenated carbon overcoat.

the free energy gradient with respect to h :

$$\Pi = -\frac{d\gamma}{dh} = -\frac{d\gamma^d}{dh} - \frac{d\gamma^p}{dh} = \Pi^d + \Pi^p$$

The disjoining pressure and its derivative for Zdol from [79] are plotted against film thickness in Figure 5.2. Note that surface energy measurements can vary significantly with lubricant end-group, molecular weight, and production processes such as annealing [80], so by employing this model, we are confining our simulation results to the lubricant-disk systems used in the experimental data to which the disjoining pressure model was fit (unannealed Zdol 2000 coating a production magnetic disk with a 1.3-nm-thick amorphous hydrogenated carbon overcoat). We are also limiting our simulations to 0.2–2 nm because that is the range of the experimental data on which the disjoining pressure model is based. Other kinds of lubricants may have different intermolecular interactions and therefore they may require a different disjoining pressure model.

Viscosity

An explicit formula for viscosity can be derived by applying the method of absolute reaction rates to pure liquids. In this approach, credited to Eyring [83], viscosity and diffusion in a liquid are viewed as rate processes, similar to chemical kinetics. In Eyring’s model, flow occurs when one molecule squeezes past its neighbors, passing through a ‘flow-activated state’ in which intermolecular potential energies are high due to closer proximity with neighboring

molecules, and drops into a vacant equilibrium position. Eyring reasoned that because some of the same intermolecular bonds are broken in a flow process as in a vaporization process, the activation energies of viscous flow can be estimated from vaporization energies.

Karis [84] applied Eyring’s rate theory to hard disk drive lubricants. The resulting thin-film viscosity model is:

$$\eta = \left(\frac{N_A h_P}{V_l} \right) \exp \left(\frac{\Delta E_{vis} - T \Delta S_{vis}}{RT} \right), \quad (5.5)$$

where N_A is Avogadro’s number, h_P is Plank’s constant, V_l is the molar volume (moles per unit volume) of the lubricant, R is the universal gas constant, and T is the system temperature. ΔE_{vis} and ΔS_{vis} are the flow-activation energy and entropy that depend on film thickness. We use the same reasoning and ΔE_{vis} and ΔS_{vis} values as those found in [84] for Zdol. The viscosity variation with lubricant thickness and temperature is plotted in Figure 5.3.

In contrast to the work we present in this paper, earlier simulations of hard drive lubricants under HAMR conditions have included only the temperature dependence on viscosity [75–77]. This chemical kinetics model for viscosity gives the same trend with temperature but also includes the effects of a thinning film of lubricant flow.

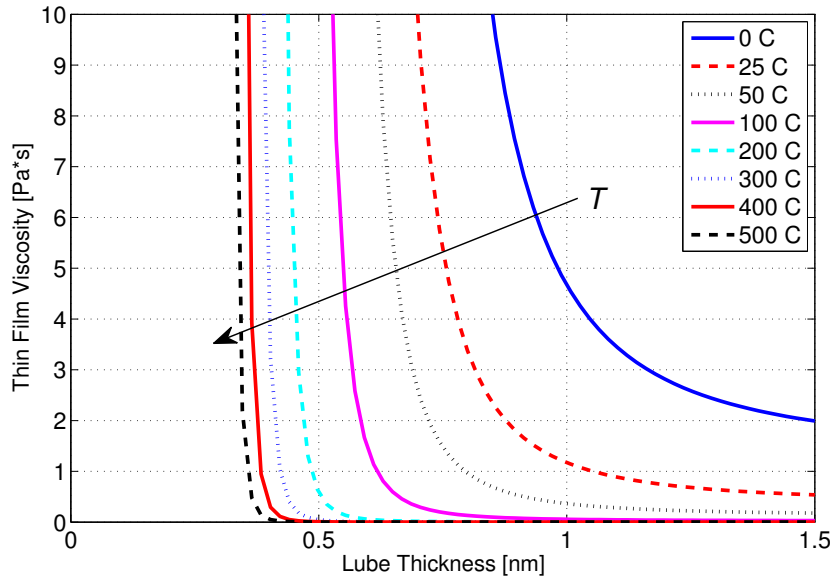


Figure 5.3: Viscosity model for Zdol from [84] based on Eyring’s rate theory [83]. The arrow points in direction of increasing temperature.

Vapor Pressure and Evaporation Rate

Vapor pressure depends on the system temperature and the nature and strength of the intermolecular interactions that need to be overcome for a molecule to escape the condensed state and vaporize. For PFPE lubricants, longer molecular chains (higher molecular weight) mean more interactions to overcome during vaporization; therefore, higher molecular weight lubricants have a lower vapor pressure. We use the method of Karis [20] to calculate the bulk vapor pressure $p_{vap,\infty}(T, M_w)$ of Zdol with the Clapeyron equation and employing the ideal gas law. The linear relationship between vaporization activation energy and molecular weight for Zdol was determined by comparing simulated evaporation data with that measured by isothermal thermogravimetric analysis [25].

Independent of its origin, a pressure difference across an interface causes a change in the equilibrium vapor pressure from the bulk value at a given temperature [85]. The long-range intermolecular interactions between the liquid film molecules and the solid substrate that give rise to disjoining pressure and the curvature of the interface modify the vapor pressure of the thin-film lubricant system by adding to the system's chemical potential. Expressions for the liquid and vapor phase chemical potentials are found by integrating the Gibbs-Duhem equation, and the final result for the equilibrium thin-film vapor pressure for a given system temperature T is determined by equating the liquid and vapor chemical potentials [86]:

$$\frac{p_{vap, film}}{p_{vap, \infty}} = \exp\left(\frac{M_w}{\rho RT} [-\Pi(h) - \gamma \nabla^2 h]\right) \quad (5.6)$$

We assume a simple constitutive model for the rate of evaporation of the lubricant based on kinetic theory. The Hertz-Knudsen-Langmuir model for evaporation/condensation specifies that the evaporation or condensation rate is proportional to the difference between the equilibrium vapor pressure and the current vapor pressure [87]:

$$\dot{m} = \alpha \frac{M_w}{\sqrt{2\pi RT}} (p_{vap} - p_i), \quad (5.7)$$

where \dot{m} is the evaporative mass flux (units mass/time per unit area), M_w is the molecular weight of the liquid molecules (mass per mole), R is the molar universal gas constant, and T is the liquid-vapor system common temperature. α is an evaporation coefficient (sometimes called the accommodation coefficient) that accounts for imperfect evaporation and the shortcomings of collision theory to describe real systems. p_{vap} is the equilibrium vapor pressure and p_i is the current vapor pressure, i.e. the partial pressure of the adjacent vapor in the gas mixture (evaporated liquid vapor plus an inert component). This simple model implies a net evaporation rate as long as the partial pressure of the evaporated substance immediately above the interface is less than the vapor pressure ($p_i < p_{vap}$).

Furthermore, we simplify the evaporation model by making additional assumptions. Recently, researchers have matched this evaporation model to relatively low temperature ($< 240^\circ\text{C}$) experimental data and claimed that the accommodation coefficient is approximately one for $T < 133^\circ\text{C}$ and decreases exponentially with increasing temperature up to

the limit of the experiments [88]. Because the evaporation accommodation is not the focus of this study, and it adds further complication, we assume $\alpha = 1$, thereby giving a high prediction value of the amount of evaporation. In addition, we assume that the lubricant is evaporated into rarefied air that has no lubricant molecules in a vapor state ($p_i = 0$). We consider this a reasonable assumption when the disk linear velocity is around 10 m/s, thereby quickly shearing away recently evaporated lubricant. Therefore, the evaporation model used here is represented by the following equation:

$$\dot{m}(T, M_w, h) = \frac{M_w}{\sqrt{2\pi RT}} p_{vap,\infty} \exp\left(\frac{M_w}{\rho RT} [-\Pi - \gamma \nabla^2 h]\right) \quad (5.8)$$

Density

Density appears in the governing equation as an evaporation term. The variation of density in thin liquid PFPE films on solid substrates has been studied numerically with Monte Carlo simulations [89]. Those authors found that the density of the polymer decreases near the surface, and they suggested this decrease in density is due to resistance to the diffusion of polymers by the impenetrable surface. According to the plots in [89], the density of films less than 2-nm thick is about 10% less than the two sublayers above. So we approximate the thin-film density in our simulations of systems < 2 nm as 10% less than the bulk Zdol 2000 density value given in the Fomblin Z Derivatives Data Sheet: $\rho = 1630$ kg/m³.

5.2 Non-dimensional Governing Equations for HAMR Writing and Recovery Conditions

During HAMR writing, a scanning thermal spot drives lubricant deformation. After writing, the disk rapidly cools to ambient temperature and the lubricant recovers back to a flat interface. Schematics of the lubricant system under writing and recover conditions are shown in Figure 5.4. The same governing lubricant equation is used for both the HAMR writing and recovery processes. Because the thermal spot driver is absent in the recovery simulations, the non-dimensionalization of the governing equation is reconfigured. This section describes the non-dimensionalization schemes of the lubrication equation for the HAMR writing and recovery processes.

Write Simulation

The lubricant pressure and shear stresses balance the applied pressure and shear stresses. In Section 5.1, the external pressure and shear stresses acting at the lubricant-air interface

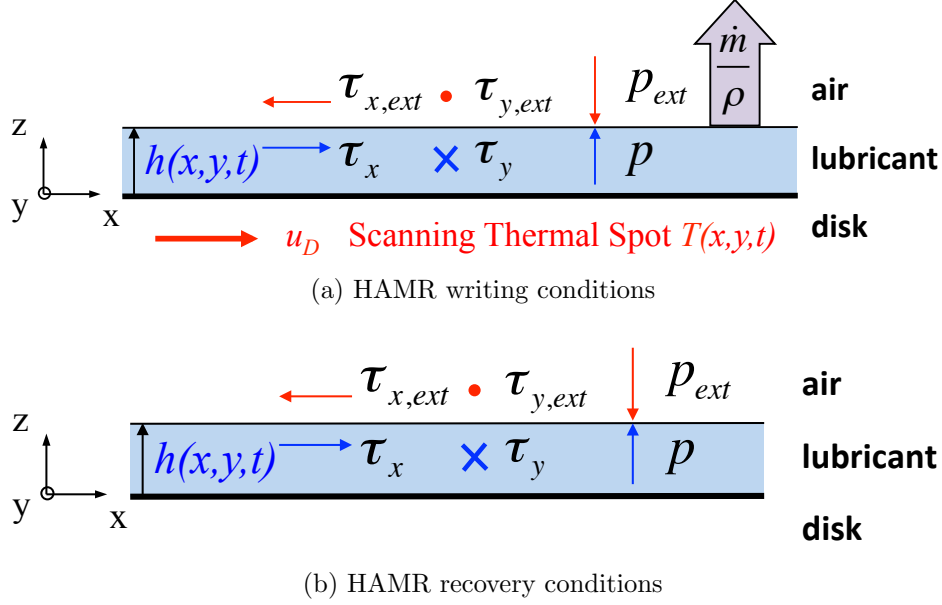


Figure 5.4: Schematics of the lubricant system under HAMR writing and recovery conditions.

were determined (Equations 5.1, 5.4, and 5.3):

$$\begin{aligned}
 p &= p_{ext} = -\Pi - \gamma \nabla^2 h \\
 \tau_x &= \tau_{x,ext} = \frac{d\gamma}{dT} \frac{\partial T}{\partial x} \\
 \tau_y &= \tau_{y,ext} = \frac{d\gamma}{dT} \frac{\partial T}{\partial y}
 \end{aligned}$$

Inserting these expressions into the lubricant's thickness evolution equation (Equation 2.13) and designating $c = -\frac{d\gamma}{dT} > 0$, we obtain the dimensional governing equation for the lubricant under HAMR writing conditions as

$$\begin{aligned}
 \frac{\partial h}{\partial t} + u_D \frac{\partial h}{\partial x} + \frac{\partial}{\partial x} \left[\frac{h^3}{3\eta} \frac{\partial}{\partial x} (\Pi + \gamma \nabla^2 h) - \frac{h^2}{2\eta} c \frac{\partial T}{\partial x} \right] \\
 + \frac{\partial}{\partial y} \left[\frac{h^3}{3\eta} \frac{\partial}{\partial y} (\Pi + \gamma \nabla^2 h) - \frac{h^2}{2\eta} c \frac{\partial T}{\partial y} \right] + \frac{\dot{m}}{\rho} = 0
 \end{aligned} \tag{5.9}$$

We use a similar non-dimensionalization scheme as Wu [75]. The obvious non-dimensionalizations are based on system parameters of initial lubricant thickness h_0 , prescribed temperature profile FWHM L , ambient temperature T_0 , maximum prescribed temperature rise $\Delta T = T_{max} - T_0$, and initial ambient lubricant properties $\eta_0 = \eta(T_0, h_0)$ and $\gamma_0 = \gamma(T_0)$:

$$\begin{aligned}
 h_* &= h h_0 & x_* &= x L & y_* &= y L \\
 \eta_* &= \eta \eta_0 & \gamma_* &= \gamma \gamma_0 & T_* &= T \Delta T + T_0
 \end{aligned} \tag{5.10}$$

We now switch to the notation that quantities with the asterisk subscript are dimensional and the quantities without the asterisk subscript are non-dimensional. The temporal t_s and pressure p_s scales as well as the non-dimensional advection velocity C_u and evaporation source term S are determined in the non-dimensionalization process so that all quantities in the governing equation are of order one and have no coefficient.

$$t_* = t t_s \quad p_* = p p_s \quad \text{where } p_* = \Pi_* \text{ or } \gamma_* \nabla^2 h_* \quad (5.11)$$

Substituting Equations 5.10 and 5.11 into Equation 5.9 and multiplying by $\frac{2\eta_0 L^2}{h_0^2 c \Delta T}$ so that the thermocapillary shear stress terms have a coefficient of one, we determine that the scales and coefficients are as follows:

$$\begin{aligned} t_s &\equiv \frac{2\eta_0 L^2}{h_0 c \Delta T} & p_s &\equiv \frac{3}{2} \frac{c \Delta T}{h_0} \\ C_u &\equiv \frac{2\eta_0 L}{h_0 c \Delta T} u_D & S &\equiv \frac{2\eta_0 L^2}{h_0^2 c \Delta T} \frac{\dot{m}}{\rho} \end{aligned} \quad (5.12)$$

The final non-dimensional governing equation for the lubricant flow and evaporation simulations is:

$$\begin{aligned} \frac{\partial h}{\partial t} + C_u \frac{\partial h}{\partial x} + \frac{\partial}{\partial x} \left[\frac{h^3}{\eta} \frac{\partial}{\partial x} (p_{disj} + p_{Lap}) - \frac{h^2}{\eta} \frac{\partial T}{\partial x} \right] \\ + \frac{\partial}{\partial y} \left[\frac{h^3}{\eta} \frac{\partial}{\partial y} (p_{disj} + p_{Lap}) - \frac{h^2}{\eta} \frac{\partial T}{\partial y} \right] + S = 0 \end{aligned} \quad (5.13)$$

where $p_{disj} = \Pi/p_s$ and $p_{Lap} = \gamma \nabla^2 h/p_s$.

Reflow Simulation

After HAMR writing, the disk is assumed to have instantly cooled back to ambient temperature. Therefore, during lubricant recovery there is no temperature gradient to induce a surface tension gradient and the external shear stresses are zero. The force balance at the lubricant-air interface under the lubricant recovery conditions is:

$$\begin{aligned} p &= p_{ext} = -\Pi - \gamma \nabla^2 h \\ \tau_x &= \tau_y = 0 \end{aligned}$$

We choose a coordinate system fixed to the spinning disk, so the advective effects are not needed in the governing equation. Substituting the determined lubricant pressure and shear stresses into Equation 2.13 and eliminating the unnecessary advective term, we obtain the dimensional governing equation for lubricant recovery:

$$\frac{\partial h}{\partial t} + \frac{\partial}{\partial x} \left[\frac{h^3}{3\eta} \frac{\partial}{\partial x} (\Pi + \gamma \nabla^2 h) \right] + \frac{\partial}{\partial y} \left[\frac{h^3}{3\eta} \frac{\partial}{\partial y} (\Pi + \gamma \nabla^2 h) \right] = 0 \quad (5.14)$$

The obvious non-dimensionalizations are based on system parameters of initial lubricant thickness h_0 , initial viscosity $\eta_0 = \eta(T_0, h_0)$, and disjoining pressure derivative at the initial lubricant thickness $\frac{d\Pi}{dh}|_{h_0} = \Pi'_0$.

$$h_* = h h_0 \quad \Pi'_* = \Pi' \Pi'_0 \quad \eta_* = \eta \eta_0 \quad (5.15)$$

The temporal t_s and length L_s scales are determined in the non-dimensionalization process so that all quantities in the governing equation are of order one and have no coefficient.

$$t_* = t t_s \quad x_* = x L_s \quad y_* = y L_s \quad (5.16)$$

The chain rule is used on disjoining pressure: $\frac{\partial \Pi}{\partial x} = \frac{d\Pi}{dh} \frac{\partial h}{\partial x}$. Substituting Equations 5.15 and 5.16 into Equation 5.14, we determine that the scales and coefficients are as follows:

$$t_s \equiv \frac{3\eta_0\gamma}{h_0^3(\Pi'_0)^2} \quad L_s \equiv \left(\frac{\gamma}{\Pi'_0}\right)^{1/2} \quad (5.17)$$

Hydrodynamic linear stability analysis predicts that periodic perturbations of the lubricant-air interface with wavenumber greater than $1/L_s$ will grow in time until the film ruptures (dewetting instability); $4t_s$ is the reciprocal of the maximum temporal growth coefficient, and because the growth of the perturbation is dominated by the fastest growing perturbation, the time to film rupture is taken to be of the order of $4t_s$ [90]. We could have chosen t_s to be equal to the time of rupture, and the result would have been a constant coefficient in front of the temporal term in our governing equation. The final non-dimensional governing equation for the lubricant recovery simulations is:

$$\frac{\partial h}{\partial t} + \frac{\partial}{\partial x} \left[\frac{h^3}{\eta} \Pi' \frac{\partial h}{\partial x} + \frac{h^3}{\eta} \frac{\partial}{\partial x} (\nabla^2 h) \right] + \frac{\partial}{\partial y} \left[\frac{h^3}{\eta} \Pi' \frac{\partial h}{\partial y} + \frac{h^3}{\eta} \frac{\partial}{\partial y} (\nabla^2 h) \right] = 0 \quad (5.18)$$

5.3 Numerical Simulation Tool

The numerical scheme used to solve the non-linear governing lubricant equations for HAMR writing (Equation 5.13) and recovery (Equation 5.18) is based on the simulation code developed by H. Kubotera [91]. Equations 5.13 and 5.18 are discretized using the control volume method [47]. First derivatives are approximated by the second-order accurate central difference scheme, and the second derivatives in the Laplacian operator are approximated by a fourth-order accurate second derivative finite difference scheme. The code takes advantage of the symmetry in y (cross-track direction, no skew). At the edge of the sufficiently large computation domain, the temperature is ambient and the Dirichlet boundary conditions are $h = h_0$.

For the HAMR writing simulation, the governing hyperbolic equation is divided into its non-advective (Eulerian) and advective (Lagrangian) phases. First the non-advective part is iteratively solved using a Gaussian elimination scheme until the convergence criterion is

met. Once the Eulerian phase is advanced, the advective phase is solved using the Cubic Interpolated Propagation (CIP) scheme [92, 93]. With no advection velocity in the y direction, our solution is one dimensional with regard to the advection scheme. A cubic interpolation function $F(x)$ between spatial grid points uses matching conditions of both the physical value $h(x, t)$ as well as it's first spatial derivative $\frac{\partial h}{\partial x}$, and this interpolant is used to advance $h(x, t)$ and $\frac{\partial h}{\partial x}$ from time n to $n + 1$.

Chapter 6

Simulation of Lubricant Deformation During HAMR Writing

6.1 Introduction

The lubricant is a critical component of the HDI that protects the disk and recording head from damage due to intermittent contacts during normal drive operations when the recording head is flying over the spinning disk with a minimum clearance < 5 nm and relative velocity around 10 m/s. The HAMR lubricant must be able to withstand the writing process in which the disk is locally heated a few hundred degrees Celsius within a few nanoseconds to reduce the coercivity of the media and allow writing of data.

Several experimental studies have investigated depletion mechanisms of conventional lubricants, usually Zdol or Ztetraol, due to localized heating. The Tagawa group at Kansai University have developed a spinstand unit to test lubricant-coated hard disks subject to an optically focused laser with a relatively large spot diameter of 900 nm. In these studies in which a slider was not flying over the disk and the maximum temperature achieved in most experiments was less than 100°C , the effects of the lubricant thickness, bonding ratio, molecular weight, end-group, and laser power have been investigated [94–97]. Experimentalists at the Data Storage Institute in Singapore have also developed a HAMR tester, which includes an optically focused $0.9\text{--}1\ \mu\text{m}$ laser spot heating the disk to an estimated maximum temperature as high as 360°C ; however the laser had to be scanned back and forth to create irradiation tracks $10\text{--}20\ \mu\text{m}$ wide in order for the lubricant depletion to be visible on the optical surface analyzer [98–101].

Lubricant flow and evaporation under HAMR writing conditions have been studied numerically as well. Wu developed a continuum-based lubricant flow model under a scanning laser (laser intensity profile assumed Gaussian with standard deviation 33.33 nm), and he found that evaporation removes a majority of lubricant from the disk surface when it is heated to 301°C within 20 ns while thermocapillary shear stress and thermoviscosity have a smaller effect [75]. Wu and Talke improved upon this model by solving the Fourier heat con-

duction problem in a multi-layered HAMR disk to determine the disk surface temperature driving the lubricant flow [76]. Similar HAMR lubricant simulations were conducted by Zeng et al. [77], and those authors investigated the effects of evaporation enthalpy, initial film thickness, and evaporation coefficient on lubricant depletion due to a Gaussian profile laser beam with standard deviation 33.33 nm and maximum disk surface temperature calculated to be 281°C. Matsuoka et al. [72] analyzed lubricant deformation considering a temperature and film thickness dependence of surface tension, which they derived from integration of a corrected van der Waals pressure equation, subjecting the lubricant to a Gaussian temperature profile with standard deviation 1 μm and maximum temperature rise of 100°C. Most lubricant simulation results in the literature have included only the component of disjoining pressure due to long-range van der Waals interactions with a form $1/h^3$, or in the case of [72] surface tension enhanced by van der Waals forces of the form $1/h^2$, and therefore simulate non-functional lubricants. Zhou et al. [102] did include a polar disjoining pressure component, but their simulation results investigated only evaporation rate and not lubricant flow on the disk. Lubricants with functional end-groups are likely to be used, so disjoining pressure that includes more than van der Waals interactions should be considered in HAMR lubricant modeling. The strong interactions between the functional end-groups and the disk substrate is expected to also create a restricted layer having an effective viscosity much larger than the mobile layers above it or the bulk lubricant [27].

Measurable lubricant deformation in non-HAMR hard drives can compromise the mechanical stability of the HDI through slider flying modulations or lubricant loss [103, 104], leading to poor read/write efficiency. In one particular experimental study, drops introduced on the disk surface with height 1.0–2.0 nm and lateral dimensions 50–100 μm caused up to 100 nm of slider flying height displacement over the first 10 revolutions before the slider gradually removed the lubricant drop obstacle [105]. Though the amplitude was only 0.2–0.3 nm, periodic ripples induced larger slider flying height modulations via a resonance effect on slider dynamics, with a peak flying height modulation of 0.8 nm (mean to peak), which resulted in a flying height loss of ~ 2 nm [106]. Few experimental studies addressing slider-lubricant interactions for HAMR system have been published [107], but it is expected that HAMR writing lubricant deformation that results in obstacles around 1 nm in height or periodic disturbances around 0.2 nm in amplitude are undesirable. As HAMR slider-lubricant interaction research progresses, other types of lubricant deformation that compromise slider flying dynamics and read/write performance may be discovered.

In this chapter we use the simulation tool described in Chapter 5 that incorporates film thickness dependencies of viscosity and additional contributions to disjoining pressure due to functional end-groups to predict lubricant flow on a HAMR disk surface. Simulations are carried out for length and time scales unobservable with current experimental capabilities: illumination times of a few nanoseconds and laser spot sizes less than 100 nm. We investigate the effect of the total disjoining pressure and thin-film viscosity on evaporation and lubricant flow for different initial thicknesses. We also consider how lubricant depletion changes with laser spot size and thermal spot maximum temperature.

6.2 Simulations Under HAMR Write Conditions

In the HAMR writing process, a complicated laser delivery system transfers enough energy to the magnetic layer to heat it above its Curie temperature so that the magnetic field generated by the magnetic write pole can reverse the magnetic polarization of the recording bits. We perform simulations that investigate how the lubricant flows and evaporates under write conditions due to the scanning thermal spot.

The transfer of electromagnetic energy from the laser diode, through the waveguide, to the near-field transducer where the energy is partially converted to electronic plasmons, and finally conveyed through the nanometers-thick air bearing, lubricant, and overcoat to the magnetic layer is a complicated and not well understood nanoscale heat transfer problem. We avoid these complications by prescribing a Gaussian temperature profile on the rotating disk surface to approximate the final result of the HAMR laser delivery system. We assume the 1–2-nm lubricant layer has the same temperature as the disk surface because it is so thin. For all simulations that follow, the ambient conditions are $T_0 = 25^\circ\text{C}$ and $p_0 = 101325 \text{ Pa} = 1 \text{ atm}$. All simulations are for Zdol 2000, with a molecular weight of 2 kg/mol.

In these simulations we do not include the air bearing pressure and shear stress or electrostatic pressure. Those effects are left to the subject of another lubricant study.

Driving Forces of Lubricant Distortion

The instigator of lubricant deformation under HAMR write conditions is the scanning thermal spot. Our model for the HAMR lubricant considers various lubricant properties that depend on local temperature and lubricant deformation: surface tension, disjoining pressure, vapor pressure, and viscosity. Of these properties and their effects resulting from the applied temperature gradient, the ones that drive lubricant deformation are the surface tension gradient (thermocapillary shear stress) and evaporation. Evaporation affects the lubricant distortion by removing lubricant and forming a depletion trough.

Thermocapillary shear stress pulls lubricant from areas of hot (low surface tension) to cold (high surface tension), thereby driving lubricant to flow outward from the thermal spot center forming a trough and side ridges. The low viscosity at the thermal spot center enhances the thermocapillary shear flow by increasing lubricant mobility. As shown in Figure 6.1, without the inclusion of viscosity temperature dependence, there is no significant lubricant distortion. The thickness dependence of viscosity, that is the increased viscosity due to stronger intermolecular forces as the film gets thinner, mitigates the amount of lubricant pulled away from the thermal spot center for thinner lubricant systems.

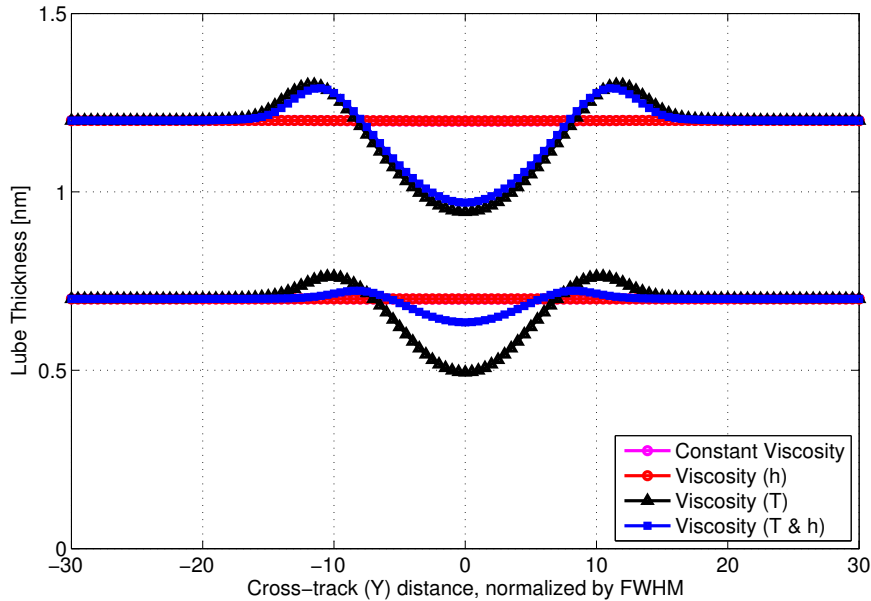


Figure 6.1: Thermocapillary shear stress, with assistance from thermoviscosity, is a main contributor to lubricant flow under HAMR writing conditions. Evaporation is set to zero in these simulations. If the temperature dependence of viscosity is included (denoted (T) in the legend), a significant amount of lubricant is drawn from the thermal spot center to side ridges in the cooler, higher viscosity regions. The thickness dependence of viscosity (denoted (h) in the legend) mitigates the amount of lubricant pulled away from the thermal spot center for thinner lubricant systems.

Disjoining Pressure Study

Disjoining pressure can affect the lubricant in two ways according to our model. The disjoining pressure value affects evaporation (Equation 5.8). The disjoining pressure gradient drives lubricant flow from areas of high to low pressure (Equation 5.13). Because disjoining pressure is a function of lubricant thickness only, the product of the disjoining pressure derivative and the lubricant-air interface gradient determine the direction of this pressure gradient: $\nabla\Pi = \frac{d\Pi}{dh}\nabla h$. The disjoining pressure varies substantially with lubricant thickness, so we consider four thicknesses: 0.5 nm, 0.7 nm, 1.2 nm, and 1.4 nm. These four lubricant systems are subjected to $t_f = 2$ ns of illumination by a 20-nm FWHM thermal spot scanning at a velocity $u_D = 5$ m/s. The maximum center temperature is $T_{max} = 350^\circ\text{C}$. The lubricant has a molecular weight of 2 kg/mol (Zdol 2000). Four cases at each lubricant thickness are considered: (1) no disjoining pressure ($\Pi = 0$), (2) the dispersive component ($\Pi = \Pi^d$), (3) the polar component ($\Pi = \Pi^p$), and (4) the total disjoining pressure ($\Pi = \Pi^d + \Pi^p$).

Disjoining Pressure Effect on Evaporation

In the first set of simulations, we include all effects (thermocapillary shear stress, thermoviscosity with thickness dependence, Laplace pressure, and thin-film evaporation) for different components of disjoining pressure. The value of disjoining pressure can enhance or inhibit evaporation through its effect on vapor pressure.

The cross-track lubricant profiles at time $t_f = 2$ ns for the case when evaporation is included are shown in Figure 6.2. All lubricant profiles exhibit a center trough at the maximum temperature location ($y = 0$); this depletion zone is created by mass removal through evaporation and outward mass flow due to thermocapillary shear stress. The side ridges are due to the thermocapillary shear stress. The inclusion of one or both components of disjoining pressure results in a smaller maximum trough depth for all lubricant thicknesses compared with cases excluding disjoining pressure. Disjoining pressure suppresses lubricant removal and flow compared with a bulk film, though the degree of this mitigation depends on the lubricant thickness.

The suppression effect of disjoining pressure on lubricant deformation can be explained by analyzing the direction of the thermocapillary shear stress and disjoining pressure gradient. Thermocapillary shear stress always drives lubricant away from the thermal spot center. For Zdol lubricant systems thinner than 1.5 nm, the total disjoining pressure derivative is negative. With the formation of a trough due to evaporation and flow initiated by thermocapillary shear stress, the ∇h points outward from the thermal spot center. Therefore with the negative sign from $\frac{d\Pi}{dh}$, the disjoining pressure gradient $\nabla\Pi$ points inward toward the thermal spot center, the opposite direction of the thermocapillary shear stress.

The thinner lubricants experience little change due to the thermal spot because of the thin-film enhancements to viscosity and suppression of evaporation (Figure 6.2a). The peak-to-peak cross-track profile change for $h_0 = 0.5$ nm is less than 0.022 nm for cases that included disjoining pressure, a deformation below the resolution of most optical instruments used to measure lubricant thickness. So for practical purposes, this simulation result for $h_0 = 0.5$ nm can be interpreted as no lubricant deformation. For the $h_0 = 0.7$ nm lubricant system, slight deformation is predicted, ranging from 0.15-nm peak-to-peak variation for the case considering only Π^d to 0.092-nm peak-to-peak for the case including the total disjoining pressure.

For the thicker lubricant systems, the inclusion of the polar component of disjoining pressure results in less lubricant deformation compared with the cases including only the dispersive component or no disjoining pressure (Figure 6.2b). With only dispersive disjoining pressure, the peak-to-peak lubricant deformation is 0.7 nm; this deformation is roughly twice the peak-to-peak deformation when either the polar or total disjoining pressure is considered (0.36 nm). For $h_0 = 1.4$ nm, the deformation is greater but the discrepancy when including the polar component or total disjoining pressure is a little smaller: 0.85-nm peak-to-peak for the dispersive component and 0.56-nm peak-to-peak for the polar or total disjoining pressure.

The amount of lubricant removed during 2 ns of thermal spot illumination is plotted in Figure 6.3. Note that the mass of one Zdol PFPE molecule is $M_w/N_A = 0.32\text{e-}24$ kg. When

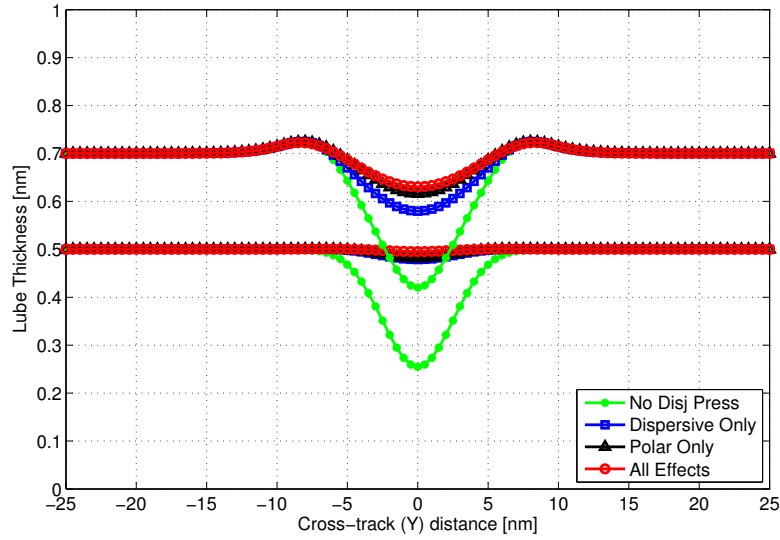
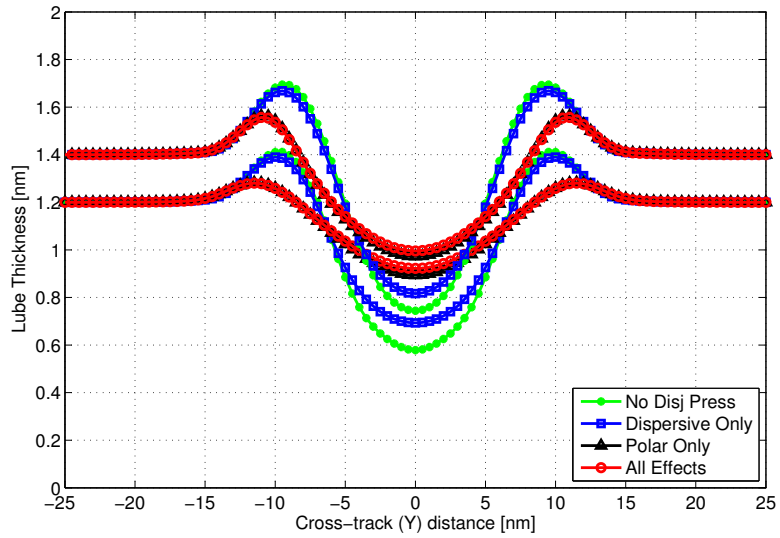
(a) $h_0 = 0.5$ and 0.7 nm(b) $h_0 = 1.2$ and 1.4 nm

Figure 6.2: Disjoining pressure study: Cross-track profiles at the center of the depletion trough for lubricant systems of different thicknesses. Thin lubricant systems show little deformation for cases that including disjoining pressure. For thicker films, the inclusion of polar disjoining pressure suppresses lubricant deformation compared with cases without this component. $t_f = 2$ ns, $u_D = 5$ m/s, $T_{max} = 350^\circ\text{C}$, FWHM = 20 nm.

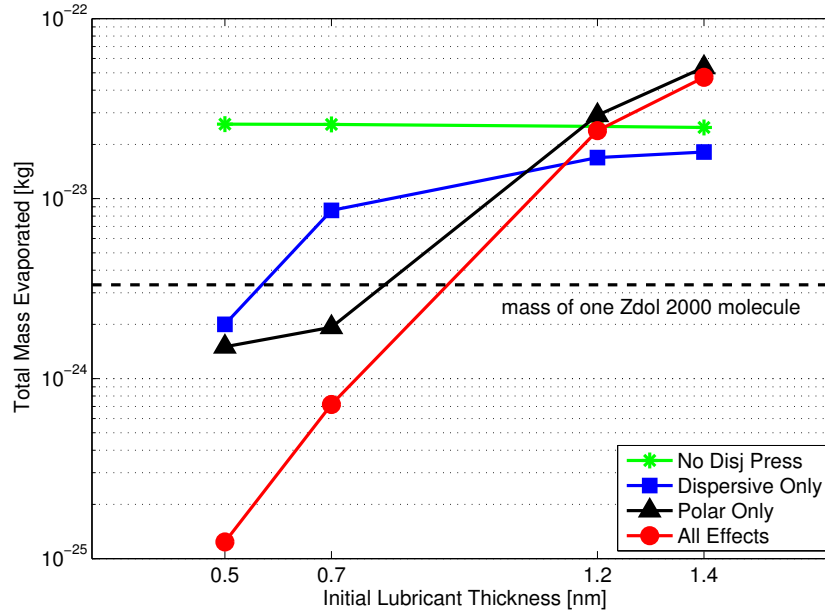


Figure 6.3: Disjoining pressure study: Amount of mass evaporated after 2 ns of illumination by the laser with a scanning speed 5 m/s. The variation in disjoining pressure with lubricant thickness determines the evaporation rate.

disjoining pressure is excluded, the amount of evaporative mass loss is relatively constant across the four lubricant thicknesses. Dispersive disjoining pressure significantly mitigates evaporation for thinner lubricant systems but has a smaller effect in thicker systems. The polar disjoining pressure significantly suppresses evaporation for the thinner lubricants where $\Pi^p > 0$ and enhances evaporation over bulk lubricant evaporation for systems thicker than about 1 nm, where $\Pi^p < 0$. When total disjoining pressure is considered for the thinner lubricant systems, the amount of evaporative mass removal is much less than for cases considering the components in isolation. Above 1 nm, where the polar disjoining pressure dominates the total disjoining pressure curve and $\Pi < 0$, the amount of mass evaporated for total disjoining pressure follows the polar component curve of evaporation enhancement.

As further illustration of the lubricant properties dictating lubricant deformation, the instantaneous evaporative mass flux and viscosity at 2 ns just before the thermal spot is turned off are plotted in Figures 6.4 and 6.5. The evaporation is several orders of magnitude higher at the thermal spot center than at the edges of the domain where the lubricant temperature is close to ambient. The viscosity is much higher for the thinner lubricant systems meaning that it is much harder for the pressure gradients and thermocapillary shear stress to drive the lubricant flow.

The final Laplace pressure profiles for the simulations that include all effects are plotted

for the four lubricant thicknesses in Figure 6.6. All lubricant systems are subjected to the same temperature profile and hence the same surface tension profile $\gamma(T)$. So the Laplace pressure $\gamma\nabla^2h$ plotted in Figure 6.6 provides a comparison of the interface mean curvatures ($\kappa = \nabla^2h/2$). The magnitude and gradient of curvature increase with lubricant thickness, implying that the Laplace pressure contribution to the lubricant flow is stronger in the thicker lubricant systems. However, we shall see in an order of magnitude analysis that the amount of lubricant flow driven by the Laplace pressure and disjoining pressure gradients is smaller than the amount driven by thermocapillary shear stress for this system.

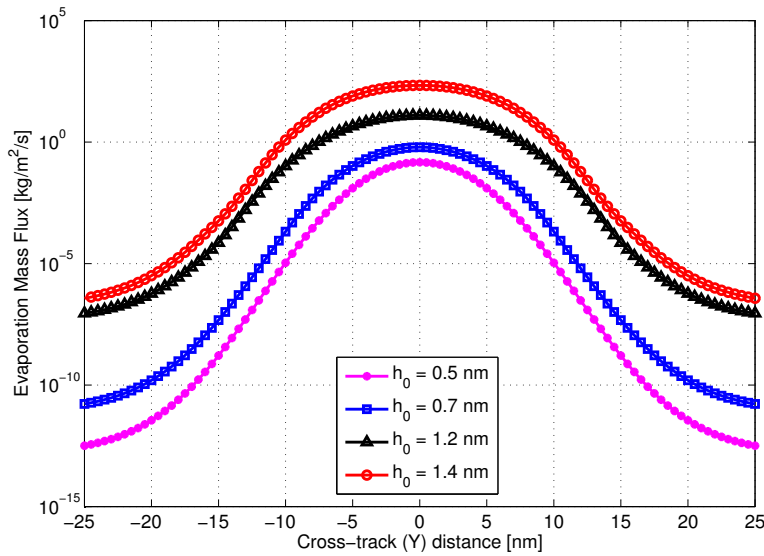


Figure 6.4: Disjoining pressure study: Instantaneous evaporative mass flux at 2 ns for the cases considering total disjoining pressure $\Pi = \Pi^d + \Pi^p$. Thinner lubricants have orders of magnitude lower evaporation rates compared with thicker lubricants.

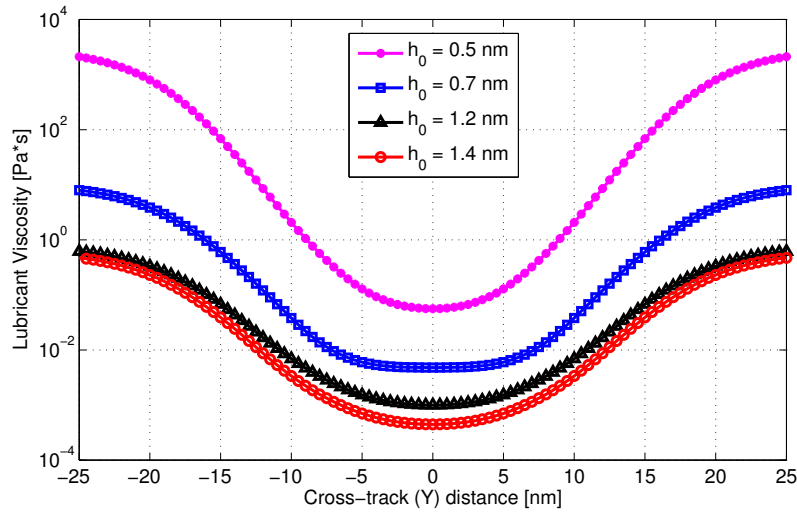


Figure 6.5: Disjoining pressure study: Instantaneous lubricant viscosity at 2 ns for the cases considering total disjoining pressure $\Pi = \Pi^d + \Pi^p$. Thinner lubricants have orders of magnitude higher viscosity compared with thicker lubricants.

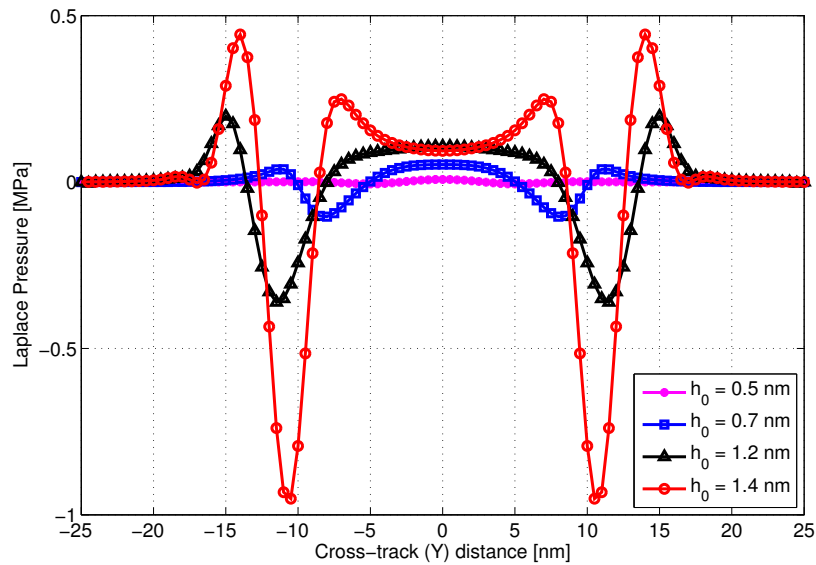


Figure 6.6: Disjoining pressure study: Final Laplace pressure for the cases considering total disjoining pressure $\Pi = \Pi^d + \Pi^p$. Laplace pressure and hence interface curvature become more severe as the lubricant thickens.

Disjoining Pressure Gradient Effect on Lubricant Flow

In order to isolate the disjoining pressure gradient $\nabla\Pi$ effect on lubricant flow, we suppress the evaporation in this analysis. We point out that in regimes where $\frac{d\Pi}{dh} > 0$, the lubricant film can become unstable [20, 73] so that the film spontaneously thickens and thins to form droplets. We repeat the simulations presented above but here the evaporation is set to zero. The resulting lubricant profiles at 2 ns are plotted in Figure 6.7 for the four lubricant thicknesses.

For the thin lubricant systems, there are no significant differences between the disjoining pressure cases and the amount of deformation is very small (Figure 6.7a). For $h_0 = 0.5$ nm, the maximum peak-to-peak lubricant thickness difference is only 0.0045 nm. For practical purposes, this simulation result is interpreted as no lubricant deformation. The polar component of the disjoining pressure derivative is positive and is therefore in the unstable regime (see Figure 5.2b for $h = 0.5$ nm), but the high viscosity keeps the lubricant from becoming unstable. The $h_0 = 0.7$ nm system shows more lubricant deformation with a maximum peak-to-peak thickness change of approximately 0.09 nm and a similar trough minimum within 0.02 nm between the four cases. The analysis presented below shows that thermocapillary shear stress is the dominant flow force at $h_0 = 0.7$ nm, so the differences in disjoining pressure derivative across the four cases do not significantly impact the final lubricant profile.

The thicker lubricant systems show significantly more lubricant deformation, on the order of a few tenths of nanometers (Figures 6.7b). Including the polar disjoining pressure component mitigates lubricant flow away from the thermal spot center. For lubricant thicknesses greater than 1 nm, Π^p dominates the Π profile (Figure 5.2), so it is expected that the lubricant profile for total disjoining pressure will closely match that for cases including only the polar component. The peak-to-peak thickness changes are 0.32 nm for $h_0 = 1.2$ nm and 0.53 nm for $h_0 = 1.4$ nm, which are very close to the peak-to-peak values for the cases when evaporation was considered (0.36 nm and 0.56 nm, respectively). Eliminating evaporation still resulted in several Angstroms of lubricant deformation, and we will show next that this is due to thermocapillary shear stress.

Relative Strengths of Lubricant Flow Driving Effects

To compare the relative strengths of the forces driving lubricant flow, we calculate the terms in the governing equation at their characteristic values for each lubricant system. The characteristic lubricant thickness is the initial thickness h_0 and the characteristic temperature gradient is the maximum temperature change $\Delta T = T_{max} - T_0 = 325^\circ\text{C}$ divided by the thermal spot FWHM $L = 20$ nm. The derivative of the disjoining pressure is evaluated at the initial thickness: $\Pi'_0 = \left. \frac{d\Pi}{dh} \right|_{h_0}$. The spatial derivatives of the lubricant thickness and Laplace pressure are taken to be the peak-to-peak profile change divided by the distance over which that change occurs Δy , essentially a linear approximation of major cross-track profile features from Figures 6.2 and 6.6. The characteristic flow forces are taken from inside

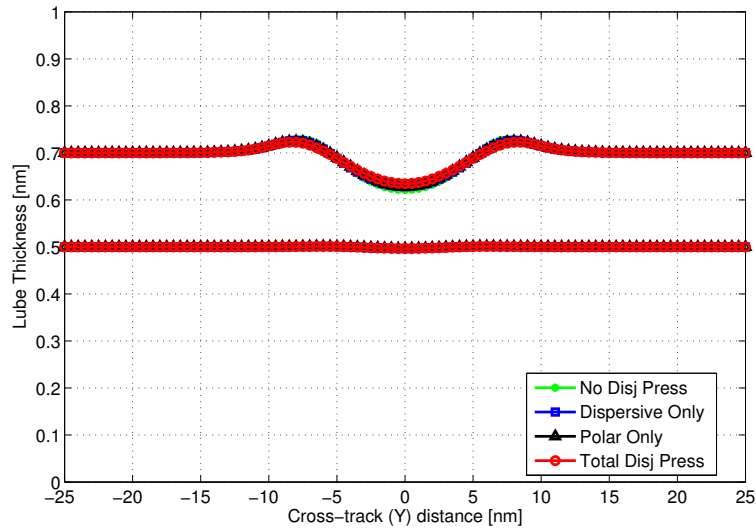
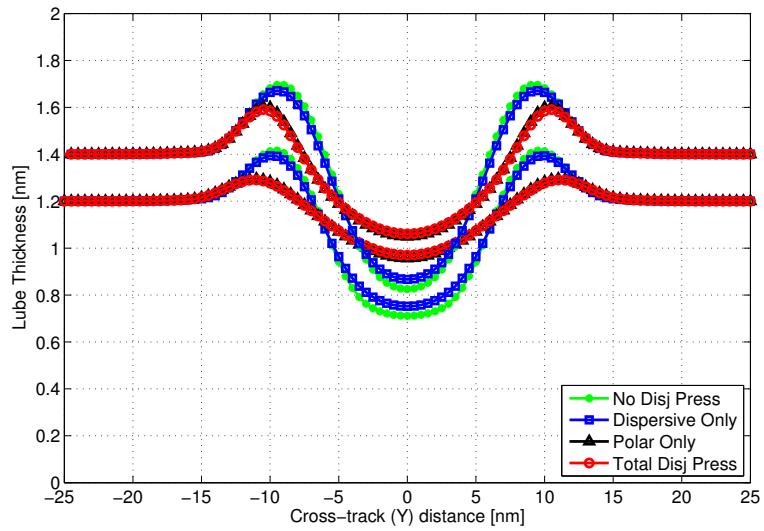
(a) $h_0 = 0.5$ and 0.7 nm(b) $h_0 = 1.2$ and 1.4 nm

Figure 6.7: Disjoining pressure study with no evaporation: Cross-track profiles at the center of the depletion trough for lubricant systems of different thicknesses with evaporation suppressed. Total disjoining pressure suppresses lubricant flow away from the thermal spot center for thicker lubricants but has little effect for thin lubricant system. $t_f = 2$ ns, $u_D = 5$ m/s, $T_{max} = 350^\circ\text{C}$, FWHM = 20 nm.

the divergence term of the dimensional governing evolution equation:

$$\begin{aligned} \text{Thermocapillary shear stress:} \quad F_\gamma &= \frac{h_0^2}{2\eta_0} \frac{d\gamma}{dT} \frac{\Delta T}{L} \\ \text{Disjoining pressure:} \quad F_\Pi &= \frac{h_0^3}{3\eta_0} \Pi_0' \frac{\Delta h}{\Delta y} \\ \text{Laplace pressure:} \quad F_{Lap} &= \frac{h_0^3}{3\eta_0} \frac{\Delta p_{Lap}}{\Delta y} \end{aligned}$$

Table 6.1 presents the ratio of the thermocapillary shear characteristic flow force F_γ to the other flow forces, i.e. flow driven by the disjoining pressure gradient F_Π and the Laplace pressure gradient F_{Lap} . All entries in Table 6.1 are greater than one, meaning that at these characteristic values the thermocapillary shear stress is responsible for most of the lubricant flow. For thin lubricant systems, F_{Lap} is several orders of magnitude smaller than F_γ and F_Π , so it can be neglected for very thin films. For the thicker lubricant films, all flow forces are of the same order of magnitude; the thermocapillary shear stress driven flow is 1–5 times the value of the pressure gradient driven flows.

Table 6.1: Comparison of characteristic forces driving lubricant flow for different lubricant thicknesses. $\Delta T = 325^\circ\text{C}$, thermal spot size FWHM 20 nm. Thermocapillary shear stress is the dominant flow force for thin lubricant thicknesses and the major flow force in thicker lubricant systems.

h_0	F_γ/F_Π	F_γ/F_{Lap}
0.5 nm	48.0	719
0.7 nm	3.20	29.4
1.2 nm	1.21	5.09
1.4 nm	2.29	1.75

Thin-Film Viscosity Study

The addition of the thin-film effect on viscosity is a new contribution of this work. Previous HAMR lubricant simulations based on continuum theory have included only the temperature dependence of viscosity. We conducted simulations at each thickness for two cases: (1) ignoring the thickness dependence of viscosity $\eta_\infty(T)$ and (2) including the temperature and thin-film effects on viscosity $\eta(T, h)$ (Equation 5.5).

The thin-film viscosity effect is more important in thinner lubricant films than thicker films (Figure 6.8). The thinner lubricants show little deformation (< 0.1 nm peak-to-peak) if the thickness dependence on viscosity is included, while ignoring this dependence results in significant lubricant distortion (peak-to-peak variations of 0.27 nm for $h_0 = 0.5$ nm and 0.53 nm for $h_0 = 0.7$ nm). In contrast, including viscosity thin-film effects for thicker

lubricants does not appreciably change the predicted lubricant deformation. In Figure 6.8b, the lubricant profiles for the two viscosity cases lie practically on top of each other for both lubricant thicknesses. These thin-film viscosity results can be explained by examining the viscosity at the final lubricant profiles for all cases, plotted in Figure 6.9. The thin-film viscosity of the thicker lubricants is in close proximity to and of the same order of magnitude as the temperature-only dependent viscosity. However, for the thinner lubricant systems the thin-film viscosity is several orders of magnitude higher than the temperature-only model. The high viscosity results in high resistance to flow, which can be interpreted the same as in the bonded layer, and therefore it causes little lubricant deformation.

Thus the thin-film enhancement of viscosity is important to include in simulations for lubricants less than about 1-nm thick; otherwise, ignoring viscosity's dependence on film thickness results in unrealistically large lubricant deformation.

Thermal Spot Size Study

Numerous challenges still need to be overcome before a target thermal spot FWHM of 25 nm is reached. In the mean time, larger thermal spots will be generated on the HAMR disk in the design process. Here a larger prescribed thermal spot is used with the same conditions as those employed in the previous studies. Four film thicknesses are subjected to a thermal spot maximum temperature of 350°C for four thermal spot sizes: FWHM of (1) 1 μm , (2) 100 nm, (3) 50 nm, and (4) 20 nm. All lubricant properties and thin-film effects are considered. The aim is to determine if the characteristics of the lubricant profiles change with larger thermal spot sizes when attaining the same maximum temperature on the disk.

To directly compare the lubricant profiles, we normalize the cross-track coordinate by the thermal spot FWHM. For both the large and small thermal spots, the deformations of the thin $h_0 = 0.5$ nm lubricant systems are quite small with essentially no deformation (Figure 6.10a). For $h_0 = 0.7$ nm, the smallest 20-nm FWHM thermal spot resulted in a noticeable trough and side ridges while the larger thermal spots caused smaller deformation, with the largest 1- μm FWHM spot causing a negligible lubricant distortion and no side ridges. The thicker lubricant systems show more lubricant deformation for all thermal spot sizes (Figure 6.10b). The smaller thermal spots cause a trough and side ridges with several Angstroms of peak-to-peak lubricant profile change. As the thermal spot becomes smaller, the side ridge height increases and the side ridge peak moves further away from the thermal spot center in the FWHM normalized coordinates. The largest spot again causes only a trough and no side ridges. It is interesting to note how quickly the thermal spot becomes large enough to have negligible side ridges, indicating a weaker thermocapillary shear stress: the 100-nm FWHM thermal spot lubricant profiles closely resemble the large 1- μm FWHM profiles, but not the 20-nm FWHM profiles even though the thermal spot sizes are closer. The governing equation is highly nonlinear and contains coupled terms, leading to this surprisingly sharp thermocapillary shear stress trend with thermal spot size in the FWHM range 20–100 nm.

The result of using a larger spot to achieve the same peak temperature is a smaller temperature gradient, which means lower thermocapillary shear stress. The ratio of the

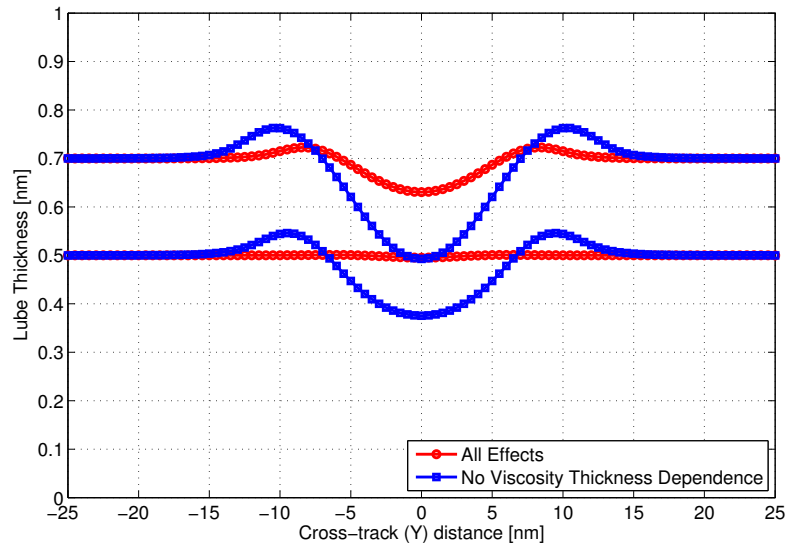
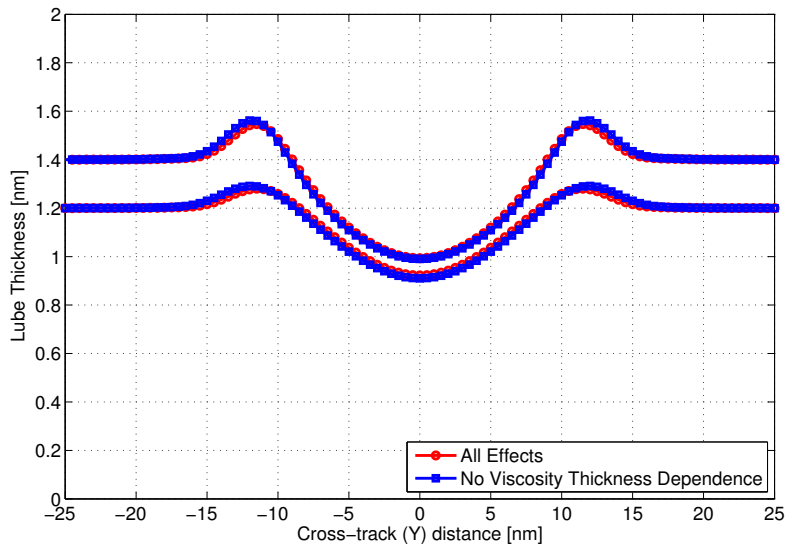
(a) $h_0 = 0.5$ and 0.7 nm(b) $h_0 = 1.2$ and 1.4 nm

Figure 6.8: Thin-film viscosity study: Cross-track profiles of viscosity at the center of the depletion trough for lubricant systems of different thicknesses. Thin-film viscosity is important to consider for thinner lubricants, but it has a smaller effect on lubricant flow for thicker lubricants. $t_f = 2$ ns, $u_D = 5$ m/s, $T_{max} = 350^\circ\text{C}$, FWHM = 20 nm.

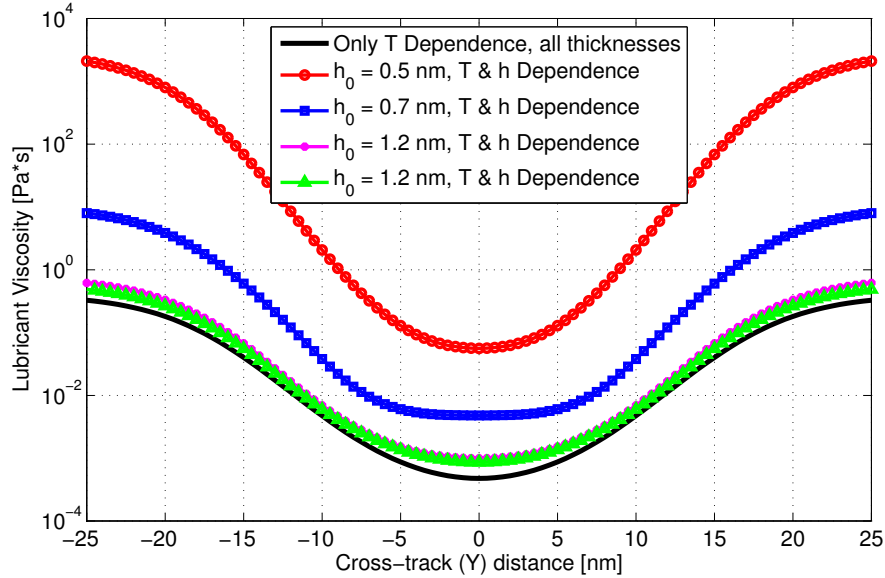


Figure 6.9: Thin-film viscosity study: Viscosity at final lubricant profiles with and without thickness dependence of viscosity. For thick films, neglecting thickness dependence results in similar viscosity values. For thin films, neglecting the thickness dependence of viscosity predicts a value several orders of magnitude lower than the thin-film viscosity model. $t_f = 2$ ns, $u_D = 5$ m/s, $T_{max} = 350^\circ\text{C}$, FWHM = 20 nm.

magnitude of maximum shear stresses $\tau = \frac{d\gamma}{dT} \nabla T$ between to simulations of different thermal spot sizes is equal to the ratio of the characteristic temperature gradients $(T_{max} - T_0)/\text{FWHM}$. Therefore, increasing the thermal spot FWHM by a factor of 50 reduces the thermocapillary shear stress by a factor of 50. The thermocapillary shear stress is too weak in the large spot system to pull lubricant into side ridges, and the resulting trough is mainly due to evaporation. A large thermal spot for which side ridges disappear for the Zdol 2000 simulated in this work appears to be a FWHM greater than 100 nm. For smaller thermal spot sizes, thermocapillary shear stress is the main driver of lubricant deformation, pulling lubricant away from the thermal spot center to the side ridges, while evaporation is not as important and deformation is similar whether the evaporation is ‘on’ or ‘off’ (comparing Figure 6.2b to Figure 6.7b).

To directly compare the amount of mass evaporated during the 2 ns of laser illumination, a normalized mass quantity needs to be determined. The total mass evaporated m_{evap} is an integral of the evaporative mass flux over space and time, which is a discretized sum over all control volumes and time steps in our numerical simulation. Because area contributes to the total mass evaporated, we can scale m_{evap} by a characteristic area, thereby normalizing to thermal spot size. Any measure of area we determine for our axisymmetric Gaussian temperature profile is proportional to the square of the FWHM, L^2 , so we use this quantity

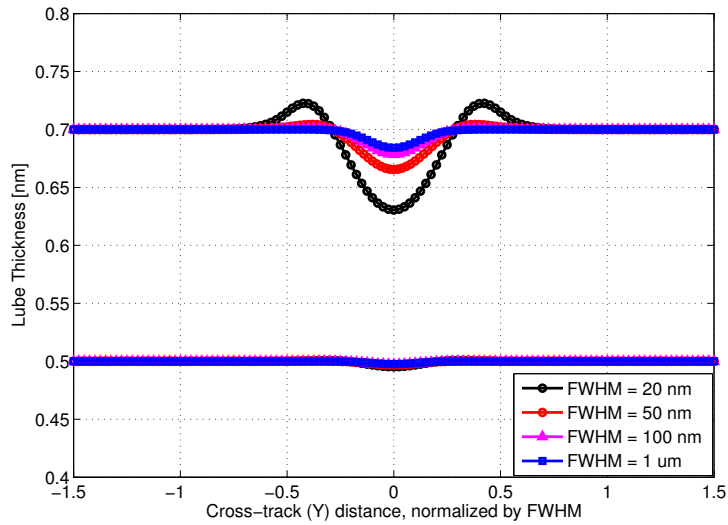
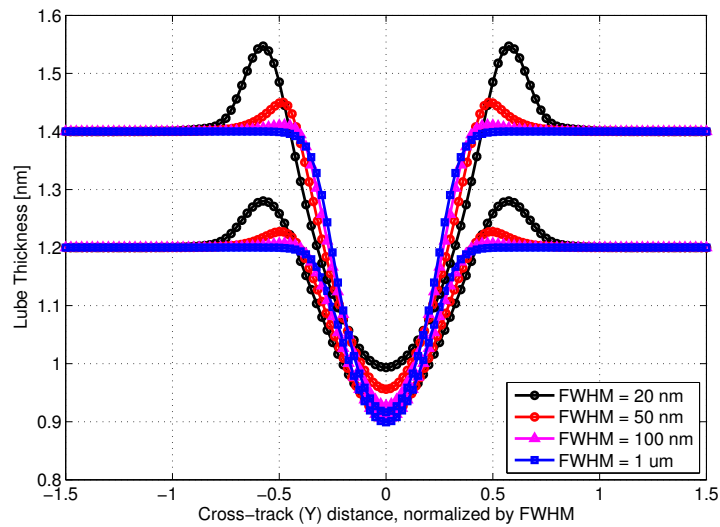
(a) $h_0 = 0.5$ and 0.7 nm(b) $h_0 = 1.2$ and 1.4 nm

Figure 6.10: Thermal spot size study: Cross-track profiles at the center of the depletion trough for lubricant systems of different thicknesses and thermal spot sizes. The cross-track coordinate is normalized by the thermal spot FWHM. The small spot profiles have side ridges due to thermocapillary shear stress while the largest spot profiles show no side ridges, only a trough due to evaporation. $t_f = 2$ ns, $u_D = 5$ m/s, $T_{max} = 350^\circ\text{C}$.

to normalize m_{evap} . Define the normalized evaporated mass as

$$\bar{m}_{evap} \equiv \frac{m_{evap}}{L^2} \quad (6.1)$$

The values of \bar{m}_{evap} for all cases are listed in Table 6.2. The thermal spot sizes have comparable \bar{m}_{evap} values. For all thicknesses, the larger thermal spot size has the highest \bar{m}_{evap} (except for 0.5 nm), and the smallest thermal spot has the smallest \bar{m}_{evap} . \bar{m}_{evap} increases with both increasing film thickness and increasing thermal spot size, almost monotonically except for the 0.5 nm thickness.

Table 6.2: Normalized total evaporated mass \bar{m}_{evap} (kg/m²) for four thermal spot sizes. The amount of normalized evaporated mass is comparable between the all thermal spot sizes.

Spot Size	0.5 nm	0.7 nm	1.2 nm	1.4 nm
20-nm FWHM	3.09e-10	1.79e-09	5.96e-08	1.18e-07
50-nm FWHM	3.10e-10	2.07e-09	8.06e-08	1.47e-07
100-nm FWHM	3.11e-10	2.16e-09	8.13e-08	1.53e-07
1- μ m FWHM	3.10e-10	2.20e-09	8.19e-08	1.53e-07

Maximum Temperature Study

Up to this point, all simulations have been for a prescribed Gaussian temperature profile that achieves a maximum temperature of 350°C . In effect, we have kept the laser power of the HAMR system constant. Here we investigate how lubricant deformation changes with maximum disk temperature, a consequence of varying the laser power, for a fixed initial lubricant thickness. For the 1.2 nm lubricant system, we illuminate the lubricant with a 20-nm FWHM thermal spot scanning at a speed of 5 m/s for 2 ns. The maximum temperature of the thermal spot is varied: $T_{max} = 30^\circ\text{C}$, 150°C , 300°C , 450°C , and 600°C .

A higher maximum temperature for a fixed thermal spot size increases the temperature gradient and has two effects: (1) the evaporation rate is higher and (2) the temperature gradient increases, resulting in a stronger thermocapillary shear stress. As shown in Figure 6.11, as T_{max} increases, the trough becomes wider and deeper and the side ridges grow. No significant lubricant deformation is predicted below 150°C . The bottom of the trough in the $T_{max} = 600^\circ\text{C}$ simulation is flat, indicating that for this lubricant model and peak temperature, the lubricant is not easily thinned below 0.3 nm. The resistance to lubricant flow (thin-film viscosity) and evaporation (thin-film evaporation) is too high.

If we ignore chemical decomposition and thermal degradation of the molecule, we imply that only complete Zdol molecules can evaporate from the thin film. According to Figure 6.12, no Zdol 2000 molecules are evaporated for T_{max} below approximately 300°C . What little deformation is present at these low temperatures is due to thermocapillary shear stress.

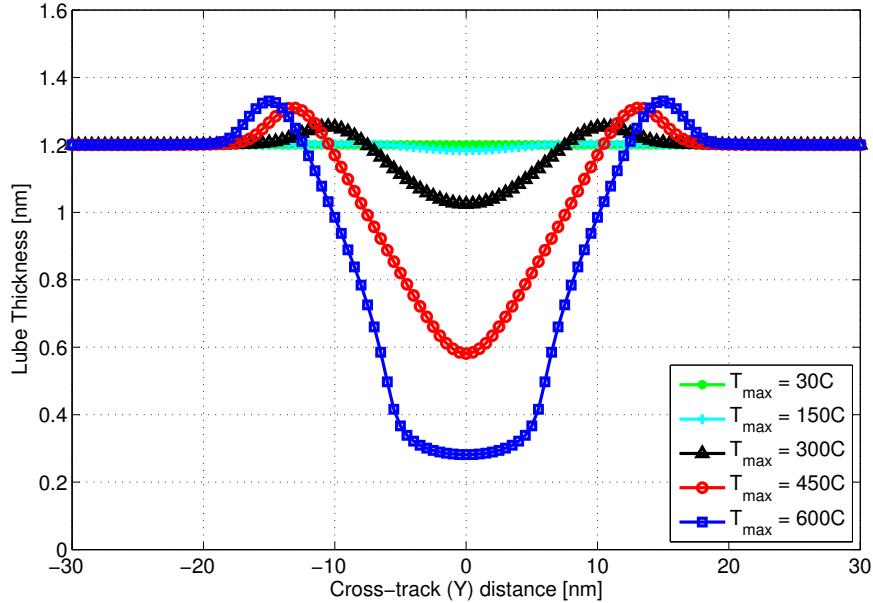


Figure 6.11: Maximum temperature study: Comparison of lubricant cross-track profiles for different thermal spot maximum temperatures. The lubricant depletion zone width and depth increase with increasing thermal spot maximum temperature. FWHM = 20 nm, $h_0 = 1.2$ nm, $u_D = 5$ m/s.

Note that thermal decomposition of bulk Fomblin Zdol occurs at temperatures above 350°C [22, 23], so our high temperature simulations should not be interpreted as a quantitative analysis.

6.3 Discussion

We have shown that several Angstroms of lubricant deformation is possible after 2 ns of thermal spot illumination for some cases. For a thermal spot maximum temperature of 350°C, the thinner film systems of 0.5 and 0.7 nm thickness have mild peak-to-peak deformation of less than 0.1 nm for all cases simulated. For the same thermal spot illumination, the thicker systems of 1.2 and 1.4 nm thickness show possibly significant peak-to-peak deformation ranging from 0.30–0.56 nm. Recalling that 0.2–0.3 nm amplitude periodic ripples were observed to induce relatively large slider flying height modulations via a resonance effect [106], we note that it is possible that the lubricant deformation due to laser heating in thicker lubricants could also degrade the slider dynamics if the deformation is periodic, for example if the laser is pulsed. We have not investigated slider-lubricant interactions under HAMR writing conditions, so there could be further lubricant deformation and slider dynamic instabilities

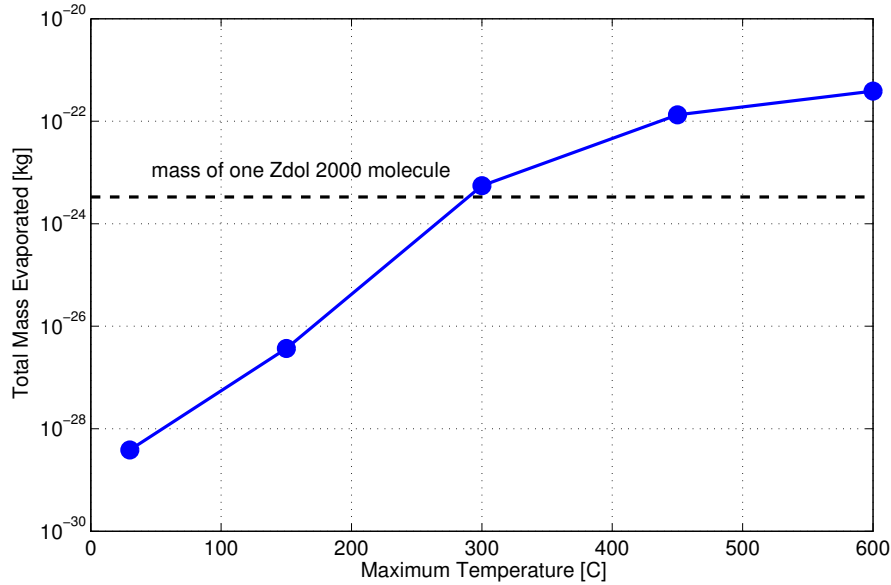


Figure 6.12: Maximum temperature study: Comparison of total mass evaporated in 2 ns of thermal spot illumination time for different thermal spot maximum temperatures. The mass of one molecule of Zdol 2000 (M_w/N_A) is indicated by the horizontal dashed line. If thermal decomposition is ignored, significant mass loss due to evaporation does not occur below $\sim 300^\circ\text{C}$. FWHM = 20 nm, $h_0 = 1.2$ nm, $u_D = 5$ m/s, $t_f = 2$ ns.

due to the mutual influences.

While experimental data for Zdol 2000 under laser illumination is published, direct comparison of simulation results with these published data is difficult because of unknown system parameters and excessive computation time needed to reproduce many of the experiments. Experimental papers in the literature report the laser spot diameter on the disk surface, which we understand to be assumed from the objective lens specifications or approximated by some experimental means. The exact temperature profile on the disk during laser illumination is unknown. A single value for the local temperature increase on the disk surface due to laser heating has been estimated from changes in disk surface optical properties [108]; in these experiments, the authors report the “width of the effective region” heated by the 900 nm diameter laser spot was found to be “approximately 10 μm in the radial direction”. So it is possible that the temperature profile could be larger than the reported laser spot size. The thermal spot size is one of the main determinants of the magnitude of lubricant deformation. For an initial lubricant thickness of 0.99 nm and a thermal spot maximum temperature range of 310–345 $^\circ\text{C}$, our simulations predict a 30–40% decrease in trough depth when the thermal spot FWHM is reduced from 6 μm to 1 μm . In the absence of experimentally determined disk temperature profiles, we can only guess from the measured depletion profiles what is the

thermal spot FWHM, assuming the actual temperature profile is Gaussian. Additionally, the time between laser illumination and measurement of the lubricant profile is usually not reported; it is possible that the lubricant partially recovers before the lubricant profile is measured. Our lubricant recovery simulations of the profiles from Figure 6.10 predict significant recovery within 1 s after the thermal spot illumination ceases. Simulation of several laser passes, either on one track [94–96] or on adjacent tracks to illuminate an arc [99–101], is computationally prohibitive at this time; the computation time would be on the order of several months. Our disjoining pressure model is only applicable up to thicknesses around 2.5 nm because the model is a polynomial fit to data from lubricant systems up to only 2 nm thickness; beyond 2.5 nm thickness, the disjoining pressure model predicts unrealistic values for Π^p . However, we directly compare with one set of experiments from the literature, making assumptions about simulation input parameters, and qualitatively compare with others. In addition, insights into the published experimental results are made from our simulation results.

The best candidate for direct comparison with published experimental results is the work of Tagawa et al. [97] which presents a plot of lubricant depletion depth after one disk revolution versus laser power for Zdol 2000 systems of 0.99 nm and 2.12 nm thicknesses. Their experimental procedure involved only one laser pass, and the thicknesses are within the regime of applicability of the disjoining pressure model. We replicate one pulse of the 300 kHz laser (1.67 μ s of laser on-time) and estimate the thermal spot FWHM to be 6 μ m based on the width of the trough in the cross-track profiles presented in [97]. The maximum temperature at each laser power is estimated from [108]. We expect our simulations to over-predict the evaporation as we have assumed an ideal evaporation coefficient of one. Indeed, at the end of 1.67 μ s of illumination by a 18–22-mW laser spot, we predict a roughly 0.4 nm deeper trough than reported in [97, Figure 4]. The agreement between our simulation results and the results shown in that figure is within 0.05 nm at lower power levels (≤ 11 mW or $\leq 205^\circ\text{C}$), but this is not notable because the amount of deformation is measured to be 0.05 nm or less. Other reasons for the discrepancy between our simulations and their reported trough depths beyond over-predicting evaporation include possible lubricant recovery between the end of the laser illumination and a difference between the actual thermal profile on the disk from what we used as an input into our simulation.

In another study, Tagawa et al. [95] found that after 10 minutes of illumination by a 5-mW laser ($T_{max} \approx 100^\circ\text{C}$ [108]) on what is understood to be a single track, the lubricant profile had a significant trough depth (0.40–2.08 nm) and comparatively small width (67–82 μ m) for lubricant films thicker than one monolayer (> 1.2 nm). In contrast, the trough depth was small (0.05–0.07 nm) and the width relatively large (170–287 μ m) for lubricant films with thicknesses less than one monolayer. We do predict a trough several Angstroms deeper for a 2 nm film compared to a 1 nm film immediately after illumination by a $T_{max} = 222 - 239^\circ\text{C}$, 6- μ m FWHM thermal spot, but the widths are close to the thermal spot FWHM for both thicknesses. Our relatively small predicted widths are possibly due the lubricant being considered a viscous fluid, whereas PFPE lubricants are known to exhibit some viscoelastic behavior. A wide deformation due to a point source could be attributed to an elastic-

like response of the lubricant. Also, there may be deformation phenomena that arise with approximately 36,000 laser passes in 10 minutes that are not evident in a simulation of a single laser pass.

Tagawa et al. [94] illuminated different lubricants of thicknesses larger than 2 nm with a 5-mW laser ($T_{max} \approx 100^\circ\text{C}$ [108]) for a single disk revolution and 60 revolutions. For the 60 revolution cases they observed a raised ridge on the outer diameter side of the track, but no raised ridges for the one revolution cases. The laser spot size on the disk surface was reported to be 900 nm in diameter, which may or may not correspond to the size of the thermal spot generated on the disk surface. Based on our results in Section 6.2, a small temperature rise less than 100°C above ambient and a large thermal spot with a FWHM of several hundred nanometers or more is expected to generate a negligible thermocapillary shear stress and the observed deformation is mainly due to evaporation. The raised ridge at the outer diameter edge of the depletion track in [94] could be due to air shearing stresses, as the authors conjectured, or possibly centripetal acceleration effects due to the disk rotation, effects we did not include in our simulations. These effects may have relatively long time scales and only be visible after tens of disk revolutions.

Several experimental results from the Digital Storage Institute show raised ridges on both sides of the depletion track with the outer diameter edge usually higher [99–101]. In these experiments, the laser progressed on the disk surface in the radial direction from the inner to outer diameter to create a 10–20- μm depletion track visible by an optical surface analyzer. The outer edge of the depletion track may exhibit more accumulation because the laser was scanned from the inner to the outer radius, creating a leading edge accumulation zone similar to roller processes, as well as air shearing stress and centripetal acceleration.

Qualitatively, our simulation results show similar trends as other simulation studies of Zdol-type lubricants under HAMR conditions. These trends include lubricant depletion zone width and depth increase with disk surface temperature, side ridges forming due to thermocapillary shear stress, and thickness dependence of the severity of lubricant depletion [72, 75–77].

The simulations by Wu [75, 76] show more lubricant deformation due to evaporation and a smaller thermocapillary shear stress effect than we predict for similar simulation conditions. We share the same governing evolution equation, but this equation incorporates models for lubricant properties of viscosity, evaporation, disjoining pressure, and surface tension. Even when we suppress the polar component and use similar conditions ($h_0 = 1.45$ nm, FWHM = 80 nm, $\Delta T = 265^\circ\text{C}$, $t_f = 20$ ns), the plots in [75] show a deeper trough ($h_0 - h_{min} \approx 1.06$ nm) than we predict ($h_0 - h_{min} = 0.142$ nm). Additionally, our simulations predict notable thermocapillary shear stress side ridges, while plots in [75] show no side ridges. Our evaporation models are different than the model given in [75, 76], which predicts a higher evaporation rate according to our comparison simulations. Other researchers replicated Wu’s lubricant depletion model and also found that it over-predicts evaporation compared with Tagawa’s experiments [88]. In [75], evaporation is suppressed to isolate thermocapillary shear stress, similar to Figure 6.1 in this paper. We conducted similar simulations with only the dispersive disjoining pressure acting and no evaporation. While we predict 0.098-nm peak-

to-peak distortion in the down-track profile, [75, Figure 5(b)] shows approximately 0.016-nm peak-to-peak deformation. Our viscosity must decrease faster with temperature than the one employed in [75, 76], where the general form of the viscosity model is provided but not the values of the coefficients.

These HAMR writing lubricant deformation studies are for Zdol 2000, a common lubricant in hard drives a decade ago. Modern lubricants such as Ztetraol and ZTMD have more functional end-groups that interact more strongly with the carbon overcoat; therefore the disjoining pressure, viscosity, surface tension, and evaporation models should probably be different from Zdol property models. Stronger lubricant-carbon overcoat interactions imply that the lubricant is more difficult to move and evaporate, so the amount of deformation due to thermal spot scanning is expected to be less for a lubricant such as Ztetraol in comparison with the simulation results we present here for Zdol 2000. For future studies, we will add the capability to simulate other lubricant types by incorporating disjoining pressure models for Ztetraol and ZTMD based on experimental studies [21, 109]. Suitable experimental data must also be found for the vaporization energy variation with molecular weight for Ztetraol and ZTMD; we expect the vaporization energy will increase linearly with molecular weight as with Zdol, but the constants will differ. In addition, flow activation energy and entropy are properties needed for the viscosity model.

This continuum mechanics model is only as good as the incorporated lubricant property models, most notably the disjoining pressure and viscosity. It is possible that surface tension γ_{LV} isn't a viable quantity when the system consists of one or two monolayers. Maybe there should be one quantity to represent the enhanced intermolecular forces. Marchon and Saito have approached this concept with the temperature dependent Hamaker constant [28].

In this chapter, we have not considered thermal decomposition or the polydispersity. Experiments suggest thermal decomposition of Zdol consists of cleavage of the fluorinated ether backbone at temperatures above 350°C [22, 23], meaning the disk could be covered with severed Zdol molecules having only one functional end-group after the writing process. Lubricant properties such as viscosity and disjoining pressure would change due to the different nature of the polymer molecules. More experimental studies of thermal decomposition processes and kinetics of the leading contender for the HAMR lubricant are needed, and these results could be incorporated into an improved continuum model to predict HAMR lubricant behavior. Lubricants on hard drives are not pure materials, but rather a mixture of different molecular weight components. Because evaporation is strongly dependent on molecular weight, the degree of polydispersity determines how the evaporation rate changes with time as the lighter molecules evaporate first [102, 110].

In this chapter, we have shown several Angstroms of lubricant deformation under HAMR writing for several cases. How the lubricant recovers after the thermal spot has passed is the subject of the next chapter.

6.4 Conclusion

We have developed a continuum model to predict HAMR lubricant behavior on the disk under write conditions. The effects of functionalized end-groups on disjoining pressure and thin-film viscosity are considered. Under an applied thermal spot, lubricant deformation is driven by the surface tension gradient (thermocapillary shear stress) and evaporation. The low viscosity at the thermal spot center enhances the thermocapillary shear flow by increasing the lubricant's mobility. Total disjoining pressure suppresses lubricant removal and flow compared with models that consider only the van der Waals force contribution to disjoining pressure, though the degree of this mitigation depends on the lubricant thickness. Above 1-nm thickness, evaporation is enhanced over the bulk value for the particular Zdol disjoining pressure model used here because the disjoining pressure is negative. Thinner lubricants less than 1 nm have orders of magnitude lower evaporation rates and higher viscosities compared with thicker lubricants, which means lubricant depletion is harder to achieve for very thin films if the lubricant does not thermally decompose. For simulations of lubricants less than about 1 nm thick, ignoring viscosity's dependence on film thickness results in unrealistically large lubricant deformation. A larger thermal spot size, above 100-nm FWHM, generates a lower thermocapillary shear stress that becomes too weak to pull lubricant into side ridges for the $T_{max} = 350^{\circ}\text{C}$ cases studied, and the resulting trough is mainly due to evaporation. This is in contrast to the smaller thermal spots which have a higher temperature gradient: thermocapillary shear stress is the main driver of lubricant deformation, pulling lubricant away from the thermal spot center to the side ridges, while evaporation is not as important and deformation is similar whether the evaporation is considered or not. No significant lubricant deformation is predicted at temperature below 150°C for a 2-ns thermal spot illumination time. As the thermal spot maximum temperature increases, the lubricant depletion zone depth and width increase. This work is a first step toward the simulations of functional lubricants under HAMR write conditions. Future improvements to the model should include consideration of viscoelastic, thermal decomposition, and polydispersity effects and the ability to simulate more complicated lubricants.

This chapter presents work published in Tribology Letters [111].

Chapter 7

Simulation of Lubricant Recovery After HAMR Writing

7.1 Introduction

The HAMR lubricant must be able to withstand the writing process in which the disk is locally heated a few hundred degrees Celsius within a few nanoseconds to reduce the coercivity of the media and allow writing of data. In addition, the lubricant must be able to recover the depletion and accumulation zones induced by HAMR writing so as to allow for stable flying heights and reliable read/write performance. In Chapter 6, we simulated the distortion of thin Zdol films due to a thermal spot during HAMR writing and predicted several Angstroms of depletion in some cases. In particular, for a 20-nm FWHM thermal spot reaching a maximum temperature of 350°C, systems with thickness greater than 1 nm show possibly significant peak-to-peak deformation ranging from 0.30–0.56 nm. In this chapter, we continue these simulations into the recovery period in order to evaluate HAMR system factors that can lead to better HDI performance.

Experimental studies of lubricant recovery suggest that the lubricant depletion zone due to HAMR writing may not recover by the next laser pass in approximately 6–15 ms, the time for one disk revolution in 10,000–4000 RPM drives, at least for the laser spot sizes used in the experiments. Though their experiments involved scanning a laser back and forth, not a single laser pass as we simulate, Ma et al. [99, Figure 3] show a significant trough of depth of 0.8 nm for an initially 1.2-nm-thick functionalized lubricant 5 minutes after laser illumination. In a similar paper, these authors report that a 0.5-nm peak-to-peak lubricant depletion is relaxed to less than 0.1 nm trough depth after 5 hours of recovery [100, Figure 2]. Though not the same initial deformation as resulting from HAMR writing, the free surface spreading of PFPE lubricants relaxing from a sharp stair-step interface shows significant changes after several minutes of spreading [112, 113]. Thus the several Angstrom deep troughs in HAMR lubricants after writing could be present for subsequent laser passes in the immediately following disk revolutions.

A significant amount of lubricant deformation can compromise the mechanical stability of the HDI through slider flying modulations or lubricant loss [103, 104] and lead to poor read/write efficiency. In one particular experimental study, drops of lubricant introduced on the disk surface of height 1–2 nm and lateral dimensions 50–100 μm caused up to 100 nm of slider flying height increase over the first 10 revolutions before the slider gradually removed the lubricant drop obstacle [105]. Though the amplitude was only 0.2–0.3 nm, periodic ripples induced slider flying height modulations via a resonant effect on slider dynamics, with a peak flying height modulation of 0.8 nm (mean to peak), which resulted in a flying height loss of ~ 2 nm with 3σ [106]. Few experimental studies addressing slider-lubricant interactions for HAMR systems have been published [107], but it is expected that HAMR writing lubricant deformation that results in obstacles or periodic disturbances would be undesirable.

Numerical studies of lubricant recovery based on continuum lubrication theory have been conducted for conventional (non-HAMR) hard drive systems. Early lubricant recovery flow simulations using a constant viscosity indicate that the time scale for the initially 5-nm thick lubricant to replenish a 100- μm -wide, 3-nm-deep trough is several minutes [114]. Ma et al. [115] numerically investigated the effect of functional end-groups, molecular weight, and carbon overcoat on lubricant recovery into a 1- μm diameter hole using the diffusion equation; those authors used experimental data from the spreading of a sharp stair-step lubricant interface to determine the diffusion coefficient thickness dependence and predicted critical reflow time. While several authors have simulated lubricant flow and evaporation under HAMR writing conditions [75, 76, 98], to our knowledge simulations of recovery of the trough and side ridges after HAMR writing have yet to be published in the literature.

In this chapter we use our simulation tool described in Chapter 5 to study Zdol lubricant recovery on the disk surface following HAMR writing. We present recovery simulation results for length and time scales unobservable with current experimental capabilities: laser spot sizes less than 1 μm and lubricant recovery in the first few microseconds after laser illumination. We investigate how initial thickness, thermal spot size during HAMR writing, and thermal spot maximum temperature affect Zdol lubricant recovery after HAMR writing.

7.2 Simulations of Recovery After HAMR Writing

The simulations of lubricant recovery start from an initial profile that is the final profile upon completion of HAMR writing from Chapter 6. For HAMR writing, a Gaussian temperature profile with a maximum temperature $T_{max} = 350^\circ\text{C}$ and varying full width at half maximum (FWHM) scanned the lubricant surface with speed 5 m/s for a duration of 2 ns. The ambient conditions are $T_0 = 25^\circ\text{C}$ and $p_0 = 101325 \text{ Pa} = 1 \text{ atm}$. All simulations are for Zdol 2000 with a molecular weight of 2 kg/mol.

We investigate how initial lubricant thickness and the thermal spot size used in HAMR writing affect lubricant recovery. Three thicknesses are considered: 0.7 nm, 1.2 nm, and 1.4 nm. Three thermal spot sizes are considered: (1) 20-nm FWHM, close to the targeted ther-

mal spot size of 25-nm FWHM for 5 Tb/in² HAMR recording density [12], (2) 1- μ m FWHM, the approximate size of laser spots used in many experimental setups from the literature, and (3) an intermediary size of 100-nm FWHM. In the previous chapter, writing simulations were performed for an initial lubricant thickness of 0.5 nm, but the deformation was very small, everywhere within 0.01 nm of the initial thickness. So there is no need to perform lubricant recovery simulations for the 0.5-nm lubricant because there it is practically undeformed under the simulated writing conditions.

Recovery simulations are run until the lubricant recovers to within 0.01 nm of the initial lubricant thickness, close to the resolution of optical surface analyzers that measure lubricant thickness. Table 7.1 lists the recovery times for the three thermal spot sizes and the three lubricant thicknesses. We show in an upcoming section that the Laplace pressure has a minor effect on lubricant recovery speed and profile shape, so it is neglected for the 20-nm and 100-nm FWHM cases to speed up the computation time. The 20-nm FWHM case had the fastest recover times at all thicknesses: with recovery times in tens of microseconds, the 20-nm FWHM recovers an order of magnitude faster than the 100-nm FWHM case (hundreds of microseconds) and four orders of magnitude faster than the large 1- μ m FWHM case (tens of milliseconds). The 20-nm and 100-nm FWHM cases exhibit the fastest recovery times for the 1.2-nm thickness while the 1- μ m FWHM case had monotonically increasing recovery time with increasing film thickness. Though the recovery times listed in Table 7.1 are longer for the largest 1- μ m FWHM thermal spot, still the interface becomes quite flat by the next time the slider comes around. After 15 ms of recovery time, the 0.7-nm lubricant is within 0.0107 nm of its initial thickness, the 1.2-nm lubricant recovers to within 0.0168 nm, and the 1.4-nm lubricant to within 0.0420 nm. The lubricant profiles at several times in the recovery process are plotted in Figure 7.1. To directly compare the lubricant profiles, we normalize the cross-track coordinate by the thermal spot FWHM.

Table 7.1: Recovery time to within 0.01 nm of initial thickness for various thermal spot sizes (FWHM) and initial thicknesses. Laplace pressure is omitted for the 20-nm and 100-nm FWHM cases to speed up computation time.

Spot Size	0.7 nm	1.2 nm	1.4 nm
20-nm FWHM	94.3 μ s	10.2 μ s	28.2 μ s
100-nm FWHM	384 μ s	256 μ s	802 μ s
1- μ m FWHM	17.8 ms	25.5 ms	81.1 ms

The trough recovery rate is a figure of merit for lubricant recovery. The amount of depletion in the trough is greater than the amount of accumulation in the side ridges (if present), so the trough is the last to recover and therefore determines recovery time. The trough recovery rate plotted in Figure 7.2 is the result of a backward difference approximation of the rate of change of the global minimum point h_{min} between time steps n and $n - 1$

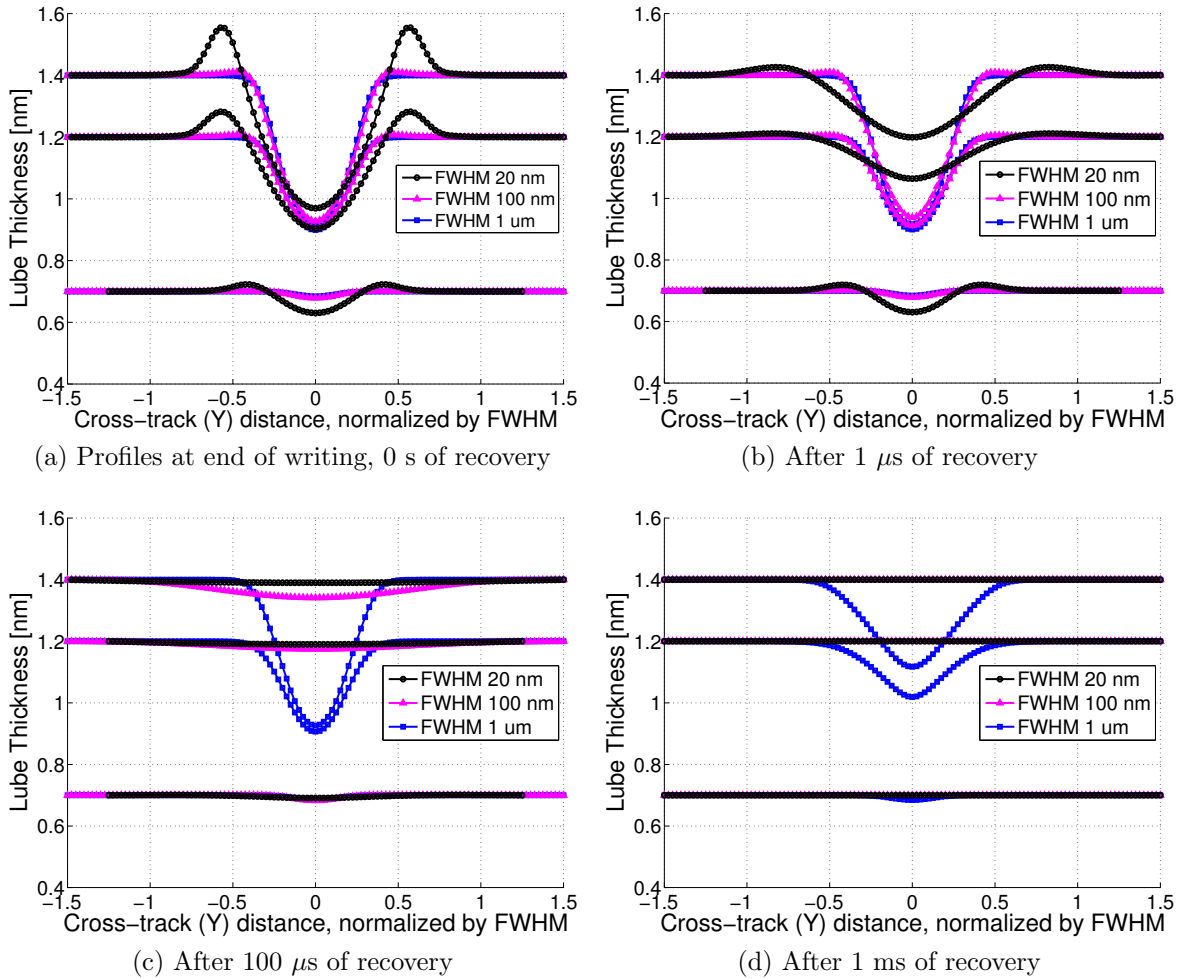


Figure 7.1: Cross-track profiles after specified amounts of recovery time for different initial thicknesses ($h_0 = 0.7, 1.2,$ and 1.4 nm) and thermal spot sizes used during HAMR writing (illumination time 2 ns, scanning speed 5 m/s, $T_{max} = 350^\circ\text{C}$). The cross-track coordinate is normalized by the thermal spot FWHM for direct comparison.

separated by length of time Δt :

$$\text{trough recovery rate at time step } n = \frac{h_{min}^n - h_{min}^{n-1}}{\Delta t}$$

A maximum exists for the thicker lubricants ($h_0 = 1.2, 1.4$ nm) because other sections of the lubricant profile, the side ridges or another location of the trough, initially have a faster recovery rate due to higher interface slope or higher curvature. After those features relax, the trough minimum point is the location of fastest recovery, which decreases monotonically in time. The global maximum recovery rate, that is $\min_{i,j}[(h_{i,j}^n - h_{i,j}^{n-1})/\Delta t]$, generally de-

creases in time (not shown). Like a linear spring restoring force that is proportional to the displacement ($F = -kx$), the restoring disjoining pressure and Laplace pressure forces decrease in magnitude as the lubricant relaxes toward a flat interface. Thus the global recovery rate decreases in time. For all thicknesses, the trough recovery rate of the smallest 20-nm FWHM spot case is an order of magnitude faster than the intermediate 100-nm FWHM case and three orders of magnitude faster than the 1- μm FWHM case. For all thermal spot sizes, the trough recovery rate for the 0.7-nm initial thickness is about three orders of magnitude slower than the thicker 1.2-nm and 1.4-nm cases. The tolerance of the algorithm is 10^{-9} , so rates below this value are effectively zero.

Some interesting trends are evident in Table 7.1 and Figures 7.1–7.2: smaller spots recover much faster and an optimal thickness for fastest recovery time exists for smaller spot sizes. Before offering an explanation for these trends, we first discuss the factors that determine lubricant recovery.

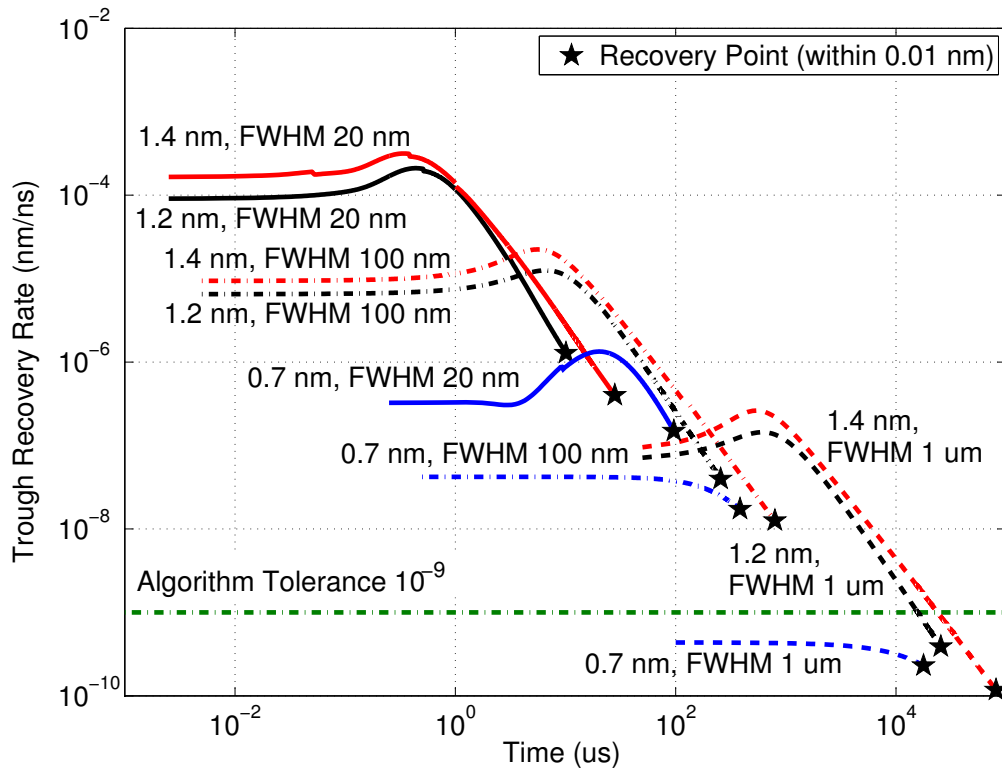


Figure 7.2: Trough recovery rate for various initial lubricant thicknesses and thermal spot sizes. A star indicates the time at which the lubricant recovers to within 0.01 nm of the original thickness. The algorithm tolerance is 10^{-9} . Laplace pressure, which has a minor effect on the lubricant profile, is ignored for 20-nm and 100-nm FWHM to expedite the computation time.

Determinants of Recovery: Driving Forces and Flow Resistance

According to our viscous lubricant model, the driving forces of lubricant recovery are the disjoining pressure and Laplace pressure gradients. Viscosity determines the level of resistance to flow; highly viscous liquids are difficult to drive into flow. Lubricant recovery time depends on the strength of the driving forces and the fluidity (reciprocal of viscosity), or how easily the lubricant flows; stronger driving forces and higher fluidity/lower resistance to flow lead to faster recovery times. Recasting the non-dimensional governing equation 5.18, we can group the terms according to contributions to ‘fluidity’ or as a ‘driving force’. Equation 7.1 is the basis of our explanations and interpretations of our simulations.

$$\frac{\partial h}{\partial t} = -\nabla \cdot \underbrace{\left[\underbrace{\frac{h^3}{\eta}}_{\text{Fluidity}} \overbrace{\nabla (\Pi + \nabla^2 h)}^{\text{Driving forces}} \right]}_{\text{Flow = Fluidity} \cdot \text{Driving forces}} \quad (7.1)$$

The driving forces depend on the shape of the lubricant-air interface profile such that severe interface profiles result in faster recovery times. Laplace pressure is a reflection of the mean curvature. The higher the curvature of the interface profiles, the larger the Laplace pressure force and consequently the faster the recovery rate driven by Laplace pressure. Disjoining pressure gradient can be decomposed with the chain rule: $\nabla \Pi = \Pi' \nabla h$ where $\Pi'(h)$ is an explicit function from [79]. Steeper lubricant distortion profiles lead to higher disjoining pressure driving forces and therefore faster recovery times due to the larger values of ∇h .

Laplace Pressure: A Minor Effect

The lubricant profile and recovery rate are not significantly different if Laplace pressure is excluded. Disjoining pressure is considered to be the main driver of lubricant recovery, and we therefore ignore Laplace pressure if its inclusion leads to very long computation times.

An example of the minor impact of Laplace pressure is illustrated in Figure 7.3, which shows the 20-nm FWHM, $h_0 = 1.2$ nm case simulation results up to 3 μ s of recovery with and without Laplace pressure. The impact of excluding the Laplace pressure is minimal as indicated by the minor differences in the trough and side ridge heights. The exclusion of Laplace pressure significantly reduces computation time. To determine the approximate recovery time to within 0.01 nm of the initial thickness, we exclude the Laplace pressure for several cases.

Trough recovery rate and recovery time are also very similar with and without the Laplace pressure. As an example, Figure 7.4 shows the practically identical trough recovery rate and recovery time to within 0.01 nm of h_0 for the 1- μ m FWHM, $h_0 = 1.4$ nm case. The recovery time is 81.1 ms with Laplace pressure and 82.2 ms without Laplace pressure.

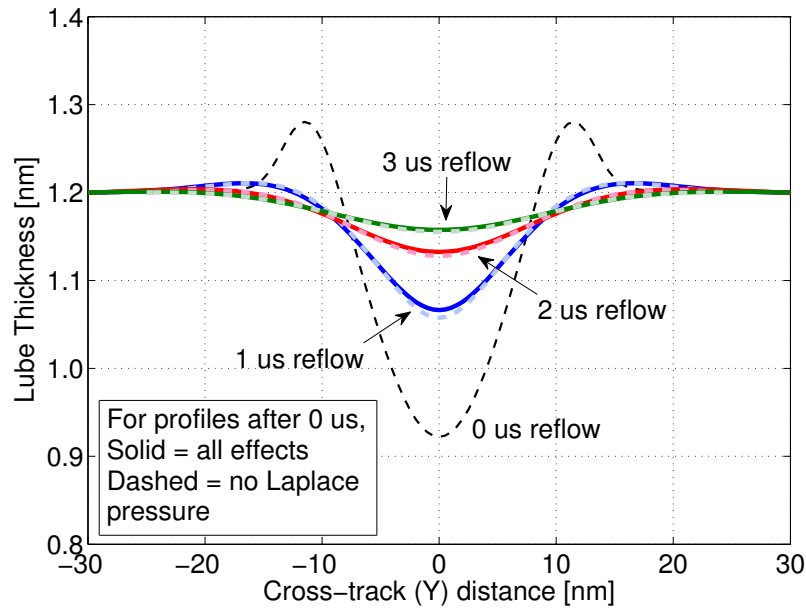


Figure 7.3: Cross-track lubricant profiles for 20-nm FWHM and 1.2-nm initial thickness with and without Laplace pressure.

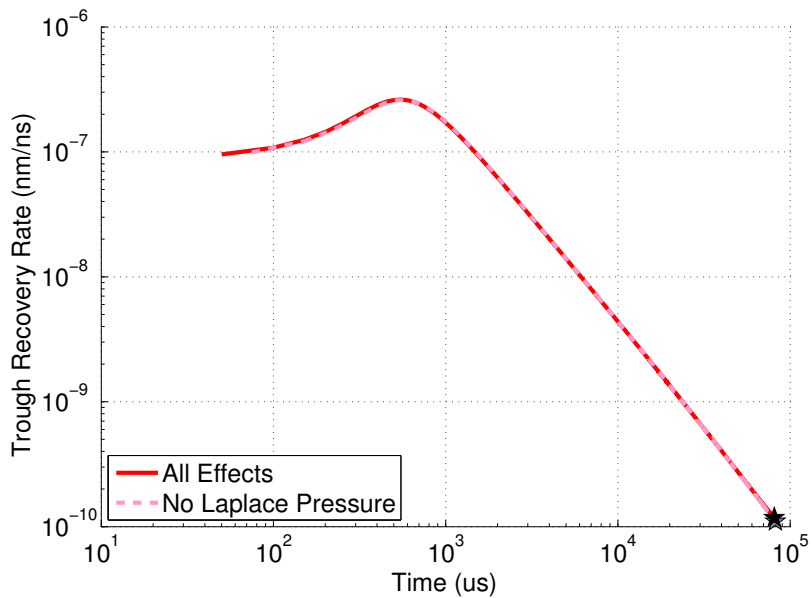


Figure 7.4: Lubricant trough recovery rates for 1- μm FWHM and 1.4-nm initial thickness with and without Laplace pressure.

HAMR Lubricant Recovery Trends

Small spots recover faster During writing, we found that large temperature gradients from small laser spots removed more lubricant from the laser path compared to large laser spots because thermocapillary shear stress formed side ridges. The recovery simulations show that these side ridges add to lubricant deformation and result in faster recovery times. Small spots recover faster because the driving disjoining pressure gradient is much higher due to the sharper profile shape induced by HAMR writing, i.e. ∇h is larger. Inspecting the initial cross-track profiles from Figure 7.1a, we see that all three thermal spots have comparable depths in physical units (nm) and comparable trough widths in the FWHM normalized cross-track coordinates for the thicker lubricants of 1.2 nm and 1.4 nm. In other words, Δh is similar but Δy varies proportionally with thermal spot size. The resulting profile shape that determines the recovery rate, $\frac{\Delta h}{\Delta y}$, is therefore inversely proportional to the thermal spot FWHM. The profile shape $\frac{\Delta h}{\Delta y}$ for the 20-nm FWHM case is initially roughly 5 times larger than for the 100-nm FWHM case and approximately 50 times larger than for the 1- μm FWHM case. One may expect the initial recovery rate for the 20-nm FWHM case to therefore be approximately 5 and 50 times faster than the 100-nm and 1- μm FWHM cases, respectively. As shown in Figure 7.2, the initial trough recovery rate for 20-nm FWHM is at least 10 times faster than for 100-nm FWHM at the same initial thickness and at least 1000 times faster than for 1- μm FWHM. The interaction of interdependent terms in the non-linear governing equation and the lubricant profile evolution also influence the recovery rate so that recovery rate comparisons cannot be made solely from deformed interface profile comparisons.

Thin films recover slower The recovery rate is slower for 0.7-nm initial thickness lubricant systems because the viscosity increases drastically as the lubricant approaches 0.6-nm thickness (Figure 5.3). In addition, the smaller amount of lubricant deformation for thin systems leads to a smaller ∇h and therefore smaller $\nabla \Pi$ recovery driving force. The high flow resistance (or lower fluidity) and small driving force for the thin lubricants result in slower recovery rates compared to thicker lubricants.

Small spots exhibit an optimal thickness for recovery The amount of recovery needed after HAMR writing can be quantified by performing a discretized integration of the deformation profile. The amount of lubricant above the initial thickness h_0 is accumulation and the amount below h_0 is depletion. The total volume of accumulation and depletion $\Delta h \Delta x \Delta y$ can be normalized for direct comparison of different thermal spot sizes: Δh retains physical units of nanometers and the lateral dimensions $\Delta x, \Delta y$ are normalized by the thermal spot FWHM. The volume to recover following HAMR writing along a cross-sectional slice of width 3-FWHM and the recovery time are plotted in Figure 7.5. One would expect that as the volume of lubricant depleted and accumulated during HAMR writing increases with increasing lubricant thickness, the time to recover would increase. However, this is a highly non-linear problem with driving forces and fluidity that depend on the solution $h(x, y, t)$. For smaller laser spot systems, the higher ∇h translates to higher restoring $\nabla \Pi$ force that has its fastest recovery rate in a middle thickness range where the lubricant is not too thin

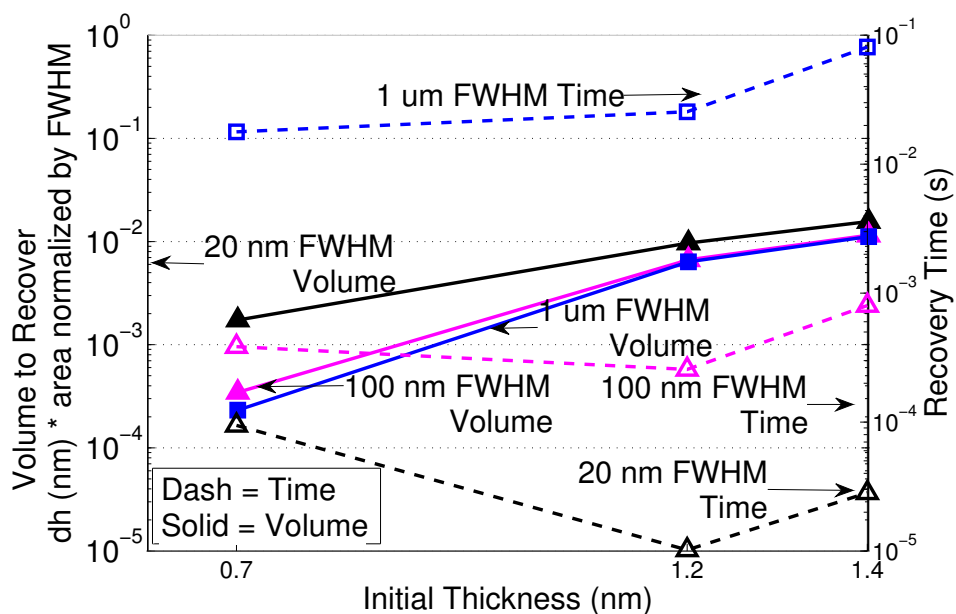


Figure 7.5: Normalized volume to recover following HAMR writing and recovery time to within 0.01 nm of the initial thickness for different thicknesses and thermal spot sizes. The volume to recover is from a cross-sectional slice $3 \cdot \text{FWHM}$ in width.

to have high viscosity but not too thick so that there is considerable lubricant depletion and accumulation that needs to be recovered. This optimal point becomes more pronounced as the thermal spot size decreases.

Maximum Temperature Study

We have shown that smaller thermal spots recover faster compared to larger spots and argued this is in part due to their "more severe" lubricant deformation. However, the severity of the lubricant depletion can be so catastrophic that the lubricant cannot recover. Table 7.2 lists the recovery times to within 0.01 nm of the initial 1.2-nm thickness for each maximum temperature. The recoveries of four thermal spot maximum temperature cases are plotted up to $4 \mu\text{s}$ in Figure 7.6. The lower temperature cases recover easily and smoothly from their relatively mild deformations. The 450°C case demonstrates little trough movement after $1 \mu\text{s}$ but then recovers after this initial resistance. The trough minimum point snaps up once a cone-shaped interface induces a large enough disjoining pressure force between 1 and $4 \mu\text{s}$ of recovery time (not shown), and the system is able to recover to a flat interface. The trough for the 600°C case does not move in the $4 \mu\text{s}$ depicted in Figure 7.6 or in the next $20 \mu\text{s}$ of simulated recovery. We assume that a crater with vertical sidewalls would remain indefinitely. The difficult recovery behavior after high HAMR writing temperatures is due

to high viscosity at the trough minimum thicknesses of 0.4 nm and below.

Table 7.2: Recovery time to within 0.01 nm of initial thickness for various thermal spot maximum temperatures achieved during HAMR writing. Laplace pressure is neglected to speed up the computation time.

T_{max}	Recovery time
150°C	0.264 μ s
300°C	4.73 μ s
450°C	34.4 μ s
600°C	never

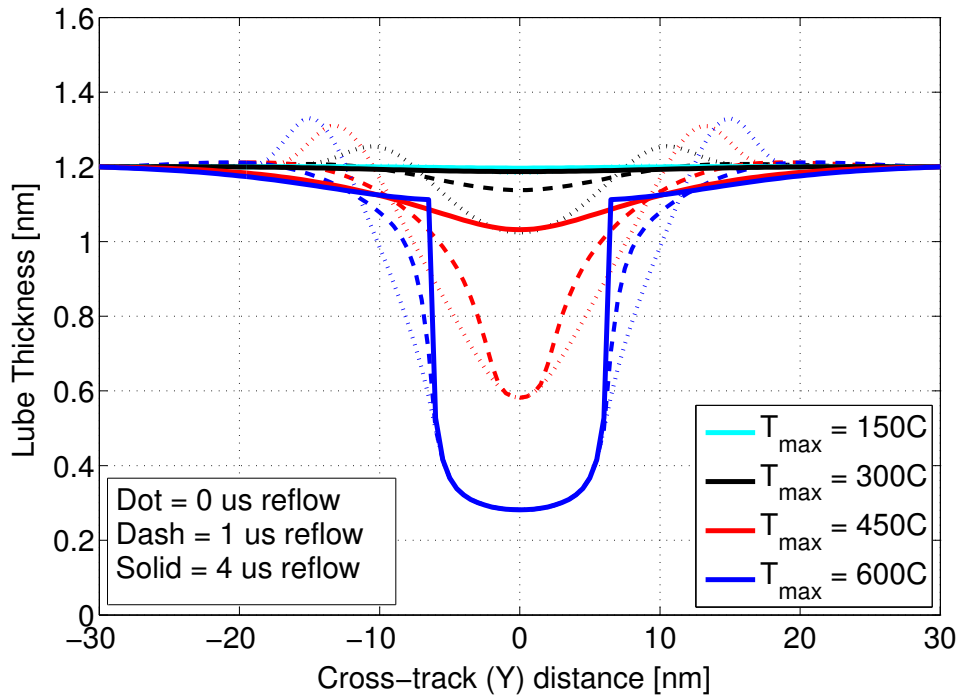


Figure 7.6: Cross-track lubricant profiles for different maximum temperature achieved during writing with a 20-nm FWHM. Initial (0 s of recovery, immediately after writing) and recovery after 1 μ s are shown for each T_{max} case. All effects, including Laplace pressure, are considered. $h_0 = 1.2$ nm, 20-nm FWHM case.

7.3 Discussion

We have shown that several Angstroms of lubricant deformation due to 2 ns pulse of a sub-100-nm FWHM thermal spots recover to within 0.01 nm after less than 1 ms. This indicates that the lubricant is well recovered by the second laser pass on a single track under these conditions. Seemingly in contrast, experiments cited in the Section 7.1 demonstrate PFPE lubricants require several hours to recover from laser-induced deformation [99, 100]. However, the severity of the trough profile in [99, 100] is relatively mild, roughly 25 μm in width as measured from the top of the side ridges and 0.5–0.1 nm in peak-to-peak variation, leading to a slow recovery process. The driving force magnitude is about 1/1250 of the same peak-to-peak variation due to a 20-nm FWHM thermal spot. In addition, Ztetraol is the lubricant tested in [99, 100]; the extra two hydroxyl end-groups per molecule increases the interaction with the carbon overcoat, increasing the viscosity and decreasing recovery time.

These recovery studies are for Zdol 2000, a common lubricant in hard drives a decade ago. Modern lubricants such as Ztetraol and ZTMD have more functional end-groups that interact more strongly with the carbon overcoat [21, 116]; therefore the disjoining pressure, viscosity, surface tension, and evaporation (during HAMR writing) models should be different from Zdol property models. Stronger lubricant-carbon overcoat interactions imply that it is more difficult to move and evaporate the lubricant, so the amount of deformation due to thermal spot scanning is expected to be less for a lubricant such as Ztetraol in comparison with the simulation results we present here for Zdol 2000. For future HAMR lubricant writing and recovery studies, we look to add the capability to simulate other lubricant types by incorporating disjoining pressure models for Ztetraol and ZTMD based on experimental studies [21, 109]. Suitable experimental data must also be found for the vaporization energy variation with molecular weight for Ztetraol and ZTMD; we expect the vaporization energy will increase linearly with molecular weight as with Zdol, but the constants will differ. In addition, flow activation energy and entropy are properties needed for the viscosity model.

While experimental data for Zdol 2000 under laser illumination is published, validation of our recovery simulation tool is not feasible at this time because the lubricant profiles at two specified time points are not given. The simulation tool requires an initial profile of Zdol 2000 measured at a specified time as an input, and another profile measured at a later time is required for the comparison between simulation results and experimental observation. In the literature we have only found such plots for Ztetraol [100].

Because we model the lubricant as a viscous fluid, lubricant recovery occurs more slowly and at a steadier rate than what we expect for actual hard drive lubricants that are known to exhibit some viscoelastic behavior. In response to a suddenly applied loading state, such as a sudden application of interface restoring forces upon rapid cooling of the substrate to ambient temperature, a Newtonian viscous fluid responds by a flow process toward equilibrium (flat interface). The rate of recovery depends on the fluid's viscosity. A viscoelastic material would be expected to respond with an instantaneous deformation (elastic, solid-like response) followed by a flow process which may or may not be limited in magnitude as time increases (viscous, fluid-like response) [117]. For future HAMR lubricant simulation studies, we plan to

modify our simulation tool to include a viscoelastic constitutive model. We expect that with the inclusion of viscoelastic effects, there will be a rapid elastic response to the restoring forces followed by a slower flow process. The recovery time may or may not decrease, depending on the nature of the fluid-like response.

Though not a direct comparison to our viscous fluid recovery simulations, bulk Zdol relaxation times derived from oscillatory shear experiments are another indicator of Zdol's ability to recover from a displacement disturbance. The relaxation times listed in Table 22.3 in [20] are a measure of the time needed for the stress to relax in the lubricant after it has been subjected to a constant strain and are derived under the assumption that the lubricant behaves as a linear viscoelastic fluid. The times listed in Table 7.1 are a measure of how long it takes the lubricant modeled as a viscous fluid to recover from a trough to a nearly flat interface. The bulk relaxation time for Zdol 2500 is 5.03×10^4 s and for the different batches of Zdol 4000 range from 2.40×10^3 to 2.10×10^8 s [20]. These relaxation times are much longer than the time needed for the interface to recover from depletion caused by a scanning thermal spot that is on the order of microseconds or milliseconds (Table 7.1). Possible reasons for this discrepancy in magnitude include the fundamental difference in material models (viscous fluid vs. linear viscoelastic fluid) and different relaxation behavior of thin-film lubricant from the bulk material. The discrepancy may also be an indicator that modeling Zdol as a viscous fluid is not appropriate. It would be interesting to compare our results with the relaxation times in [20] once the viscoelastic constitutive model is implemented into our lubricant simulation tool.

Our model does not account for thermally initiated chemical changes such as cross-linking, cleavage of molecules, or altered nature of the interactions with the carbon overcoat due to changes in the lubricant or the overcoat. Thermal decomposition of bulk Fomblin Zdol occurs at temperatures above 350°C [22, 23], so our high temperature simulations in Section 7.2 should not be interpreted as a quantitative analysis. Those effects are also left to the subject of another lubricant study.

We have used a dispersive disjoining pressure component that behaves as $\frac{1}{h^3}$ in employing the model proposed by Karis and Tyndall [79] for Zdol; however, a more physical model that introduces a distance of closest approach, d_0 , so that $\Pi^d \sim \frac{1}{(h+d_0)^3}$ remains bounded as $h \rightarrow 0$ [118]. In [118], d_0 is chosen to be the sum of the van der Waals radii for carbon and fluorine atoms that make up the backbone of non-functional PFPE lubricant studied in that paper. By using $\Pi^d \sim \frac{1}{h^3}$, we are predicting a larger dispersive disjoining pressure derivative $(\Pi^d)'$, the disjoining pressure term present in the governing Equation 5.18 at a given thickness, compared to the derivative predicted by the distance of closest approach form. The disparity between $(\Pi^d)'$ for the two models increases with decreasing film thickness. For lubricant thicknesses $h > 0.63$ nm such as all the thickness profiles shown in Figure 7.1, we over-predict $(\Pi^d)'$ by a factor of 7.1 or less. The smallest thickness predicted from our simulations is 0.28 nm, achieved after illumination by $T_{max} = 600^\circ\text{C}$; at this thickness the $\Pi^d \sim \frac{1}{h^3}$ model predicts a $(\Pi^d)'$ that is 35 times greater than the closest approach model derivative. However, the thin-film viscosity model results in such a large viscosity that it appears impossible to

remove the final 0.28 nm of lubricant with the specified thermal spot, effectively resulting in a distance of closest approach. So even though we use a Π^d model that is unbounded as $h \rightarrow 0$, the thin-film viscosity will prevent the lubricant from achieving zero film thickness. Thus we have qualitatively similar results as if we had used the distance of closest approach model for dispersive disjoining pressure.

The constitutive laws of continuum mechanics will eventually break down when the characteristic dimensions are small enough so that the discrete nature of individual polymer molecules is important. For the 1–2-nm thick lubricant subject to nanosecond-scale laser illumination, molecular dynamics (MD) simulation may be more accurate. MD simulations solve the equations of motion (Newton’s second law) for each particle subject to assumed intra- and intermolecular potentials and force fields. Smith et al. [119] recently published MD simulation results for steady and transient heating of bulk and thin-film Zdol. However, there are also assumptions implicit in MD simulations; so just as simulations of continua are only as good as the constitutive law, MD simulations are only as good as the assumed potentials and force fields.

7.4 Conclusion

Interesting and non-obvious results for small HAMR thermal writing spots are predicted by our lubricant recovery simulations. Small thermal spot sizes needed to achieve 5 Tb/in² recover on the order to 100–1000 times faster than deformations due to micron-sized optical spots. There appears to be an optimal thickness at which small thermal spot deformations recover fastest, a thickness that is not too thin to have high resistance but not too thick so that substantial lubricant depletion and accumulation needs to be recovered. HAMR lubricant experiments usually are scaled up so that observations can be made using current optical measurement techniques. However, our simulations show that simple scaling of experimental observations using optical laser spots of diameters close to 1 μm to predict phenomena induced by thermal spots close to 20-nm FWHM may not be valid. Researchers should be aware of the possibility of different lubricant behavior at small scales when designing and developing the HAMR HDI.

This chapter presents work published in Tribology Letters [120].

Chapter 8

Conclusion and Future Work

8.1 Conclusion

The hard disk drive industry is approaching the storage density limit of traditional magnetic recording technology. A fundamentally new technology is needed to decrease magnetic recording bit sizes below the superparamagnetic limit to achieve industry storage density targets of 1–10 Tb/in². Heat assisted magnetic recording is positioned to be the next technology employed in HDD products that drastically increases storage density. However, thermal issues such as high temperature gradients on the disk and a heat-dissipating laser delivery system integrated into the slider body add to the already challenging mechanical problem of maintaining reliable head-disk spacings of less than 5 nm; the industry projects that the slider’s flying height will be only 1.1 nm in 4 Tb/in² HDDs [12]. This dissertation investigates through numerical simulation how two components of the head-disk interface, the air bearing and the lubricant coating the disk, are affected by the new thermal effects introduced by HAMR.

The models for the air bearing and lubricant are both derived from lubrication theory as described in Chapter 2. The lubricant is modeled as an incompressible Newtonian fluid. As a first step in modeling HAMR lubricant behavior, we develop a lubricant model based on the conventional HDD lubricant Zdol for which there exists much published experimental data and theoretical analysis. The air bearing is treated as an ideal gas, and the sophisticated slip-correction coefficients proposed by Fukui and Kaneko [18] are used. The assumptions and limitations of the lubricant and air bearing models are also discussed.

The iterative static air bearing solver used to evaluate the slider’s flying attitude and thermal protrusion due to heat-dissipating elements is described in Chapter 3. The air bearing solution and slider body electro-thermo-mechanical solution depend on each other through heat transfer and pressure boundary conditions at the air bearing surface. Three major changes are made to the isothermal version of the air bearing solver CMLAir to create a non-isothermal version appropriate for HAMR conditions, CMLAir-HAMR: the implementation of the general MGL equation, the capability to input an ABS temperature

profile used to estimate the local air bearing temperature, and the addition of a thermal creep flow rate database.

Static slider air bearing simulations performed on a simplified HAMR slider of our own design are presented in Chapter 4. The smallest stable flying height determines the areal recording density and the efficiency of the NFT, so we concentrate our flying height studies at the slider's trailing edge region that contains the read and write transducers and the NFT. The heat dissipating elements in the slider are the TFC heater, the laser diode, and the NFT. We investigate the impact of each component of the HAMR slider on the slider thermal deformation, which has a significant influence on the minimum flying height. The NFT heat dissipation induces localized protrusion and high temperatures, making it the minimum flying height location and the peak ABS temperature location. The Ta_2O_5 waveguide dissipates heat away from the NFT, thereby lowering the maximum ABS temperature and smoothing the NFT localized protrusion. For our particular slider design, the laser diode does not appreciably affect the slider protrusion or flying attitude. The air bearing model options for heat transfer model, thermal creep, and the MGL governing equation are tested. Thermal creep could be an important factor to investigate further; for minimum flying heights less than 2 nm, the flying height is 0.05–0.15 nm lower when thermal creep is included. If a stable 1-nm flying height can be realized, the enhanced cooling of the ABS near the minimum flying height location at the NFT could be used to control the temperature rise of the NFT.

Details of the lubricant model are provided in Chapter 5. The effects of functionalized end-groups on disjoining pressure and thin-film viscosity are considered. The viscosity and disjoining pressure models come from previously published investigations of Zdol [79, 84]. Two different non-dimensionalization schemes are used for HAMR writing and lubricant recovery conditions according to the effects driving lubricant flow in each system: thermocapillary shear stress and evaporation for HAMR writing and surface tension and disjoining pressure for lubricant recovery.

Lubricant deformation simulation studies during HAMR writing are undertaken in Chapter 6. The lubricant is a critical component of the HDI that protects the disk and recording head from damage during intermittent contact; the HAMR lubricant must be able to withstand the writing process. Total disjoining pressure suppresses lubricant removal and flow compared with models that consider only the van der Waals force contribution to disjoining pressure, though the degree of this mitigation depends on the lubricant thickness. For thicknesses below 1 nm, the orders of magnitude lower evaporation rates and higher viscosities lead to little deformation compared with thicker lubricants. Ignoring the thickness dependence of viscosity for lubricants less than 1 nm thick results in unrealistically large lubricant deformation. No significant lubricant deformation is predicted for temperatures below 150°C for a 2-ns thermal spot illumination. The most significant finding is the dependence of lubricant deformation characteristics on thermal spot size. For larger thermal spot size above 100-nm FWHM, the resulting thermocapillary shear stress is too weak to pull the lubricant into side ridges for the $T_{max} = 350^\circ\text{C}$ cases studied, and the resulting trough is mainly due to evaporation. This is in contrast to the smaller thermal spots with the higher temperature gradients for which thermocapillary shear stress is the main driver of lubricant

deformation, pulling lubricant away from the thermal spot center to the side ridges, while evaporation is not as important.

Lubricant recovery simulations following HAMR writing are presented in Chapter 7. The interesting and non-obvious results for small vs. large thermal spot sizes continue into the lubricant recovery phase. Small 20-nm FWHM thermal spots recover 100–1000 times faster than micron-sized thermal spots due to higher lubricant-air interface curvature and gradients that determine the driving forces of disjoining pressure and Laplace pressure gradients. Unlike larger thermal spots, sub-100-nm FWHM thermal spots appear to have an optical thickness for fastest recovery time to a flat interface. Our simulation studies of the lubricant under HAMR conditions indicate that simple scaling of several published experimental observations that use optical laser spots of diameters close to 1 μm may not be valid to predict phenomena induced by thermal spots close to 20-nm FWHM.

8.2 Future Work

Though not presented in this dissertation, we did modify the governing equation of the CMLAir dynamic solver to allow for air temperature variation. The ABS protrusion and temperature profiles determined by the iterative static solver serve as realistic and accurate starting base cases to be interpolated for the dynamic simulation. The dynamic solver can be used to predict flying height variations or instabilities that will occur at small physical spacings under HAMR conditions and determine the sources of these phenomena. Finite element simulations presumably based on continuum theory indicate that the peak temperature and protrusion time constants of the NFT are quite different: 1–2 ms for peak NFT protrusion and 2–3 μs for peak NFT temperature [60]. The ABS time-varying protrusion and temperature profiles that are prescribed in dynamic solver input files should be based on the most accurate thermo-mechanical HAMR slider modeling available and allow for different variation of ABS protrusion and temperature.

Conduction is the only mode of heat transfer at the ABS considered by the iterative static solver. However, for near-zero flying height HAMR systems with large ABS and disk temperature gradients at the minimum flying height location, viscous dissipation may be comparable to heat conduction.

Both the lubricant and air bearing simulations are simplified by mostly neglecting the roughness inherent to all disk and slider surfaces. For the air bearing simulations in this dissertation, the slider surface is presumed to be smooth and disk roughness is included only with a statistical approximation. Disk and slider roughness (surface features with wavelengths up to a few microns) and disk waviness (surface features with wavelengths on the order of a few microns to a few millimeters) are already incorporated into the dynamic simulator, and these simulation capabilities should be included in future dynamic HAMR air bearing studies. In this work, the lubricant is assumed to be bounded by a perfectly flat substrate. However, current production disks have a root-mean-square roughness around 0.34 nm according to AFM measurements [32, 33]. Disk roughness likely affects how the lubricant

interacts with the carbon overcoat and therefore affects lubricant properties. However, if the lubricant property models are based on thin-film experiments on real disks, the effects of disk roughness on lubricant properties may be sufficiently incorporated. Larger-scale disk waviness may be an issue for lubricant flow.

The next likely step for the lubricant model is to implement a viscoelastic constitutive equation to replace the current viscous fluid model. The mechanical properties of polymers such as the PFPE lubricants used in HDDs demonstrate some viscoelastic phenomena. The complicated molecular-level contortions of each flexible threadlike polymer chain that underlie macroscopic mechanical deformation of the lubricant are likely better predicted by a viscoelastic fluid model than an idealized viscous fluid model. A place to start may be the linear viscoelastic Maxwell element coefficients obtained from oscillatory shear measurements reported in [20].

Intermolecular forces depend on the lubricants molecular weight, coverage of the disk, and the lubricant-carbon overcoat binding interactions. Currently, intermolecular forces are modeled in our air bearing simulation using a simple Lennard-Jones 6-12 potential with two parameters that remain constant for the duration of the simulation. With this method, intermolecular forces only vary according to local physical clearance between the slider and the disk. With our lubricant code, we can determine how the lubricant coverage and optical properties and hence intermolecular force parameters vary over the disk surface during and after HAMR writing. There is potential to consider more sophisticated steric effects due to overlapping and oriented polymer molecules by using a more complicated interaction potential. The air bearing simulation results provide air bearing pressure and shear stress boundary conditions for detailed lubricant simulations. In summary, the air bearing simulation tool could provide better boundary conditions for the lubricant simulation tool, and vice versa.

Bibliography

- [1] IBM. (). IBM 350 disk storage unit, [Online]. Available: http://www-03.ibm.com/ibm/history/exhibits/storage/storage_350.html (Retrieved Jul. 15, 2013).
- [2] Seagate Technology, *Laptop SSHD Laptop Thin SSHD Data Sheet*, 2013.
- [3] J.-J. Maleval. (March 28, 2013). HISTORY: List of 221 Companies in HDD Manufacturing Since 1956, [Online]. Available: <http://www.storagenewsletter.com/news/disk/217-companies-hdd-since-1956> (Retrieved Jul. 15, 2013).
- [4] E. Savitz, “Seagate CEO Luczo On Drives, Zettabytes, Flash And His Tattoo,” *Forbes*, April 12, 2012. [Online]. Available: www.forbes.com/sites/ericsavitz/2012/04/12/seagate-ceo-luczo-on-drives-zettabytes-flash-and-his-tattoo (Retrieved Jul. 15, 2013).
- [5] International Data Corporation, *THE DIGITAL UNIVERSE IN 2020 Executive Summary: Big Data, Bigger Digital Shadows, and Biggest Growth in the Far East*, <http://www.emc.com/collateral/analyst-reports/idc-the-digital-universe-in-2020.pdf>, 2012.
- [6] Seagate Technology. (January 28, 2013). Seagate And Virident Join Forces To Deliver Solutions For The Enterprise Flash Storage Market [Press release], [Online]. Available: <http://www.seagate.com/about/newsroom/press-releases/seagate-virident-join-forces-pr-master/> (Retrieved Jul. 15, 2013).
- [7] HGST. (Jun. 24, 2013). Western Digital To Strategically Expand Its Position in Enterprise Solid State Storage with the Acquisition of sTec, Inc.; Company to be Fully Integrated in HGST [Press release], [Online]. Available: <http://www.hgst.com/press-room/2013/western-digital-to-strategically-expand-its-position-in-enterprise-solid-state-storage-with-the-acquisition-of-stec-inc-company-to-be-fully-integrated-into-hgst> (Retrieved Jul. 15, 2013).
- [8] T. Coughlin and E. Grochowski, *Years of Destiny: HDD Capital Spending and Technology Developments from 2012–2016*, IEEE Santa Clara Valley Magnetics Society Meeting, Jun. 19, 2012. [Online]. Available: http://ewh.ieee.org/r6/scv/mag/MtgSum/Meeting2012_06_Presentation.pdf (Retrieved Jul. 15, 2013).
- [9] D. W. Meyer, P. E. Kupinski, and J. C. Liu, “Slider with temperature responsive transducer positioning,” US Patent 5 991 113, Nov. 23, 1999.

- [10] R. L. Wallace, "The reproduction of magnetically recorded signals," *Bell System Technical Journal*, vol. 30, pp. 1145–1173, 1951.
- [11] P.-L. Lu and S. H. Charap, "Magnetic Viscosity in High-Density Recording," *Journal of Applied Physics*, vol. 75, no. 10, pp. 5768–5770, 1994.
- [12] "International Technical Roadmap: Magnetic Data Storage - the technology of magnetic hard disk drives (HDDs)," IDEMA Advanced Storage Technology Committee (ASTC), Tech. Rep., 2013.
- [13] W. Challener, C. Peng, A. Itagi, D. Karns, W. Peng, Y. Peng, X. Yang, X. Zhu, N. Gokemeijer, Y.-T. Hsia, G. Ju, R. Rottmayer, and M. Seigler, "Heat-assisted magnetic recording by a near-field transducer with efficient optical energy transfer," *Nature Photonics*, vol. 3, pp. 220–224, 2009.
- [14] B. C. Stipe, T. C. Strand, C. C. Poon, H. Balamane, T. D. Boone, J. A. Katine, J.-L. Li, V. Rawat, H. Nemoto, A. Hirosune, O. Hellwig, R. Ruiz, E. Dobisz, D. S. Kercher, N. Robertson, T. R. Albrecht, and B. D. Terris, "Magnetic recording at 1.5 Pb m⁻² using an integrated plasmonic antenna," *Nature Photonics*, vol. 4, no. 7, pp. 484–488, 2010.
- [15] M. Seigler, W. A. Challener, E. Gage, N. Gokemeijer, G. Ju, B. Lu, K. Pelhos, C. Peng, R. Rottmayer, and X. Yang, "Integrated heat assisted magnetic recording head: Design and recording demonstration," *IEEE Transactions on Magnetics*, vol. 44, no. 1, pp. 119–124, 2008.
- [16] B. Xu, C. W. Chia, Q. Zhang, Y. T. Toh, C. An, and G. Vienne, "Thermal Analysis of Heat-Assisted Magnetic Recording Optical Head with Laser Diode on Slider," *Japanese Journal of Applied Physics*, vol. 50, no. 9, 09MA05, Sep. 2011.
- [17] O. Reynolds, "On the Theory of Lubrication and Its Application to Mr. Beauchamp Tower's Experiments, Including an Experimental Determination of the Viscosity of Olive Oil," *Philosophical Transactions of the Royal Society of London*, vol. 177, pp. 157–234, 1886.
- [18] S. Fukui and R. Kaneko, "Analysis of ultra-thin gas film lubrication based on linearized Boltzmann equation: First report derivation of a generalized lubrication equation including thermal creep flow," *ASME Journal of Tribology*, vol. 110, pp. 253–262, 1988.
- [19] N. Shukla, A. J. Gellman, and J. Gui, "The Interaction of CF₃CH₂OH and (CF₃)₂CO with Amorphous Carbon Films," *Langmuir*, vol. 16, no. 16, pp. 6562–6568, 2000.
- [20] T. Karis, "Lubricants for the Disk Drive Industry," in *Lubricant Additives: Chemistry and Applications*, L. Rudnick, Ed., CRC Press, 2009, ch. 22, pp. 523–584.
- [21] X.-C. Guo, B. Knigge, B. Marchon, R. J. Waltman, M. Carter, and J. Burns, "Multidentate functionalized lubricant for ultralow head/disk spacing in a disk drive," *Journal of Applied Physics*, vol. 100, p. 044306, 2006.

- [22] R. Lei, A. Gellman, and P Jones, "Thermal stability of Fomblin Z and Fomblin Zdol thin films on amorphous hydrogenated carbon," *Tribology Letters*, vol. 11, no. 1, pp. 1–5, 2001.
- [23] L Li, P. Jones, and Y.-T. Hsia, "Effect of chemical structure and molecular weight on high-temperature stability of some Fomblin Z-type lubricants," *Tribology Letters*, vol. 16, no. 1-2, pp. 21–27, 2004.
- [24] G. W. Tyndall and R. J. Waltman, "Thermodynamics of confined perfluoropolyether films on amorphous carbon surfaces determined from the time-dependent evaporation kinetics," *The Journal of Physical Chemistry B*, vol. 104, no. 30, pp. 7085–7095, 2000.
- [25] M Stirniman, S. Falcone, and B Marchon, "Volatility of perfluoropolyether lubricants measured by thermogravimetric analysis," *Tribology Letters*, vol. 6, pp. 199–205, 1999.
- [26] C. Mate and B Marchon, "Shear response of molecularly thin liquid films to an applied air stress," *Physical Review Letters*, vol. 85, no. 18, pp. 3902–3905, 2000.
- [27] M. Scarpulla, C. Mate, and M. Carter, "Air shear driven flow of thin perfluoropolyether polymer films," *Journal of Chemical Physics*, vol. 118, no. 7, pp. 3368–3375, 2003.
- [28] B Marchon and Y Saito, "Lubricant Thermodiffusion in Heat Assisted Magnetic Recording," *IEEE Transactions on Magnetics*, vol. 48, no. 11, pp. 4471–4474, 2012.
- [29] D Dowson, "A generalized Reynolds equation for fluid-film lubrication," *International Journal of Mechanical Sciences*, vol. 4, pp. 159–170, 1962.
- [30] W. Gross, L. Matsch, V. Castelli, A. Eshel, J. Vohr, and M. Wildmann, *Fluid Film Lubrication*. New York: John Wiley & Sons, Inc., 1980.
- [31] A. Oron, S Davis, and S Bankoff, "Long-scale evolution of thin liquid films," *Reviews of Modern Physics*, vol. 69, no. 3, pp. 931–980, 1997.
- [32] A. I. Vakis, S.-C. Lee, and A. A. Polycarpou, "Dynamic Head-Disk Interface Instabilities With Friction for Light Contact (Surfing) Recording," *IEEE Transactions on Magnetics*, vol. 45, no. 11, pp. 4966–4971, 2009.
- [33] A. I. Vakis and A. A. Polycarpou, "Head-disk interface nanotribology for Tbit/inch² recording densities: near-contact and contact recording," *Journal of Physics D: Applied Physics*, vol. 43, no. 22, p. 225 301, 2010.
- [34] S. A. Schaaf and P. L. Chambre, *Flow of Rarefied Gases*. Princeton University Press, 1961.
- [35] G. Karniadakis, A. Beskok, and N. Aluru, *Microflows and Nanoflows: Fundamentals and Simulation*. New York: Springer Science+Business Media, Inc., 2005.
- [36] A. Burgdorfer, "Thermal Management in Heat-Assisted Magnetic Recording," *ASME Journal of Basic Engineering*, vol. 81, pp. 94–100, 1959.
- [37] Y. T. Hsia and G. A. Domoto, "An Experimental Investigation of Molecular Rarefaction Effects in Gas Lubricated Bearings at Ultra-Low Clearances," *Journal of Lubrication Technology*, vol. 105, no. 1, pp. 120–129, 1983.

- [38] S. Fukui and R. Kaneko, "Molecular Gas Film Lubrication (MGL)," in *Handbook of MicroNano Tribology*, B. Bhushan, Ed., 1st, CRC Press Inc., 1995, ch. 13, pp. 559–604.
- [39] C. Cercignani, *The Boltzmann Equation and Its Applications*. New York: Springer-Verlag, 1988.
- [40] Y. Sone, *Molecular Gas Dynamics: Theory, Techniques, and Applications*. Boston: Birkhäuser, 2006.
- [41] C Cercignani, M Lampis, and S Lorenzani, "Flow of a rarefied gas between parallel and almost parallel plates," in *Proceedings of 24th International Symposium on Rarefied Gas Dynamics*, American Institute of Physics, vol. 762, Melville, NY: AIP Conference Proceedings, 2005, pp. 719–724.
- [42] S Loyalka, "Thermal transpiration in a cylindrical tube," *Physics of Fluids*, vol. 12, no. 11, pp. 2301–2305, 1969.
- [43] F Alexander, A. Garcia, and B. J. Alder, "Direct simulation Monte Carlo for thinfilm bearings," *Physics of Fluids*, vol. 6, no. 12, pp. 3854–3860, 1994.
- [44] W Huang, D. Bogy, and A. Garcia, "Three-dimensional direct simulation monte carlo method for slider air bearings," *Physics of Fluids*, vol. 9, no. 6, pp. 1764–1769, 1997.
- [45] S. Lu, "Numerical Simulation of Slider Air Bearings," PhD thesis, University of California, Berkeley, 1997.
- [46] B. Cox and D. B. Bogy, *The CML Air Bearing Design Program (CMLAir), Version 7 User Manual*, 2007.
- [47] S. Patankar, *Numerical Heat Transfer and Fluid Flow*. New York: Hemisphere Publishing Corporation, 1980.
- [48] E. Cha and D. B. Bogy, "A Numerical Scheme for Static and Dynamic Simulation of Subambient Pressure Shaped Rail Sliders," *ASME Journal of Tribology*, vol. 117, pp. 36–46, 1995.
- [49] N. Liu, "Application of Rarefied Gas Dynamics to the Head-Disk Interface in Hard Disk Drives," PhD thesis, University of California, Berkeley, 2010.
- [50] J. Bechtel, "The Effect of Thermal Creep Flow in a Heat Assisted Magnetic Recording System," Master's thesis, University of California, Berkeley, 2009.
- [51] E. H. Kennard, *Kinetic Theory of Gases With an Introduction to Statistical Mechanics*. McGraw-Hill, 1938.
- [52] F. M. White, *Fluid Mechanics*, 5th ed. New York: McGraw-Hill, 2003.
- [53] S. Zhang and D. B. Bogy, "A heat transfer model for thermal fluctuations in a thin slider/disk air bearing," *International Journal of Heat and Mass Transfer*, vol. 42, pp. 1791–1800, 1999.

- [54] L. Chen, D. B. Bogy, and B. Strom, "Thermal dependence of MR signal on slider flying state," *IEEE Transactions on Magnetics*, vol. 36, no. 5, pp. 2486–2489, 2000.
- [55] D. Chen, N. Liu, and D. Bogy, "A phenomenological heat transfer model for the molecular gas lubrication system in hard disk drives," *Journal of Applied Physics*, vol. 105, p. 084303, 2009.
- [56] J. Zheng and D. B. Bogy, *CML TFC Code User's Manual*, 2009.
- [57] B. Xu, H. Yuan, J. Zhang, J. Yang, R. Ji, and T. Chong, "Thermal effect on slider flight height in heat assisted magnetic recording," *Journal of Applied Physics*, vol. 103, no. 7, 07F525, 2008.
- [58] H. Zheng, H. Li, and F. E. Talke, "Numerical simulation of thermal flying height control sliders in heat-assisted magnetic recording," *Microsystem Technologies*, vol. 18, no. 9-10, pp. 1731–1739, 2012.
- [59] B Xu, Y Toh, C Chia, J Li, J Zhang, K. Ye, and C. An, "Relationship between near field optical transducer laser absorption and its efficiency," *Magnetics, IEEE Transactions on*, vol. 48, no. 5, pp. 1789–1793, 2012.
- [60] B Xu, J Li, Y Toh, K Ye, and J Zhang, "Dynamic Thermal Responses of Heat-Assisted Magnetic Recording Head in Data Writing Process," *Magnetics, IEEE Transactions on*, vol. 48, no. 11, pp. 3280–3283, 2012.
- [61] G. Chen, *Nanoscale Energy Transport and Conversion : A Parallel Treatment of Electrons, Molecules, Phonons, and Photons: A Parallel Treatment of Electrons, Molecules, Phonons, and Photons*. New York: Oxford University Press, 2005.
- [62] E. Cetinorgu, B. Baloulas, O. Zabeida, J. Klemberg-Sapieha, and L. Martinu, "Mechanical and thermoelastic characteristics of optical thin films deposited by dual ion beam sputtering," *Applied Optics*, vol. 48, no. 23, pp. 4536–4544, 2009.
- [63] W. M. Kays and M. E. Crawford, *Convective Heat and Mass Transfer*. New York: McGraw-Hill, 1993.
- [64] L. Wu, "Physical Modeling and Numerical Simulations of the Slider Air Bearing Problem of Hard Disk Drives," PhD thesis, University of California, Berkeley, 2001.
- [65] B. H. Thornton and D. B. Bogy, "Head-disk interface dynamic instability due to intermolecular forces," *IEEE Transactions on Magnetics*, vol. 39, no. 5, pp. 2420–2422, 2003.
- [66] S. Loyalka, "Comments on "poiseuille flow and thermal creep of a rarefied gas between parallel plates"," *Physics of Fluids*, vol. 17, no. 5, pp. 1053–1055, 1974.
- [67] J. E. Bechtel and D. B. Bogy, "Heat-Assisted Magnetic Recording Air Bearing Simulations That Account for Lateral Air Temperature Variation," *IEEE Transactions on Magnetics*, vol. 47, no. 10, pp. 2379–2382, 2011.

- [68] B. V. Budaev and D. B. Bogy, "On the lifetime of plasmonic transducers in heat assisted magnetic recording," *Journal of Applied Physics*, vol. 112, no. 3, p. 034512, 2012.
- [69] A. W. Adamson, *Physical Chemistry of Surfaces*, 5th ed. New York: John Wiley & Sons, Inc., 1990.
- [70] P.-G. de Gennes, F. Brochard-Wyart, and D. Quere, *Capillarity and Wetting Phenomena: Drops, Bubbles, Pearls, Waves*. New York: Springer Science+Business Media, Inc., 2004.
- [71] G. Batchelor, *An Introduction to Fluid Dynamics*. Cambridge, England: Cambridge University Press, 1967.
- [72] H Matsuoka, K Oka, Y Yamashita, F Saeki, and S Fukui, "Deformation characteristics of ultra-thin liquid film considering temperature and film thickness dependence of surface tension," *Microsystem Technologies*, vol. 17, no. 5-7, pp. 983–990, 2011.
- [73] B. V. Derjaguin, N. Churaev, and V. Muller, *Surface Forces*. New York: Consultants Bureau, Plenum Publishing Corporation, 1987.
- [74] C. M. Mate, "Taking a Fresh Look at Disjoining Pressure of Lubricants at Slider-Disk Interfaces," *IEEE Transactions on Magnetics*, vol. 47, no. 1, pp. 124–130, 2011.
- [75] L. Wu, "Modelling and simulation of the lubricant depletion process induced by laser heating in heat-assisted magnetic recording system," *Nanotechnology*, vol. 18, p. 215702, 2007.
- [76] L. Wu and F. E. Talke, "Modeling laser induced lubricant depletion in heat-assisted-magnetic recording systems using a multiple-layered disk structure," *Microsystem Technologies*, vol. 17, no. 5-7, pp. 1109–1114, 2011.
- [77] Y. Zeng, W. Zhou, X. Huang, and S. Yu, "Numerical study on thermal-induced lubricant depletion in laser heat-assisted magnetic recording systems," *International Journal of Heat and Mass Transfer*, vol. 55, no. 4, pp. 886–896, 2012.
- [78] Y.-T. Hsia, P. Jones, and L. R. White, "Can Contact-Angle Measurements Determine the Disjoining Pressure in Liquid Nanofilms on Rigid Substrates?" *Langmuir*, vol. 20, no. 23, pp. 10073–10079, 2004.
- [79] T. Karis and G Tyndall, "Calculation of spreading profiles for molecularly-thin films from surface energy gradients," *Journal of Non-Newtonian Fluid Mechanics*, vol. 82, pp. 287–302, 1999.
- [80] G. W. Tyndall, P. Leezenberg, R. J. Waltman, and J Castenada, "Interfacial interactions of perfluoropolyether lubricants with magnetic recording media," *Tribology Letters*, vol. 4, no. 2, pp. 103–108, 1998.
- [81] G. W. Tyndall, R. J. Waltman, and D. Pocker, "Concerning the interactions between Zdol perfluoropolyether lubricant and an amorphous-nitrogenated carbon surface," *Langmuir*, vol. 14, pp. 7527–7536, 1998.

- [82] R. J. Waltman, D. Pocker, and G. W. Tyndall, "Studies on the interactions between ZDOL perfluoropolyether lubricant and the carbon overcoat of rigid magnetic media," *Tribology Letters*, vol. 4, pp. 267–275, 1998.
- [83] R Powell, W. Roseveare, and H Eyring, "Diffusion, thermal conductivity, and viscous flow of liquids," *Industrial and Engineering Chemistry*, vol. 33, no. 4, pp. 430–435, 1941.
- [84] T Karis, B Marchon, V Flores, and M Scarpulla, "Lubricant spin-off from magnetic recording disks," *Tribology Letters*, vol. 11, no. 3-4, pp. 151–159, 2001.
- [85] J. H. Poynting, "V. Change of state: Solid-liquid," *Philosophical Magazine Series 5*, vol. 12, no. 72, pp. 32–48, 1881.
- [86] V. P. Carey, *Liquid-Vapor Phase-Change Phenomena*, 2nd ed. New York: Taylor & Francis Group, LLC, 2008.
- [87] G. M. Rosenblatt, "Evaporation from Solids," in *Treatise on Solid State Chemistry*, N. Hannay, Ed., vol. 6A, New York: Plenum Press, 1976, ch. 3, pp. 165–240.
- [88] W Zhou, Y Zeng, B Liu, S Yu, and X Huang, "A Model for Laser Induced Lubricant Depletion in Heat-Assisted Magnetic Recording," *Tribology Letters*, vol. 45, pp. 411–416, 2012.
- [89] M. S. Mayeed and T. Kato, "Density Variation in the Ultrathin Liquid Perfluoropolyether Films on Solid Surfaces," *Tribology Transactions*, vol. 44, no. 3, pp. 444–450, 2001.
- [90] E. Ruckenstein and R. K. Jain, "Spontaneous rupture of thin liquid films," *Journal of the Chemical Society, Faraday Transactions 2*, vol. 70, pp. 132–147, 1974.
- [91] H Kubotera and D. Bogy, "Numerical simulation of molecularly thin lubricant film flow due to the air bearing slider in hard disk drives," *Microsystem Technologies*, vol. 13, no. 8-10, pp. 859–865, 2007.
- [92] T Yabe, T Aoki, G Sakaguchi, and P Wang, "The compact CIP (Cubic-Interpolated Pseudo-particle) method as a general hyperbolic solver," *Computers and Fluids*, 1991.
- [93] T Aoki, "Multi-dimensional advection of CIP (Cubic-Interpolated Propagation) scheme," *Computational Fluid Dynamics Journal*, vol. 4, no. 3, pp. 279–291, 1995.
- [94] N. Tagawa, R Kakitani, H Tani, N Iketani, and I Nakano, "Study of Lubricant Depletion Induced by Laser Heating in Thermally Assisted Magnetic Recording System—Effect of Lubricant Film Materials," *IEEE Transactions on Magnetics*, vol. 45, no. 2, pp. 877–882, 2009.
- [95] N. Tagawa, H Andoh, and H Tani, "Study on Lubricant Depletion Induced by Laser Heating in Thermally Assisted Magnetic Recording Systems: Effect of Lubricant Thickness and Bonding Ratio," *Tribology Letters*, vol. 37, pp. 411–418, 2010.

- [96] N. Tagawa and H Tani, “Lubricant Depletion Characteristics Induced by Rapid Laser Heating in Thermally Assisted Magnetic Recording,” *IEEE Transactions on Magnetics*, vol. 47, no. 1, pp. 105–110, 2011.
- [97] N. Tagawa, T. Miki, and H. Tani, “Depletion of monolayer liquid lubricant films induced by high-frequency pulsed-laser heating in thermally assisted magnetic recording,” *Microsystem Technologies*, vol. 18, no. 9-10, pp. 1353–1357, 2012.
- [98] Y. Ma, L. Gonzaga, C. An, and B. Liu, “Effect of Laser Heating Duration on Lubricant Depletion in Heat Assisted Magnetic Recording,” *IEEE Transactions on Magnetics*, vol. 47, no. 10, pp. 3445–3448, 2011.
- [99] Y. Ma, X. Y. Chen, J. M. Zhao, S. K. Yu, B Liu, H. L. Seet, K. K. Ng, J. F. Hu, and J. Z. Shi, “Experimental Study of Lubricant Depletion in Heat Assisted Magnetic Recording,” *IEEE Transactions on Magnetics*, vol. 48, no. 5, pp. 1813–1818, 2012.
- [100] Y. Ma, X. Chen, and B. Liu, “Experimental Study of Lubricant Depletion in Heat Assisted Magnetic Recording over the Lifetime of the Drive,” *Tribology Letters*, vol. 47, no. 2, pp. 175–182, 2012.
- [101] —, “Experimental study of lubricant depletion in heat assisted magnetic recording: effects of laser heating duration and temperature,” *Microsystem Technologies*, vol. 19, no. 2, pp. 291–297, 2013.
- [102] W Zhou, Y Zeng, B. Liu, S Yu, W Hua, and X. Huang, “Evaporation of Polydisperse Perfluoropolyether Lubricants in Heat-Assisted Magnetic Recording,” *Applied Physics Express*, vol. 4, p. 095201, 2011.
- [103] Q. Dai, C Saint-Olive, R Pit, and B. Marchon, “Genesis and evolution of lubricant moguls,” *IEEE Transactions on Magnetics*, vol. 38, no. 5, pp. 2111–2113, 2002.
- [104] Q. Dai, B. E. Knigge, R. J. Waltman, and B. Marchon, “Time evolution of lubricant-slider dynamic interactions,” *IEEE Transactions on Magnetics*, vol. 39, no. 5, pp. 2459–2461, 2003.
- [105] R Pit, Q.-H. Zeng, Q. Dai, and B. Marchon, “Experimental study of lubricant-slider interactions,” *IEEE Transactions on Magnetics*, vol. 39, no. 2, pp. 740–742, 2003.
- [106] Q. Dai, F Hendriks, and B. Marchon, “Washboard effect at head-disk interface,” *IEEE Transactions on Magnetics*, vol. 40, no. 4, pp. 3159–3161, 2004.
- [107] R. Ji, T. K. L. Dao, B. X. Xu, J. W. Xu, B. L. Goh, E. Tan, H. Q. Xie, and T Liew, “Lubricant Pickup Under Laser Irradiation,” *IEEE Transactions on Magnetics*, vol. 47, no. 7, pp. 1988–1991, 2011.
- [108] N. Tagawa, H Tani, and K. Ueda, “Experimental Investigation of Local Temperature Increase in Disk Surfaces of Hard Disk Drives Due to Laser Heating During Thermally Assisted Magnetic Recording,” *Tribology Letters*, vol. 44, no. 1, pp. 81–87, 2011.

- [109] R. J. Waltman, "The interactions between Z-Tetraol perfluoropolyether lubricant and amorphous nitrogenated-and hydrogenated-carbon surfaces and silicon nitride," *Journal of Fluorine Chemistry*, vol. 125, pp. 391–400, 2004.
- [110] M Stirniman and J. Gui, "Polydispersity Effects in the Evaporation of Perfluoropolyether Thin Films," *Journal of Physical Chemistry B*, vol. 106, no. 23, pp. 5967–5971, 2002.
- [111] J. B. Dahl and D. B. Bogy, "Lubricant Flow and Evaporation Model for Heat Assisted Magnetic Recording Including Functional End-Group Effects and Thin Film Viscosity," *Tribology Letters*, vol. 52, no. 1, pp. 27–45, 2013.
- [112] T. E. Karis, W. Kim, and M. Jhon, "Spreading and dewetting in nanoscale lubrication," *Tribology Letters*, vol. 18, no. 1, pp. 27–41, 2005.
- [113] X. Ma, J. Gui, L Smoliar, K Grannen, B. Marchon, C Bauer, and M Jhon, "Complex terraced spreading of perfluoropolyalkylether films on carbon surfaces," *Physical Review E*, vol. 59, no. 1, pp. 722–727, 1999.
- [114] C. M. Mate, "Application of disjoining and capillary pressure to liquid lubricant films in magnetic recording," *Journal of Applied Physics*, vol. 72, no. 7, pp. 3084–3090, 1992.
- [115] X. Ma, J. Gui, B. Marchon, M. Jhon, C. L. Bauer, and G. C. Rauch, "Lubricant replenishment on carbon coated discs," *IEEE Transactions on Magnetics*, vol. 35, no. 5, pp. 2454–2456, 1999.
- [116] B. Marchon, "Lubricant Design Attributes for Subnanometer Head-Disk Clearance," *IEEE Transactions on Magnetics*, vol. 45, no. 2, pp. 872–876, 2009.
- [117] R. M. Christensen, *Theory of Viscoelasticity*, 2nd. New York: Academic Press, Inc., 1982.
- [118] B. Marchon and T. E. Karis, "Poiseuille flow at a nanometer scale," *Europhysics Letters*, vol. 74, no. 2, pp. 294–298, 2006.
- [119] R. L. Smith, Y. I. Jhon, L. T. Biegler, and M. S. Jhon, "An Atomistic Study of Perfluoropolyether Lubricant Thermal Stability in Heat Assisted Magnetic Recording," *IEEE Transactions on Magnetics*, vol. 49, no. 7, pp. 3748–3751, 2013.
- [120] J. B. Dahl and D. B. Bogy, "Simulation of Lubricant Recovery After Heat Assisted Magnetic Recording Writing," *Tribology Letters*, vol. 52, no. 1, pp. 163–174, 2013.